Diplomarbeit

Additive Manufacturing of Ni-modified polymer-derived ceramics for CO_2 methanation

ausgeführt am Institut für
Chemische Technologien und Analytik
der Technischen Universität Wien

unter der Anleitung von
Associate Prof. Dipl.-Ing. Dr.techn. Thomas Konegger
Dipl.-Ing. Johannes Eßmeister

durch

Lisa SCHACHTNER

Matr.-Nr.: 01525257

Ort und Datum

Unterschrift (Studentin)

Eidesstattliche Erklärung

Ich erkläre an Eides statt, dass die vorliegende Arbeit nach den anerkannten Grundsätzen für wissenschaftliche Abhandlungen von mir selbstständig erstellt wurde. Alle verwendeten Hilfsmittel, insbesondere die zugrunde gelegte Literatur, sind in dieser Arbeit genannt und aufgelistet. Die aus den Quellen wörtlich entnommenen Stellen sind als solche kenntlich gemacht.

Das Thema dieser Arbeit wurde von mir bisher weder im In- noch Ausland einer Beurteiler*in zur Begutachtung in irgendeiner Form als Prüfungsarbeit vorgelegt. Diese Arbeit stimmt mit der von den Begutachter*innen beurteilten Arbeit überein.

Ort und Datum

Unterschrift (Studentin)

Abstract

The conversion of CO_2 into valuable raw materials and the associated reduction of CO_2 in the atmosphere is a fundamental goal of our time. Thus, catalytically active metals required for gas conversion, such as nickel (Ni), as well as stable ceramic carrier structures both represent a broad field of research. To find alternatives to the conventional manufacturing route, where the carrier material is impregnated, the focus of this work is the direct incorporation of Ni into a polymer-derived ceramic matrix. In contrast to conventional methods, this allows the presence of metal particles even in the smallest pores.

Components of varying complexity could be produced by modifying preceramic polysilsesquioxane with $Ni(NO_3)_2$ using methacrylic acid and shaping via vat-based photopolymerization, an advanced additive manufacturing technique.

Through pyrolysis of the Ni-modified preceramic polymer at moderate temperatures (600-800 °C), amorphous SiOC components with well dispersed nanocrystalline Ni particles were obtained. Modifying the polymer and subsequent conversion prevents the Ni particles from sintering together.

The modified polymer and the fabricated structures were characterised by photorheology, simultaneous thermal analysis, scanning electron microscopy, transmission electron microscopy, and powder x-ray diffraction. In addition, a change in specific surface area, crystallinity, and shrinkage as a function of the pyrolysis temperature was observed. The influences of trimethylolpropane trimethacrylate as a reactive diluent and urethane dimethacrylate as a porogen to increase the specific surface area were also investigated.

The developed material enables additive manufacturing of porous SiOC structures with crystalline, uniformly distributed, and bimodal Ni nanoparticles embedded within. The SiOC/Ni components showed an existing catalytic activity, especially regarding CO_2 methanation. The developed printable SiOC/Ni material represents a promising starting-point for combining complex metal-modified polymer-derived ceramic systems with shaping by additive manufacturing for prospective catalysis applications.

Kurzfassung

Die Umwandlung von CO_2 in wertvolle Rohstoffe und die damit einhergehende CO_2-Reduktion in der Atmosphäre ist ein elementares Ziel unserer Zeit. Sowohl die Entwicklung der für die Gasumwandlung benötigten katalytisch aktiven Metalle wie Nickel, als auch stabile keramischen Trägerstrukturen stellen somit ein breites Forschungsfeld dar. Um eine Alternative zum klassischen Verfahren zu finden, bei der das Trägermaterial nachträglich imprägniert wird, wurde im Zuge dieser Arbeit der Fokus auf die Einbringung von Nickel in eine präkeramische keramische Matrix gelegt. Dies ermöglicht im Gegensatz zu konventionellen Methoden die Anwesenheit von Metallpartikeln selbst in den kleinsten Poren.

Durch Modifizierung von präkeramischen Polysilsesquioxan mit $Ni(NO_3)_2$ unter Verwendung von Methacrylsäure und anschließender Formgebung über photopolymerisationsbasierte additive Fertigung konnten Bauteile mit unterschiedlicher Komplexität erzeugt werden. Durch Pyrolyse des Ni-modifizierten Polymers bei moderaten Temperaturen (600-800 °C), konnten amorphe SiOC-Bauteile mit fein verteilten, nanokristallinen Nickelpartikeln hergestellt werden. Zudem verhindert das Modifizieren des Polymers und die anschließende Umwandlung ein Zusammensintern der Ni-Partikel

Das modifizierte Polymer sowie die hergestellten Strukturen wurden unter anderem mittels Photorheologie, Simultane thermische Analyse, Elektronenstrahlmikroskopie und Röntgenbeugung charakterisiert. Zudem konnte eine Veränderung der spezifischen Oberfläche, Kristallinität und Schwindung in Abhängigkeit der Pyrolysetemperatur beobachtet werden. Auch die Einflüsse von Trimethylolpropantrimethacrylat als Reaktivverdünner und Urethandimethacrylat zur Erhöhung der spezifischen Oberfläche wurden untersucht.

Das entwickelte Material ermöglicht die Herstellung von porösen additiv gefertigten SiOC-Strukturen mit darin eingebetteten kristallinen, gleichmäßig verteilten, und bimodalen Ni-Nanopartikeln. Die SiOC-Ni-Komponenten zeigten eine vorhandene katalytische Aktivität, besonders in Bezug auf die CO_2 Methanisierung. Das entwickelte druckbare SiOC/Ni-Material stellt einen vielversprechenden Ausgangspunkt für die Kombination komplexer metallmodifizierter polymerer Keramiksysteme mit additiver Formgebung für zukünftige Katalyseanwendungen dar.

Danksagung

Mein besonders herzlicher Dank gilt Thomas Konegger für die zahlreichen Anregungen, Diskussionen und die Betreuung dieser Arbeit. Danke, Thomas, für die Möglichkeit in einer tollen Arbeitsumgebung an einem spannenden und aktuellen Thema zu arbeiten. Ich konnte sehr viel von dir lernen. Besonders bedanken möchte ich mich auch bei Johannes Eßmeister für die umfangreiche Unterstützung, Hilfestellung bei verschiedensten Geräten und Analysemethoden und die verlässliche Bereitschaft zur Problemlösung. Du warst stets bereit mich zu unterstützen und mit mir gemeinsam an diversen Problemstellungen zu arbeiten. Auch bei Eva Szoldatits möchte ich mich für die tolle Teamarbeit und Durchführung zahlreicher Messungen herzlich bedanken. Danke für die BET und Katalyse Messungen an deinem wirklich gelungenen Teststand. Vielen Dank auch an Karin Föttinger für die interessanten Diskussionen.

Ich möchte mich herzlich bei der gesamten Keramik-Gruppe bedanken. Danke für die großartige Arbeitsatmosphäre und die Möglichkeiten mich mit euch auszutauschen. Vielen Dank auch an Max Podsednik und Professor Andreas Limbeck, welche mir die ICP-MS Messungen ermöglich haben.

Bedanken möchte ich mich auch bei jenen Kolleg*innen, die mich mit Messgeräten, ihrem Fachwissen und Python unterstützt haben. Danke an den gesamten und erweiterten 2. Stock und die Lehar 04 Gruppe für die schöne Zeit und dafür, dass ihr immer ein offenes Ohr für mich hattet.

Zu guter Letzt möchte ich mich noch bei meiner Familie für die Unterstützung während des gesamten Studiums bedanken. Vielen Dank, dass ihr mir ermöglicht habt, mich in einem so interessanten Gebiet weiterzubilden. Danke auch an Stephan für das große Verständnis und die Bereitschaft, dir meine Erzählungen anzuhören. Du warst mir in dieser Zeit die größtmögliche Unterstützung!

Symbols

Abbreviation	Denotation	unit of measurement
$[CH_4]_{out}$	molar fractions of CH_4 in the gas coming out	(vol%)
$[CO_2]_{in/out}$	molar fractions of CO_2 in the gas going in/out	(vol%)
2Θ	diffraction angle	(°)
A	absorption	(A.U.)
Cd	curing depth	(mm)
DBC	double bond conversion	(%)
DBC_{final}	final conversion	(%)
DBC_g	conversion at the gel point	(%)
f	frequency	(Hz)
F_N	normal force/shrinkage force	(N)
G’	storage modulus	(kPa)
G’’	loss modulus	(kPa)
G’max	maximum storage modulus	(kPa)
I	intensity	(mW/cm^2)
Lt	layer thickness	(mm)
m	mass	(g)
n	wavenumber	(cm^{-1})
O	mechanical displacement	(%)
p	pressure	(mbar)
P	count of measurement points	()
S_{CH4}	selectivity towards CH_4	(%)
t	time	(min)
T	temperature	(°C)
t_g	time to gel point	(s)
t_i	time interval between measurement points	(s)

t_m	measuring time	(s)
v	velocity	(mm/min)
v_g	gas flow velocity	(l/min)
v_h	heating rate	(K/min)
v_r	rotational speed	(rpm)
X_{CO2}	CO_2 conversion	(%)
λ	wavelength	(nm)

List of Abbreviations

Abbreviation	Denotation
Ar	argon
ART-FTIR	attenuated total reflectance Fourier-transform infrared spectroscopy
BAPO	phenylbis (2,4,6-Trimethylbenzoyl) phosphine oxide
CAD	computer-aided design
CH_3OH	methanol
CH_4	methane
CO	carbon monoxide
CO_2	carbon dioxide
DLP	digital light processing
DTA	differential thermal analysis
EDX	energy-dispersive X-ray spectroscopy
FEG	field emission gun
FS-air	fracture surface – fractured on air
FS-gb	fracture surface – fractured under Ar in a glovebox
G*16	Genorad*16
GC	gas chromatography
H_2	hydrogen
HCl	aqueous hydrochloric acid
HDDA	hexanediol diacrylate
HQ	hydroquinone
ICP-MS	inductively coupled plasma mass spectrometry
IR	infrared
LCM	lithography-based ceramic manufacturing
MAA	methacrylic acid
MK	methyl-silsesquioxane (Silres MK, Wacker)

Ni	nickel
NiN	nickel(II)nitratehexahydrate
PCP	preceramic polymer
PDC	polymer-derived ceramic
PSO	polysilsesquioxanes basic system
SA	surface area
SEM	scanning electron microscopy
SiC	silicon carbide
SiOC	silicon oxycarbide
SLA	stereolithography
SSA	specific surface area
STEM	scanning transmission electron microscopy
TEM	transmission electron microscopy
TGA	thermogravimetric analysis
THF	tetrahydrofuran
TMPTA	trimethylolpropane triacrylate
TMPTMA	trimethylolpropane trimethacrylate
TMSPM	3-(trimethoxysilyl)-propyl methacrylate
TPM	tri(propyleneglycol)-methyl ether
Tween 20	polyoxyethylene (20) sorbitan monolaurate
UdMA	aliphatic urethane dimethacrylate
UV	ultraviolet
XPS	x-ray photoelectron spectroscopy
XRD	powder x-ray diffraction
XRF	x-ray fluorescence spectroscopy

Table of Contents

1 Introduction

Since carbon dioxide (CO_2) is a very stable molecule, a catalyst is required for its conversion into valuable raw materials. [1] Porous ceramics are typically chosen as carrier structures for catalytically active metals, for example platinum (Pt), palladium (Pd), or nickel (Ni). Ceramics are used due to their unique properties, such as high melting point, high strength, and environmental resistance. [2] Conventional catalysts are produced by impregnating a ceramic support structure with the desired metal after sintering. [3]

Alternatively, polymer-derived ceramics (PDC) can be used to directly modify the polymer, for example by derivatising, rather than using impregnation processes for subsequent modifications. Another benefit of PDCs is their wide range of possible shaping techniques. Especially additive manufacturing is an important method, as it is suitable for complex-shaped parts. Stereolithography for ceramics typically involves using UV light to cure slurries of photopolymers and ceramic particles into the desired pattern. The cured polymer is then removed during sintering. This technique is also suitable for additive manufacturing of preceramic polymers, where the organic material is thermally converted into a ceramic material instead of combusting during sintering. [4] Different materials can be produced, depending on the polymer used. When aiming for SiOC, polysiloxanes with the addition of photoactive groups can be used. [5]

The modification of the preceramic polymer with Ni prior to the pyrolytic conversion opens up new advantages. Producing catalysts using metal-modified polymer-derived ceramics makes it possible to distribute the catalytically active Ni-particles homogeneously throughout the component. High porosity enables the presence of Ni even in the smallest pores, which would not be achieved by impregnation. With the Ni being well incorporated within the matrix, this approach prevents the Ni particles from sintering together and reduces the gas phase loss of nickel during catalysis.

The objective of this work was to establish a Ni-modified preceramic polymer system suitable for additive manufacturing. To be applicable for additive manufacturing via bottom-up stereolithography, the polymer resin had to be photosensitive with a fast gel point. It had to be homogenous and have adequate viscosity to allow the resin to flow during the printing process. Additionally, a gentle detachment from the bottom of the vat for the individual printing layers had to be guaranteed. The stability of the components during printing, postprocessing, and pyrolysis had to be ensured likewise.

The aim was to use the material for catalytic CO_2 methanation in thermal catalysis. For this purpose, Ni centres have to be well dispersed within the ceramic matrix to increase the number of accessible Ni-sites for catalysis.

The focus was put on the production of the material and its in-depth characterisation. Besides the characterisation of the preceramic polymer, the resulting polymer-derived ceramic was characterised with respect to morphology and the distribution of Ni within the ceramic matrix. In addition, the influence of different temperatures on the pyrolytic polymer-to-ceramic conversion was to be investigated. The catalytic activity was determined to draw conclusions about the applicability of the material in CO_2 utilisation processes.

2 Theoretical Background

The following sections give an overview of the catalysis of CO_2, more specifically CO_2 methanation. Furthermore, polymer-derived ceramics as support material for catalytically active metals are discussed. An overview of the methods for metal modification of preceramic polymers is given with a focus on derivatisation. Finally, an introduction on additive manufacturing is given with a special focus on vat-based photopolymerisation of metal-modified preceramic polymers.

2.1 Metal-based heterogeneous catalysis

Converting carbon dioxide (CO_2) into valuable chemicals and therefore reducing the concentration of CO_2 in the atmosphere is one of the most urgent scientific challenges ahead. [6] The conversion of CO_2 into valuable chemicals, such as methane (CH_4) and methanol (CH_3OH), are exothermic reactions which are thermodynamically favoured at lower reaction temperatures. [3] To promote the reaction, a substance exhibiting higher Gibbs free energy within the system, such as hydrogen (H_2), can be added to thermodynamically favour the CO_2 conversion and hence reduce the carbon involved. [1] Still, the high kinetic energy barrier associated with the CO_2 conversion is problematic for industrial applications. [7] An essential part of the reduction of CO_2 by H_2 through heterogeneous catalysis is the metallic catalyst, which needs to be active, selective and stable under the required reaction conditions. [6] By lowering the energy barrier the catalyst is essential for achieving appropriate conversion rates. [1]

Noble metals such as platinum, palladium, ruthenium and rhodium or transition metals like nickel, cobalt and iron have been investigated as promising candidates for the use as a catalyst in the hydrogenation of CO_2 towards CH_4. Noble metals are known for their relatively high activity and selectivity compared to other metals. Nonetheless, their high costs and low abundance restrict their commercial use. Besides noble metal-based catalysts, especially Ni was found to be selective towards CH_4 production through H_2 and CO_2. [8] Ni-based catalysts are thus commonly used for the hydrogenation of CO_2 to CH_4, the so-called CO_2 methanation (1), and are promising for industrial applications due to their abundance, low costs, and high activity. [8, 9] But challenges such as low-temperature activity, low dispersion and reducibility, and nanoparticle sintering have to be faced when using Ni-based catalysts. [9] The CO_2

methanation is thermodynamically favourable and faster than the reaction to alcohols or hydrocarbons. [8] Side-reactions, such as reverse water gas shift reaction (2), still occur during methanation, negatively affecting the purity and making further purification steps necessary. [7, 8] Compared to the desired products, CO_2 is a stable molecule, which means as a result a suitable catalyst and elevated reaction temperatures (200-400 °C) are necessary for the success of the catalytic conversion. [3] Possible reaction occurring during catalysis can be seen below (Eq. 1-3).

$$4\ H_2 + CO_2 \rightarrow CH_4 + 2\ H_2O \qquad (1)$$

$$H_2 + CO_2 \rightarrow CO + H_2O \qquad (2)$$

$$CO + 3\ H_2 \rightarrow CH_4 + H_2O \qquad (3)$$

The CO_2 methanation is a structure-sensitive reaction, meaning the particle size strongly influences the kinetics, as the coordination of surface atoms changes as a function of the particle size. Considering the exothermic nature of the reaction, at elevated reaction temperatures, the Ni-particles are prone to agglomeration. Therefore, sintering of the particles at high temperatures poses a serious problem as activity and long-term stability of the catalyst are thereby decreased. To obtain a highly active catalyst with well-dispersed metal particles, only minimal particle growth can be tolerated. [3, 8] At low metal concentrations, Ni is generally found to be highly dispersed on the support, while the particles tend to agglomerate at higher concentrations.[10] According to *Wu et al.* [7], the most efficient catalysts have small and well-dispersed particles. To optimize activity and selectivity toward the desired product, the ideal particle size distribution is individual for every specific catalytic system.

Another problem caused by the sintering of Ni particles is the deactivation of the catalyst due to the limited steric accessibility of Ni. The deactivation of the catalyst may also occur in the presence of carbon monoxide (CO), which may result from CO disproportionation or incomplete CO hydrogenation reactions (3). [3] It is known that significant amounts of CO can inhibit the CO_2 methanation reaction and lead to substantial deactivation of the catalyst through carbon deposition or $Ni(CO)_4$ formation. [11]

The robust nature of ceramics makes them ideal candidates for catalytic support materials. [12] Silicon carbide (SiC) has proven to be a suitable support material for catalysts due to its thermal stability, high heat conductivity, and chemical inertness. [2] The disadvantage, however, is that commercial SiC powders have a very low specific surface area. To achieve a high catalytic conversion of the gas into the desired product, a high specific surface area is required to improve the metal dispersion, to keep the gas-catalyst interaction as high as possible, and to facilitate the internal exchange of substances. [2, 8] *Le et al*. [13] investigated Ni-based catalysts supported on SiO_2 and SiC for the CO and CO_2 methanation reaction. In their paper, it was shown that high Ni dispersion and strong CO_2 adsorption can improve the catalytic activity for CO_2 methanation. The high thermal conductivity provided by SiC also appears to be beneficial for CO and CO_2 methanation. Regarding the improvement of the dispersion of catalytically active components, polymer-derived ceramics via a sol-gel method are becoming increasingly important compared to the traditional wet impregnation of SiC powders. [12]

2.2 Polymer-derived ceramics

Preceramic Polymers are classified as organosilico polymers which are based on a Si-based backbone with variable substituents such as carbon, oxygen, hydrogen, nitrogen and boron. When pyrolyzed under controlled and inert conditions, the preceramic polymer can be directly converted into a ceramic material – a so-called polymer-derived ceramic (PDC). [1] Based on their property profile, PDCs have been investigated for their use as structural ceramics in high-temperature applications. PDCs in general exhibit enhanced properties concerning creep and oxidation resistance. Relatively low synthesis temperatures, low costs, necessity of high-purity products and the option for geometric design variability are all desirable economic qualities. [1, 5]

2.2.1 Polymer-derived SiOC

Due to its molecular structure, the properties of Si-based PDCs can be varied by adapting the polymer via derivatisation to suit the intended application. The chosen polymer also has a major influence on the final phases and microstructure of the ceramic product. [1, 5]

A wide range of polymer precursors can be used to modify silicon-based polymer systems to obtain suitable preceramic polymers (PCPs). In addition to the elemental composition and the versatile end groups, the degree of cross-linking can be modified. By choosing suitable end groups, which provide for 3-dimensional cross-linking, an infusible polymer (green body) can be obtained as a predecessor for ceramisation. An important sub-group of polysiloxanes are non-linear polysilsesquioxanes, characterised by their general formula $–[RSi–O_{1.5}]_n–$ (with R being hydrogen or an organic aryl or alkyl group) and their highly branched molecular structure. [1, 5, 12]

Polysilsesquioxane PCPs are usually prepared using sol-gel methods including a hydrolysis step, followed by the condensation of the alkoxide end groups.

$$R'SiOR_3 + 3\ H_2O \rightarrow RSi(OH)_3 + HOR \quad (4)$$

$$3\ R'Si(OH)_3 \rightarrow 3\ R'SiO_{1.5} + ½\ H_2O \quad (5)$$

$$R'Si(OH)_3 + R'SiOR_3 \rightarrow RSiO_{1.5} + 3\ HOR \quad (6)$$

The hydrolysis (4), to obtain hydroxyl groups, can be initiated by the addition of controlled amounts of water, acid or base. The hydrolysis is followed by the condensation (5) and (6), leading to the formation of a three-dimensional network, known as the polymeric gel. [1, 14, 15]

If the catalyst used for hydrolysis is acidic, the electrophilic hydrolysis reaction proceeds faster than the condensation, resulting in a less branched network with longer chains, often referred to as silicone resin. [1]

PCP is cured by exposure to heat or, in the presence of a suitable photoinitiator and reactive groups, by radiation such as UV light. After shaping and curing are completed, the polymer-to-ceramic transformation proceeds at high reaction temperatures. [5]

The conversion is a complex process in which a series of simultaneous chemical and physical transformations take place until ceramic material is obtained. [1] Regarding polysilsesquioxane, which exhibits a Si-O-Si backbone, pyrolysis leads to the formation of silicon oxycarbides (SiO_xC_y), a ternary PDC, with high hardness and high service temperatures. [1, 12, 16] It is also known for its strong oxidation and corrosion resistance, chemical stability and thermal durability. [15]

The conversion into ceramic components takes place at moderate to high temperatures to consolidate the elements contained in the polymer into the final ceramic. When lower pyrolysis temperatures are applied (400-700 °C), ceramic-polymer hybrid materials (ceramers) with high specific surface areas are obtained. At higher temperatures the ceramers are converted into amorphous or even crystalline structures. [5, 17] Variation of the process parameters, such as atmosphere composition and pyrolysis temperature, allows for the adjustment of properties such as porosity and metal dispersion. [18]

The pyrolysis is usually carried out in an inert environment to control the composition of the desired product. [5] A common method is controlled pyrolysis in a tube furnace, where an inert gas flow ensures the removal of decomposition gases. [5, 12, 17]

A major drawback of PDCs is their strongly pronounced shrinkage that is difficult to control, affecting the structural integrity of the final product. The loss of volatile additives needs to be taken into account when adjusting the heating and cooling rates at temperatures up to 1500 °C. [1] The conversion leads to the decomposition of organic moieties (such as methyl groups) and Si-OH groups into volatile species that leave the material. [5, 12, 17] After the initial rearrangements between and within the chains of the polymer, mineralisation of the residual material occurs. Above 800 °C redistribution reactions of silicone sites occurs, leading to SiOC. [19] The voids resulting from the removal of organic components can lead to structural weaknesses. [15]

During thermal conversion, not only a structural rearrangement and thus a cleavage of chemical bonds takes place, but also a decomposition of organic compounds, resulting in an inorganic ceramic. At temperatures up to 400 °C, the elimination of solvent and other organic compounds with a lower molecular weight takes place. If present, any residual double bonds not cured during preceding polymerisation can then be thermally cross-linked. At higher temperatures (up to 800 °C) the cleavage of stronger bonds present in the polysilsesquioxane takes place. Between 800 °C and 1000 °C hardly any mass loss can be observed, suggesting that the conversion into an inorganic material is complete. At these temperatures, chemical bonds in the amorphous ceramic rearrange and compositional changes take place. The crystallisation process is initiated at even higher temperatures. [1] Figure 1 shows a simplified representation of the pyrolytic conversion of a preceramic polymer into a polymer derived ceramic.

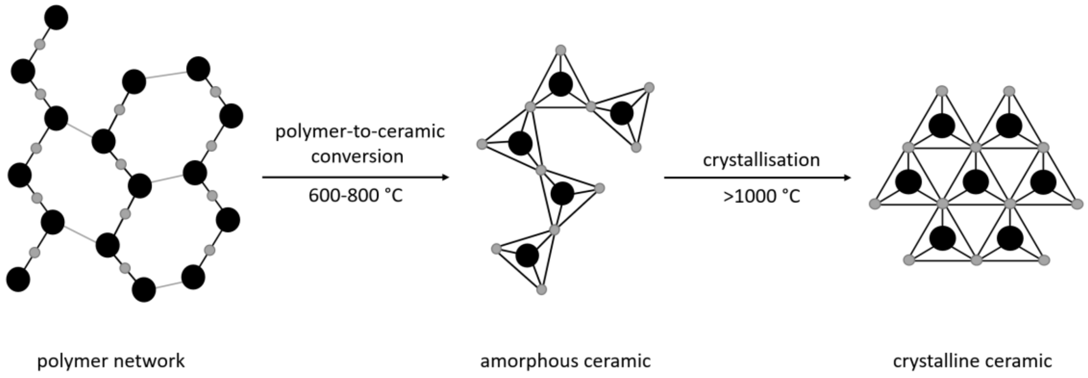

Figure 1: Simplified representation of the pyrolytic conversion of a polymer into ceramer and further into a crystalline ceramic.

Upon heat treatment under an inert atmosphere, the cured preceramic polymer pyrolyzes to an inorganic ceramic. The composition of the final ceramic depends on the polymer used. [12] Besides its composition, the properties of the desired product can be tailored through variation of the pyrolysis conditions. Pyrolysis at temperatures up to 800 °C result in materials with a high specific surface area due to the formation of micro- and mesopores during decomposition reactions. At these temperatures, the transformation to ceramic is interrupted. The hybrid material ceramer, in which the polymer is only partially converted into ceramic, presents properties related to both ceramic and polymeric characteristics. [1]

2.2.2 Metal-modified preceramic polymers

To obtain metal-modified PDCs, three approaches can be distinguished. The first option consists of the physical blending of inorganic metal-containing powders into the preceramic material, followed by curing and pyrolysis. This method is limited in terms of the particle size of the metal (oxide) powders. Due to that, sedimentation and dispersion problems often arise. The second option is synthesis from metallopolymers, in which the metal precursor is integrated into the polymer main chain, often leading to an elaborate preparation route. With these single-source precursors, the distribution of the metal is improved and the desired nanoparticles are built-up, starting from the atomic scale via the formation of clusters. The modified PCP is then again cured and pyrolyzed. As a third option, the derivatisation of the PCP with the introduction of complexing agents is considered a promising preparation method. Well dispersed metal particles within the ceramic matrix are achieved and problems revolving around sedimentation and sintering are eliminated while remaining implementable in industrial environments. The fabricated metal complexes subsequently react with the polymeric preceramic precursor. After a transfer of the metal species from the complex to the polymer chain, a metal-modified precursor is obtained which is ready for curing and pyrolysis. After curing, the added metal becomes part of the precursor and remains well distributed in the PDC matrix during pyrolysis. [1, 12] Figure 2 shows the schematic possibilities for modifying PDCs.

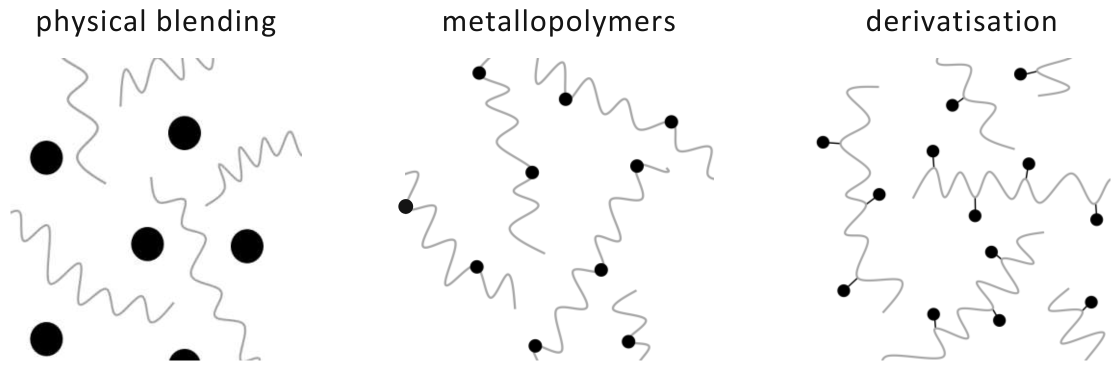

Figure 2: Three methods for incorporating metal into a preceramic polymer to obtain metal modified PCDs: physical blending of PCP and powder, the use of metallopolymers and derivatisation of preceramic polymers.

As stated in chapter 2.1 (Metal-based heterogeneous catalysis), in this work, Ni was chosen as the catalytically active component. At this point it should be addressed that other metals such as copper (Cu), iron (Fe), cobalt (Co) or titanium (Ti), can also be introduced into the matrix. [1] Inorganic salts, such as metal nitrates or metal chlorides, are cheap metal carriers with high metal content. Nevertheless, most inorganic salts are water-soluble and therefore difficult to incorporate into or mix with a preceramic polymer. [20] As for Ni, Ni-particles obtained through the use of Ni(II)nitrate ($Ni(NO_3)_2$) are reported to suffer from sintering and redistribution, while such conduct is not known in case of Ni(II)acetylacetonate ($Ni(acac)_2$). As $Ni(acac)_2$ displays a higher solubility in organic solvents, it is compatible with the polymeric solution to larger extents. [18]

The integration of the metal into the preceramic silicon matrix by the use of complexing precursors with organic components results in a homogeneous distribution. [1] The use of complexing agents that include amino groups, which can also act as cross-linkers, improve the stability and curability of the preceramic polymer. [18] To ensure complexation of the Ni ions and to provide additional cross-linking agents for the polymeric network, an amino-containing siloxane is usually the complexing agent of choice. Examples are 3-amino-propyldiethoxymethylsilane, 3-aminopropyl-triethoxysilane, 2-amino-ethyl-3-aminopropyl-trimethoxysilane and bis-[3-(trimethoxysilyl)propyl]amin. [1, 18] Complexing siloxanes have been reported to be very efficient in creating small and well-distributed Ni nanoparticles. [18] As an alternative, *Fu et al.*[21] proposed methacrylic acid as a complexing agent to prepare a 3D printable metal-modified preceramic polymer.

According to *Adam et al.* [22], the final particle size of the added metal modification can be reduced while improving the homogeneity by increasing the molar ratio of complexing agent and metal ion. However, it has not been confirmed yet which starting materials have a decisive influence on the final metal particle size. *Schumacher et al.* [18] stated that the complexing agent influences the final metal particle size in the ceramics, opposed to *Macedo et al.* [1] who found that the metal particle size was nearly independent of the complexing agent used. Yet, a stronger dependence on the Ni salt used as a metal precursor was observed. $Ni(NO_3)_2$ and Ni acetate ($Ni(AcO)_2$) were found to form smaller particles, compared to $NiCl_2$ and $Ni(acac)_2$. Another selection criterion of the metal precursor is the required solubility to achieve a high dispersion of the metal.

The generation of uniformly dispersed metal nanocrystals with a diameter of 2-5 nm within an amorphous SiOC ceramic was obtained after pyrolysis at 1000 °C by *Fu et al.* [21]. Upon pyrolysis at 1200 °C a larger amount of well-distributed nanoparticles with a diameter of 4-8 nm was obtained.

The introduction of metal elements at the atomic level prevents sedimentation and improves the mechanical properties of the structures obtained. This also simplifies the shaping process through stereolithography-based additive manufacturing. [21]

2.2.3 Additive manufacturing by stereolithography

Ceramic materials are important for a variety of applications due to their unique properties such as their high melting point, excellent high-temperature performance, hardness and chemical stability in harsh conditions. Due to their brittleness and hardness, it has always been a challenge to machine complex ceramic parts. [21, 23] Conventional shaping technologies such as slip casting and extrusion casting are cumbersome when fabricating intricately shaped structures that often require post-processing operations. [20, 23-25] Additive manufacturing (AM) is an alternative production process for 3D microstructures. Structures that are not feasible using conventional ceramic methods can indeed be realized through this approach. [25] AM offers advantages such as mould-free fabrication, near-net-shapes, versatile customizability and rapid prototyping. [21] Moreover, the design of complex structures with a high degree of flexibility and the reduction of waste material enables short product lead time. [15]

Additive manufacturing techniques in general can be categorized into extrusion and jetting-based, photopolymerisation-based and powder sintering/melting-based techniques. [15] The method chosen in this work belongs to photopolymerisation-based additive manufacturing.

Photopolymerisation-based additive manufacturing

A rising segment in AM for ceramics are photopolymerisation-based systems, where it can be distinguished between slurry-based methods and the use of preceramic polymers, where the focus of this work is set on.

AM processes based on photopolymerisation are versatile in terms of material and equipment requirements and can produce parts with high resolution. [15]

Furthermore, a wide range of structures is achievable through the implementation of a light-curable polymer that allows for the application of plastic forming techniques. PDCs thus combine the moldability of polymers and the thermomechanical properties of ceramics, which opens up further application possibilities. [1, 21] The conversion of PCPs and ceramic-polymer blends into solid ceramic structures based on photopolymerisation is often accompanied with challenges. These range from shrinkage and mass loss to cracking and undesirable surface properties. [15]

Photopolymerisation, the formation of long-chain macromolecules by continuous reaction of monomers in the presence of light, is a chain reaction usually initiated by a photoinitiator. The photoinitiator can absorb photons from the exposed light to form reactive species that are essential for polymerisation. The reactive species react with the functional groups of the monomers in the liquid resin and further reactive species are generated. The increase of the reaction chain results in the formation of solid polymer structures. The chemical and structural properties of the printed (green) body differ from those of the resin used. The polymerisation rate and depth depend on the intensity and wavelength of the light. [15, 23]

Stereolithography

One example of photopolymerisation-based additive manufacturing is stereolithography (SLA). In this technique, entire three-dimensional parts are built up by successively printing two-dimensional layers on top of each other. As with all additive manufacturing processes, the design must be created first using a computer-aided design file (CAD). The file is then sliced into a series of 2D cross-sectional layers with a selected layer thickness that gradually add up to the desired 3D structure. The liquid layers become solidified on top of each other until the desired green part is complete. During the printing process the functional groups of the monomers and oligomers are cured and form a stable 3D network structure. [23, 26]

In stereolithography, the resin is exposed to a laser that emits light in the UV range. This can be achieved top-down, with the curing light above the resin, or bottom-up, with the light source beneath the resin tank. [15] The top-down SLA process requires a low-viscosity resin, a large vat and a recoater blade to level the resin, and struggles with the layer thickness. In contrast, the bottom-up setup overcomes these problems but requires a shallow tub with a transparent bottom to allow the induced light to cure the resin. Also, a non-sticking bottom must enable a gentle detachment of the individual cured layer. The building platform is positioned inside the tank, leaving a small gap between itself and the transparent bottom with the thickness of a single layer. After UV-curing, the platform is lifted to peel off the freshly cured layer and allow for new resin to flow between the last cured layer and the bottom of the tank. Since the component is lifted out of the vat, the construction height is not limited to the depth of the vat compared to the top-down construction method. The layer thickness can be precisely controlled as it is determined by the elevation of the printing platform and not by the properties of the resin liquid, resulting in a higher vertical resolution. The laser beam provides the energy required to initiate the photopolymerisation process and form a highly cured and solid polymer. [21, 23] The layer-by-layer polymerisation of the desired pattern can be achieved by controlling the movement of the laser beam. Conventional laser stereolithography uses a light spot with a wavelength of about 355 nm. [15]

Alternatively, stereolithography with digitial light processing (DLP) can be used to cure the individual layers. An imaging projector, a mask-like device, projects the desired image into the photosensitive resin. It uses a wavelength in the UV-range and a digital micro mirror device for the light exposure which makes this method more expensive compared to laser-SLA. [15] The structures obtained have a higher resolution, but the final product size is limited because of the limited dimensions of the patterned light. DLP requires less printing time because each layer is printed at once, regardless of the individual areas. [23] The illustration below (Figure 3) shows the systematic operation of the bottom-up photopolymerisation-based printer setup.

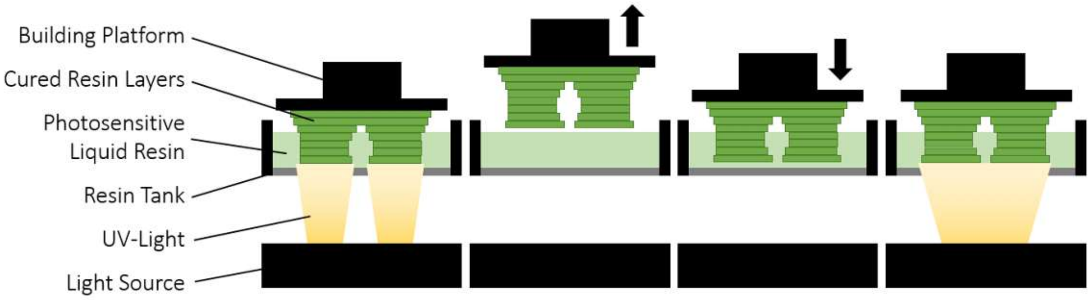

Figure 3: Generic method of operation for a bottom-up SLA 3D printer with DLP. After selective irradiation, the cured layer is gently detached from the bottom of the vat by lifting the printing platform. The resin levels itself within the tank, preparing for the next layer. The platform in lowered, leaving a designated gap. Then the next layer is cured.

The fundamental parameters of the printing process can be divided into technical parameters, such as light intensity and layer thickness, and intrinsic photosensitive parameters, such as penetration depth. These parameters have a significant influence on the geometric accuracy of the manufactured parts. [23] Regarding the design of the printed piece, *Eckel et al.* [24] stated that the design of the printed polymer should be limited to features with a thickness of less than 3 mm in one dimension to avoid shattering during pyrolysis.

Photopolymerisation-based additive manufacturing of SiC-based materials

When aiming at photopolymerisation-based additively manufactured SiC, which is associated with a number of valuable properties, various methods have been reported. By physically blending SiC powders with photocurable polymers, the system is difficult to use for photopolymerisation-based AM. Apart from sedimentation problems, the system exhibits a tendency to reduce the curing depth. This, in turn, can lead to scattering of incident light resulting in structures of poor resolution, severe cracking, low mechanical performance and surface roughness. [15, 27] By increasing the exposure energy during the printing process, *Ding et al.* [26] produced a grey-colored SiC ceramic slurry suitable for DLP 3D printing. Particle size, solid loading and printing parameters thus have a high influence on the printability and quality of the final product. *Essmeister et.al.* [4] developed a novel polymer-derived SiOC/SiC composite system suitable for AM. The proposed system was able to produce specimens with well-dispersed SiC particles in a polymer-derived SiOC matrix with improved mechanical properties.

Alternatively, polymer-derived SiOC can be used for the production of well-defined structures without causing sedimentation during the printing process. [25] Compared to some conventional ceramic materials, PDCs exhibit good thermomechanical properties such as creep, crystallisation and lower sintering temperatures. In addition, due to the relatively low pyrolysis temperature (about 1000 °C), PDCs require less energy than the high sintering temperatures of conventional ceramics. [21]

Eckel et al. [24] and *Hazan et al*. [28] reported UV-curable preceramic monomers used in a 3D printer and that were cured through a patterned mask to form complex structures. The preceramic precursor system (PCP) mainly consists of the modified silicone polymer as well as photosensitive groups such as vinyl or acrylate. *Zanchetta et al.* [25] manufactured a 3D printable system for crack-free polymer derived SiOC ceramics with a strut size down to 200 µm. The structures were obtained by using chemically modified methyl-silsesquioxane dissolved in tetrahydrofuran (THF) and tripropylene glycol monomethyl ether (TPM), as the silicon containing monomers, and 3-(trimethoxysilyl)propyl methacrylat (TMSPM), as a cross-linker to form a photocurable PCP system. [24] Among others, *Schmidt et al.* [29], *Wang et al.* [30] and *Zocca et al.* [31] reported PDC-systems suitable for SLA and DPL printing. *Li et al.* [32] added trimethylolpropane triacrylate (TMPTA) and hexanediol diacrylate (HDDA) as a diluent and monomer to improve the viscosity, curing rate and cured strength of the resin.

The properties and components of the preceramic system influence the properties of the obtained PDC significantly. The photopolymerisation mechanisms also vary with the PCPs used. For example, UV-active preceramic monomers can be obtained by adding epoxy, thiol, acrylate or methacrylate groups to organosilicon polymers. Furthermore, they usually enhance the carbon-carbon cross-linking of the precursor during photopolymerisation resulting in a more stable green body. The disadvantage of these systems is that they suffer from volume shrinkage and they are very sensitive to oxygen contamination. [15] Polysiloxane is mostly used for the fabrication of SiOC ceramics. It is characterised by its low intermolecular forces between the Si-O-Si skeleton and has a high cross-linking ability which results in good thermal resistance. Polysiloxanes used for 3D printed PDCs usually have a carbon content of >20 wt% which is particularly favourable for high chemical and thermal stability in the final ceramics. [12, 15]

In conventional SLA 3D printing, UV absorber and polymerisation inhibitor are added to the preceramic polymer resin to confine the polymerisation and minimize light scattering to maintain the accuracy of the printed part. [12] The extent of photopolymerisation increases with UV illumination until the resin reaches the gel point, where it changes from a liquid to a solid state. The curing depth (Cd) is the depth, at which the energy of the selected light is sufficient to bring the resin to the gel point and convert it into the solid-state. [23]

Additive manufacturing of metal-modified SiOC

With regards to metal modified PDCs, the printability must be considered when developing preceramic precursors. *Ma et al.* [20] manufactured 3D printable metal-modified PDCs by physically mixing the aqueous metal precursor solution with the preceramic polymer without the addition of a complexing agent. The cured green bodies were pyrolyzed under an inert argon atmosphere at 1000 °C for 2 h. *Fu et al.* [21] fabricated metal-modified polymer-derived SiOC ceramics for detailed SLA 3D printed structures by using a methyl-silsesquioxane polymer, prepared through the sol-gel method. The polymer was dissolved in TPM and THF and mixed with TMSPM as a cross-linker. The metal alkoxides used were complexed with methyl acrylic acid (MAA) and then mixed with the pre-hydrolysed polymer, the reactive diluent trimethylolpropane triacrylate (TMPTA), to lower the viscosity and enhance the curing strength. THF was evaporated and a photoinitiator was added. The cured structures, processed with a DLP SLA 3D printer, were pyrolyzed in a range of 500-1200 °C for 1 h under nitrogen atmosphere. After pyrolysis at 1200 °C the ceramic parts exhibited a mass loss of 56% and linear shrinkage of 35%.

3 Aims

The global climate crisis makes research of alternative energy sources inevitable. The CO_2 methanation reaction, in which CO_2 and H_2 form CH_4 and H_2O, is a promising option. Due to its high activity and selectivity for methane, Ni is the most common catalyst for this reaction. The main disadvantage of Ni as a catalyst is the rapid deactivation that occurs under the given reaction conditions due to sintering of the active phase. To improve the stability, great efforts are being made to find new support materials and manufacturing processes. The focus is primarily on the cooperation and distribution of the active Ni phase within the ceramic catalyst support material. The chosen approach is the use of Ni-modified polymer-derived ceramics, shaped by photopolymerisation-based additive manufacturing.

The developed resin must …

… be photosensitive with a short time to gel point
… homogeneously distribute the added Ni-sites
… have a low viscosity to be suitable for additive manufacturing
… result in stable specimens after printing, postprocessing, and pyrolysis

The produced specimens must …

… have a high SSA
… have well distributed and accessible Ni-sites

The main objective of this work is to investigate to what extent the produced material exhibits catalytic activity towards CO_2. For this purpose, a comparison to a Ni-free reference material will be made.

In addition, the resin as well as the polymer-to-ceramic transformation and the resulting specimens will be studied to gain a more precise understanding of the material system.

4 Experimental

The next section describes the preparation of a Ni-modified preceramic polymer system suitable for AM and with sufficient stability in all following processing steps. Furthermore, the implementation of additive manufacturing via vat-based photopolymerisation is described. Finally, the characterisation of the resin, the thermal polymer-to-ceramic transformation and the resulting specimens are described.

4.1 Preparation of Ni-modified preceramic polymer

As photocurable matrix polymer, a polysilsesquioxane system, introduced by *Zanchetta et al.* [25], consisting of commercial methyl-silsesquioxane (MK, Silres MK, Wacker-Chemie) and 3-(trimethoxysilyl)-propylmethacrylat as a cross-linker (TMSPM, 98%, Sigma-Aldrich) were used. In a typical experiment, 40 g of methyl-silsesquioxane powder (MK) were dissolved in 20 g of tri(propyleneglycol)-methylether (TPM, Formlabs), and stirred magnetically at 150 rpm in a water bath at 70 °C. When fully dissolved, 10 g of TMSPM were added as a cross-linker and stirred at room temperature for 1 h at 250 rpm. Subsequently, 0.2 g of aqueous hydrochloric acid (HCl, 37%, Sigma-Aldrich) as the acid selected for the hydrolysis was mixed with 0.8 g of TPM and then slowly added into the flask with constant stirring. The mixture was hydrolysed at room temperature for 20 h (stirred at 250 rpm). The resulting volatile substances were then evaporated by a rotary evaporator at 45 °C and 100 mbar for 2 h. Finally, 2% Genorad*16 (G*16, RAHN) were added as a stabilizing agent and thoroughly mixed into the resin (PSO) using a planetary mixer (Thinky, ARE-250) for 4 min at 2000 rpm, followed by 10 min at 800 rpm. Figure 4 shows the proposed structure of a MK-TMSPM resin after hydrolysis, as proposed by *Zanchetta et.al.* [25].

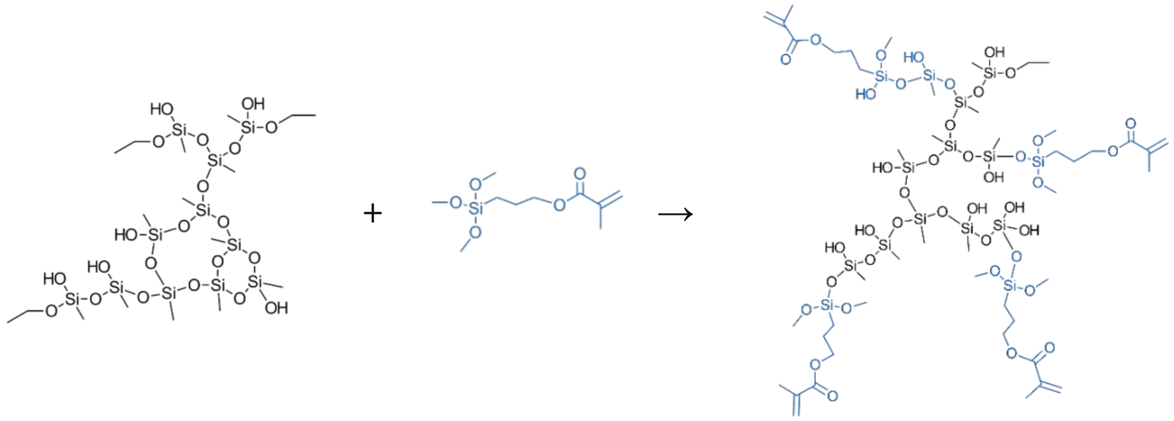

MK TMSPM

Figure 4: Proposed structure of MK-TMSPM resin after hydrolysis between the MK siloxane and TMSPM, after [25]

To prepare the Ni-modified resin, nickel (II) nitrate hexahydrate (NiN, Merck) was first dissolved in tetrahydrofuran (THF, ≥99,9%, Riedel-de Haen). The amount of NiN was calculated to correspond to the desired amount of nickel in the final pyrolyzed structure, which was varied resulting in final Ni contents between 3 wt% and 5 wt%. When fully dissolved, methacrylic acid (MAA, 99%, Thermo scientific) was added as a complexing agent in a molar ratio of 1:2 between Ni and MAA. The weight amount of THF added was at least three times the amount of MAA to ensure complete dissolution. The green solution was then stirred for 1 h at room temperature at 250 rpm. To ensure that the two forming phases did not separate, but were present as evenly distributed spherical micelles, polyoxyethylene (20) sorbitan monolaurate (Tween 20, Aldrich) as a surfactant to promote micelle formation was added and stirred for 30 minutes. The amount of Tween 20 was calculated to correspond to 5% of trimethylolpropan-trimethacrylate (TMPTMA, technical grade, Sigma-Aldrich), which was added at a later time. The photocurable matrix preceramic polymer (PSO) was added and stirred into the green solution at 100 rpm. Once all components were completely combined, the resin was stirred over night at 150 rpm. The amount of added PSO depended on the desired amount of TMPTMA. In this state the resin can be stored for multiple days without drawbacks in the following steps.

Before the AM process, the desired amount of TMPTMA was added as a reactive diluent, and the mixture was stirred for 20 minutes at 300 rpm. At this stage, the TMPTMA content was varied between 10 wt% and 20 wt%. If aliphatic urethane dimethacrylate (UdMA, RAHN) was to be added in addition to the preceramic polymer, it was added along with the TMPTMA and stirred thoroughly. UdMA was added to increase the porosity as a combustible filler. To further stabilize the resin, hydroquinone (HQ, 99%, Merck) was added simultaneously with the acrylates. The added amount of hydroquinone was 10 mg per mole of double bonds in the final formulation. The flask was then placed in the rotary evaporator at 200 rpm for 1 h at 40 °C and 60 mbar to evaporate volatile species and residual THF which may interfere with the printing process.

Before the printing process, 1% Phenylbis (2,4,6-trimethylbenzoyl) phosphine oxice (BAPO, Genocure*BAPO, 97%, RAHN) was added as a photoinitiator in yellow light. The initiator was completely dissolved and mixed into the resin by using a planetary mixer (4 min mixing at 2000 rpm, 10 min mixing at 800 rpm, 2 min mixing at 2000 rpm followed by 10 min defoaming at 800 rpm). The defoaming had to take place immediately before the printing process and was crucial for the quality of the green body, as remaining air bubbles negatively affect the structural integrity.

In Figure 5 the formulation of the relative gravimetric composition of the final preceramic polymer, aiming at 5 wt% Ni in the pyrolyzed structure, is shown. The sample denotation 5Ni10T5U indicates the Ni content of the final specimen (**5**Ni10T5U), as well as the percentage share of added TMPTMA (5Ni**10**T5U) and addition UdMA (5Ni10T**5**U). Within this work the Ni content varies between 3-5 wt%, the TMPTMA content between 10-20 wt% and the additional 5 wt% where either added or omitted entirely.

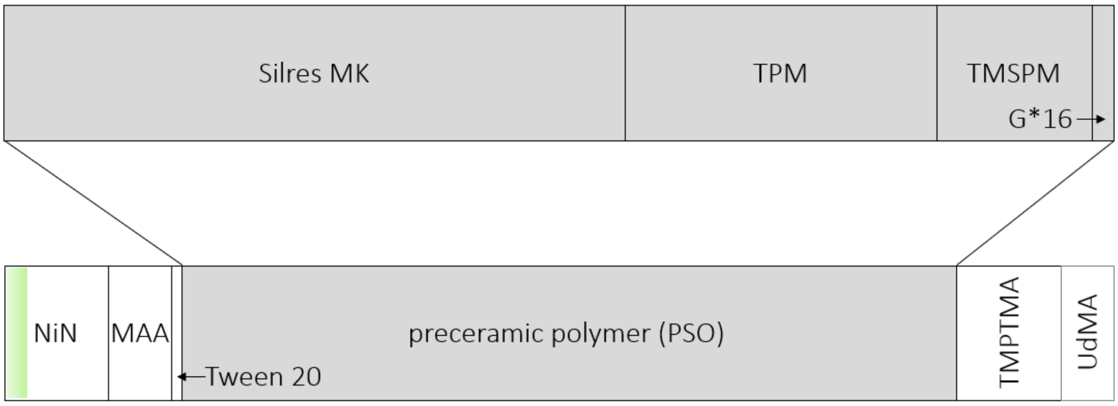

Figure 5: Exemplary relative gravimetric composition of the preceramic polymer (top) and the final Ni-modified resin 5Ni10T5U (bottom). The green area symbolises the amount of Ni present in the resin.

4.2 Implementation of additive manufacturing and pyrolysis

In this work the stereolithography-based additive manufacturing process was chosen as the AM method. The method is based on selective layer by layer curing of the photosensitive preceramic polymer resin by means of a LED technology, according to a virtually sliced CAD model. [25]

The CAD file was adapted using the Blender program (Version 3.0) and imported into the ChituBox program (Version 1.9.2), where supports were added as needed. Figure 6 shows the CAD file before and after the addition of support structures.

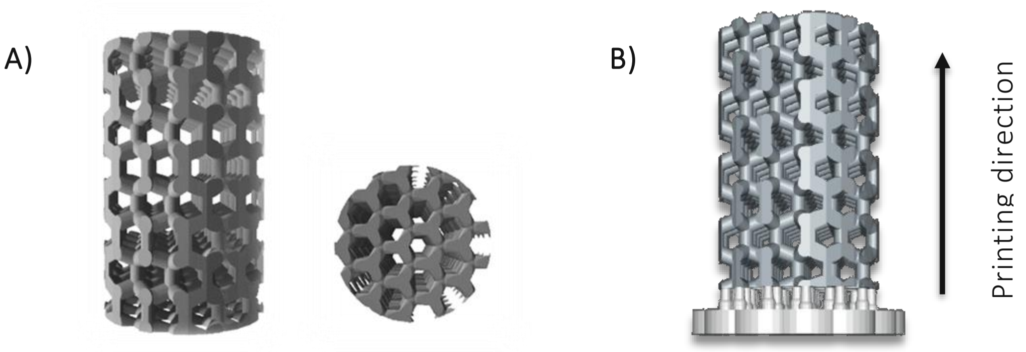

Figure 6: 3D grid structure. (A): 3D CAD file of the grid structures in different views; (B) grid structure after adding the support; with the indication of the printing direction

The final structures with the added supports were then sliced into individual patterned printing layers according to the chosen printing parameters. An example of selected printing layers is shown in Figure 7.

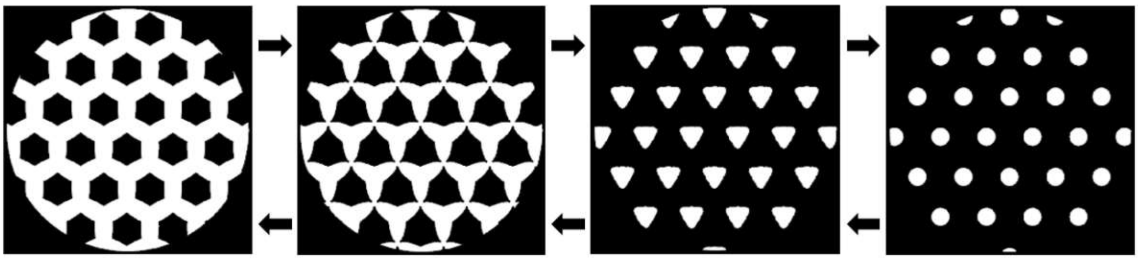

Figure 7: Exemplary patterned printing layers of the grid strucutres for the additive manufacuring on the desktop 3D printer used.

A 3D desktop printer Elegoo Mars 2 Pro was used for AM. The light exposure was realized with a 2K monochrome LCD screen with LEDs at a wavelength of 405 nm and a measured intensity of 14,5 mW/cm^2 (14 mW/cm^2 with the vat in place).

At the beginning of the printing process, first the printing platform and the resin tank were prepared. The platform was masked with a wide adhesive tape. The resin tank was equipped with a non-sticky foil (ELEGOO, FEP 2.0 Release Film Liner, with a thickness of 0.127 mm) on the bottom of the tank, which enables the gentle detachment of each cured layer. The platform was then calibrated and the tank installed. The defoamed resin was then gently poured into the tank and the light cover was placed on top before the printing process was started. Table 1 shows an example of the chosen printing parameters. The exposure time was adjusted to the needs of the resin used.

Table 1: Exemplary printing parameters for 5Ni10T grid structures on a Elegoo Mars 2 Pro 3D desktop printer

Layer Height	0.025 mm	Bottom Lift Distance	5 mm
Bottom Layer Count	5	Lifting Distance	10 mm
Exposure Time	18 s	Bottom Lift Speed	60 mm/min
Bottom Exposure Time	60 s	Lifting Speed	30 mm/min
Light-off Delay	10 s	Retract Speed	210 mm/min
Bottom Light-off Delay	12 s		

After the printing process was completed, the cured structures were gently detached from the printing platform, using a razor blade. The components were then placed in a vessel with TPM for 10 minutes in an ultrasonic bath (Emmi-12HC, EMAG). Subsequently, the supports were separated from the grid structure and compressed air was used to remove any residual uncured resin. This cleaning step was then repeated. The clean structures were then carefully dabbed dry, post-cured for 5 min under light (405 nm) and stored in a desiccator until pyrolysis was carried out.

To complement this, one print job was also carried out at Lithoz GmbH via lithography-based ceramic manufacturing (LCM). After preparing the resin and the final evaporation step, the photoinitiator (BAPO) was added at Lithoz. Further processing steps regarding printing and postprocessing were executed by Lithoz. The regained samples were then, equal to all other specimens, pyrolysed as follows.

The pyrolysis was conducted in a 3-zone split tube furnace (HZS 12/600, Carbolite Gero) in flowing Ar atmosphere (0.6 l/min). In addition, one experiment each was carried out with dried Ar (using a molecular sieve and Cu chips as oxygen getter) and with a reductive atmosphere, consisting of 5% H_2 in Ar.

The structures were pyrolyzed at temperatures varying from 600 °C to 800 °C for 2 h. The temperature program included a first step up to 200 °C (0.5 °C/min, 2 h dwell time). Subsequently the samples were heated to 500 °C (1 °C/min, 1 h dwell time). Finally, the furnace was heated to the final temperature, between 600 and 800 °C (1 °C/min, 2 h dwell time) before being cooled down to room temperature (2 °C/min).

4.3 Characterisation

In this section, the characterisation of the resin, the thermal polymer-to-ceramic transformation and the resulting specimens are described.

4.3.1 Chemical properties

For polymer characterisation, attenuated total reflectance Fourier-transform infrared spectroscopy (ATR-FTIR) was conducted on a Bruker Vertex 70v with a platinum diamond ATR unit. The interferometer compartment and optical unit were flushed with dry air. The setup was coupled with a mercury cadmium telluride (MCT) detector, cooled with liquid nitrogen. Data analysis was executed using OPUS software. The spectra were recorded from 850 to 4000 cm^{-1} at a resolution of 4 cm^{-1}.

The distribution of the micelles within the resin was examined in transmitted light mode on a three-dimensional microscope (VHX-5000, KEYENCE), where the resins were applied to a microscope slide.

The photopolymerisation was investigated using a real time IR-photorheology setup, as described by *Gorsche et al.* [33], to obtain information on the rheological properties and the time-resolved double bond conversion. The measurements were carried out at the Institute of Applied Synthetic Chemistry at TU Wien. The setup consisted of a Bruker Vertex 80 FTIR spectrometer equipped with a near infrared (NIR) optic, coupled with a rapid scan module and an Anton Paar MCR302 WESP rheometer. The measurement parameters were chosen to best simulate the conditions during AM. A broadband Exfo OmniCure 2000 UV-light source, emitting between 270 nm and 550 nm with an intensity of 15.4 mW, was chosen in combination with an external MCT IR detector (Burker DigiTect). The rheometer was equipped with a parallel plate steel measurement system with a diameter of 25 mm. The sample thickness was set to a gap of 0.05 mm between the plate and the optical window. All measurements were carried out at room temperature. Before UV irradiation, the respective resin samples were sheared with a strain of 1% and a constant shear rate of 1 Hz. To protect the optical window, an adhesive polyethylene tape from TESA (4668 MDPE) was used. To ensure no interference with the IR signals from the measured resins, the tape was included in the background measurements and subtracted from the results. Measurements were performed in triplicate. The data of the NIR measurements was analysed with the OPUS software. The double bond conversion (DBC) values were smoothed using an 8-point moving average. In addition to that, the values from the storage and loss modulus were smoothed using a 5-point moving average. The final double bond conversion (DBC_{final}), which describes the extent of photopolymerisation, was determined by calculating the mean value of the last 30 measurement points before smoothing the curve. The time schedule of the measurement is shown in Table 2.

Table 2: NIR-Photorheology measurement settings: tm, measuring time; ti, time interval between measurement points; P, count of measurement points

t_m (s)	t_i (s)	P ()	Oscillation	IR-detector	UV-light
60	1	60	1%, 1 Hz	off	off
65	1	5	1%, 1 Hz	on	off
365	0.2	300	1%, 1 Hz	on	on
605	1	240	1%, 1 Hz	on	on
607	1	2	off	on	off
609	1	2	off	off	off

In order to adjust the exposure time for the printer, the curing depth was measured with varying exposure times on the SLA desktop printer itself, using a sliding gauge. This ensured the exact same light intensity and time settings during these measurements and the actual printing process.

Thermogravimetric analysis (TGA) and differential thermal analysis (DTA) were simultaneously conducted using a NETSCH STA 449 C instrument with a NETSCH TASC 414/4 controller unit, controlled via the STA 449 C on 18 TASC 414_4 software. A ramp of 5 K min^{-1} from 30 °C to 1500 °C under flowing argon atmosphere (50 mL min^{-1}) was chosen for all measurements, the sample amount consisting of 30-40 mg. When measuring solid samples, they were chopped with a blade before starting the measurement. The data analysis was executed in the Proteus Analysis software.

In addition, the ceramic yield and the linear shrinkage were determined by a quadruple determination with the aid of an analytical balance and a vernier caliper, respectively.

Powder X-ray diffraction (XRD) was performed with a PANalytical XPert Pro MPD using CuK$\alpha_{1,2}$-radiation at a diffraction angle 2Θ between 5° and 100°. The setup was equipped with a Bragg-Brentano geometry and a X'Celerator semiconductor detector (2.1°), in a distance of 240 mm from the sample. For data analysis, PANalytical Data Viewer and Highscore+ were used. For preparation, the respective samples were ground in a mortar and then applied to a Si-Waver as a sample carrier. Finally, the powder was pressed down to the desired measuring height and straightened with the help of a glass plate.

X-ray fluorescence spectroscopy (XRF) was carried out using a Malvern PANalytical AXIOS advanced PW 4400/40 spectrometer. For this purpose, a pyrolysed plate was fixed in the measuring area with the aid of adhesive film.

In order to obtain more precise information regarding the surface and bulk composition and the bonding states, surfaces and fracture surfaces were examined using x-ray photoelectron spectroscopy (XPS). The measurements were executed by the analytical instrumentation center (AIC) at TU Wien with the use of a custom X-ray photoelectron spectrometer from SPECS GmbH, equipped with a μFocus 350 (Al-Kα (4)) as a monochromatic X-ray source and a PHOIBOS 150 WAL (SPECS) as a hemispherical detector. Pass energies of 100 eV and 30 eV (100 eV/180 eV for Ni 2p) with a step width of 0.5 eV and 50 eV were used, respectively (excitation energy: 1486.6 eV, beam energy and spot size: 100 W onto 400 µm; mean angle: 51° to sample surface normal; base pressure: $1 \cdot 10^{-9}$ mbar, pressure during measurements). Ar-ion sputtering was carried out with a SPECS IQ 38/11 ion gun using 3 kV acceleration voltage and $2 \cdot 10^{-7}$ mbar Ar partial pressure at around 2 nm/min. The analysis depth is typically around 7-10 nm. Data analysis was performed using CASA XPS software, employing transmission corrections, Shirley/Tougaard backgrounds [34, 35] and Scofield sensitivity factors [36, 37]. Deconvolution of spectra was carried out using Gaussian-Lorentzian peaks (GL(30)). Assignment of different components was primarily done using reference data [38, 39].

As a further method for determining the composition of the surface, inductively coupled plasma mass spectrometry (ICP-MS) measurements were executed. The parameters for the MS (quadrupole iCap Qc, ThermoFisher Scientific, Germany) and the laser (frequency quadrupled J200 Tandem LA/LIBS system, Applied Spectra, Inc., Fremont, Ca, 266 nm, 4 ns pulse length) can be found in Table A 1 and Table A 2 in the appendix, respectively. The method was described in more detail by *Herzig et al.*[40]. For quantification, a 5 ppb spike for Ni and a 50 ppb spike for Si in a liquid standard were used.

For elemental analysis of carbon and oxygen contents, two different setups were utilised. For the determination of the carbon content, a LECO CS230 instrument was used. To calibrate the device, steel pellets (carbon, sulfur & nitrogen in steel LCRM, part No. 502-916) were added into the ceramic crucible (LECO, part No. 528-018) as a reference material. Tungsten chips (LECOCEL, part No. 763-266) were added as an accelerator to facilitate ignition of samples for combustion. To determine the oxygen content in the samples, a LECO TC400 instrument was used. The measurements were conducted in a graphite crucible (part No. 775-433) with an inner crucible (part No. 775-431). As a reference material an iron powder (carbon, sulfur, oxygen, nitrogen & hydrogen in iron powder LCRM, part No. 502-702) was used. To prevent the atmospheric oxygen from interfering with the measurement results, the powder was weighed into tin capsules (LECO, part No. 501-059) which were then sealed. The measurements themselves took place in helium atmosphere.

4.3.2 Morphology

In this work, the morphology and macrostructure of the printed and pyrolyzed lattices were characterised with a digital microscope (VHX-5000, KEYENCE). In addition, cross-sections were prepared and inspected with an optical microscope (GX51, Olympus). Cross-sections were manufactured by embedding the pyrolyzed structures in a clear epoxy resin (Struers, Epofix) under vacuum, ensuring that no air was trapped inside the lattice. The samples were then ground (120 µm abrasive disk) and polished with a polishing machine (Struers Tegramin-30). Diamond pastes (15 µm, 6 µm and 1 µm particle size) were used as grinding media in combination with an alcohol-based lubricant (AB Technics).

Scanning electron microscopy (SEM) images of surfaces, fracture surfaces and polished cross-setions were recorded using a FEI ESEM Quanta 200. In high vacuum an ETD detector was used for imaging the secondary electrons and a dual BSD detector for the backscattered electrons. Because of the poor conductivity of the Ni-free reference samples, they needed to undergo Au-sputtering with AGAR Sputter Coater sample preparation system.

Transmission electron microscopy (TEM) measurements of a prepared sample were recorded at the University Service Centre for Transmission Electron Microscopy (USTEM) at TU Wien, using a TECNAI F20 with a field emission gun (X-FEG) as an electron source at 200 kV. The sample was prepared by cutting a pyrolyzed platelet into small pieces using a saw. The sample was then places on a sample holder and grinded to achieve a flat surface. The platelet with the flat surface facing down was then glued onto a Cu-ring. The surface of the sample was then grinded and polished using abrasive disks down to a grain size of 0.1 µm. The edge of the prepared sample was then polished using precision Ar-ion polishing (PIPS). The scanning transmission electron microscope (STEM) images, with a resolution of 0.14 nm, were recorded by a Gatan DigiSTEM II detector. High resolution-TEM images with a resolution of 0.24 nm were recorded using a Gatan GIF Tridiem. In addition, an EDAX-Ametec Apollo XLTW SDD was used to determine phase composition via energy-dispersive X-ray spectroscopy (EDX) with an energy resolution of 0.7 eV and a line resolution of 128 eV. For recording the diffraction pattern, a setup with a wider collimator was chosen (TECHNAI G20 with a LaB_6 emitter and a resolution of 0.24 nm (TEM) and 1 nm (STEM)). Imaging was performed with a Gatan GIF 2001. The images received from the TEM measurements were also used to determine the distribution of the Ni particles in the bulk material.

To determine the specific surface area, the evaluation of nitrogen adsorption at -196 °C according to BET theory with 5 measurement points was conducted. The measurements were performed on a Surface Area and Porosity Analyzer ASAP 2020 from Micromeritics. To minimize the dead volume, a glass rod was added. Depending on the expected SSA, between 100 and 200 mg of each sample were weighted in and degassed in vacuum for 4 h at 350 °C prior to measuring.

4.3.3 Catalytic activity

The catalytic activity and selectivity were determined on a specially constructed test rig described by *Szoldatits* [41], who also conducted all measurements. The reaction setup is depicted in Figure 8.

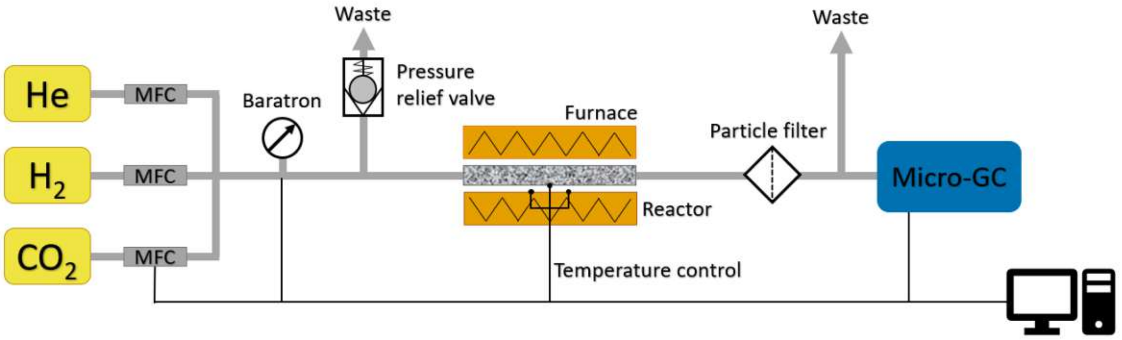

Figure 8: Set-up of the custom catalysis test rig for the determination of the CO_2 conversion and CH_4 selectivity. The assembly consists of the gas supply (with He, H_2 and CO_2), the furnace and a downstream Micro-GC. (kindly provided by Eva Szoldatits [41])

First, ether 1 g solid catalyst cylinders (1.6-1.8 mm in diameter and 3.2-3.7 mm in height, depending on the pyrolysis temperature) or a mixture of 1 g milled catalyst and 1 g Al_2O_3 (fine powder with round grain) as a filler material were pre-treated for 4 h at 400 °C in 50 ml/min gas flow consisting of 10 vol% hydrogen (H_2) in helium (He).

Afterwards the gas composition was changed to the reaction gas (10 vol% CO_2, 40 vol% H_2 and 50 vol% He) to evaluate the catalytic activity. The measurements were conducted at temperatures between 200 °C and 400 °C (step size of 50 °C) with dwell times of 2 h for each step. To exclude possible time effects, the temperatures were not measured consecutively. The temperature program is depicted in Figure 9.

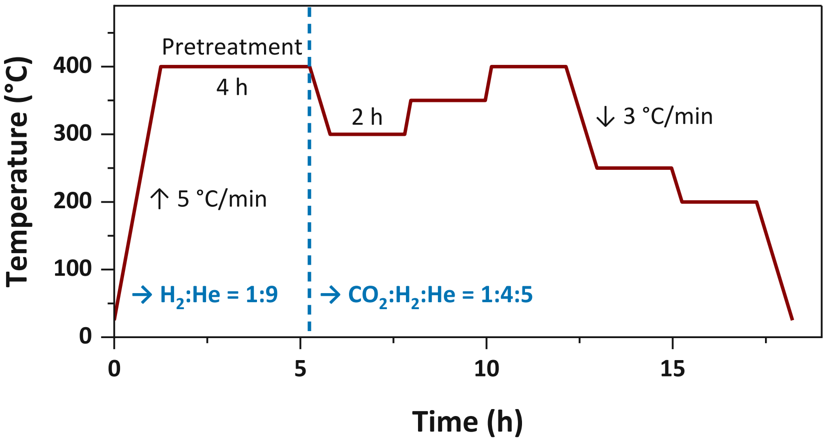

Figure 9: Temperature schedule for the reductive pre-treatment and the thermal CO_2 methanation with gas compositions, dwell times and heating rates (kindly provided by Eva Szoldatits [41])

The composition of the outlet gas was analysed using a Micro GC (Micro GC Fusion, Inficon). With the composition of the outlet gas, the CO_2 conversion and the selectivity to methane (CH_4) were calculated using the Equations (A 1) and (A 2), which can be found in the appendix.

5 Results and Discussion

In the following chapter all obtained results are described. First, the preceramic resin and the finished printed structures are described, followed by the pyrolysed components and the pyrolytic transformation of the material. Finally, the catalytic activity in respect to the CO_2 methanation is described.

Not all characterisation methods were carried out with each individual system. This is addressed separately in the individual sections.

5.1 Polymer characteristics

In a first step, the characteristics of the material in the polymer state, ranging from the starting materials to the modified precursors, were determined. Additionally, a closer look was placed on photopolymerization reaction as well as the characteristics of the additively manufactured parts before the pyrolytic conversion treatment.

5.1.1 Resin characteristics

Attenuated total reflectance Fourier transform infrared (ATR-FTIR) spectroscopy was performed with the resins without photoinitiator and polymerised additively manufactured platelets. The measurements were carried out with different sample formulations. First, the Ni-modified samples with 10 wt% TMPTMA as a reactive diluent (5Ni10T) and the according resin with the addition of 5 wt% UdMA (5Ni10T5U) were investigated. The respective reference material without any Ni (Ref10T and Ref10T5U) were also analysed.

Since the signals of CO_2 from ambient air and the oscillation of the ATR crystal lie in the wavenumber range between 1850 and 2400 cm^{-1}, this range was masked out in all subsequent spectra.

The spectra of all educts were recorded separately and compared with the photocurable preceramic polymer (PSO) without any Ni and the prepared resin for 5Ni10T, respectively. For these comparisons the focus was set on the main components, meaning MK, TPM and TMSPM for the basic polymer system and, additionally, NiN dissolved in THF, MAA and TMPTMA for the Ni-modified preceramic polymer (5Ni10T-resin).

Figure 10 shows FTIR-spectra of the starting compounds as well as the resulting preceramic basic polymer (PSO). The corresponding structures are also shown on the right. Since the information content is greater at lower wavenumbers up to 1850 cm^{-1}, the scaling of the x-axis was adjusted accordingly and is therefore different on both sides of the axis discontinuity. For this, and all subsequent spectra the signals were assigned according to *Socrates* [42].

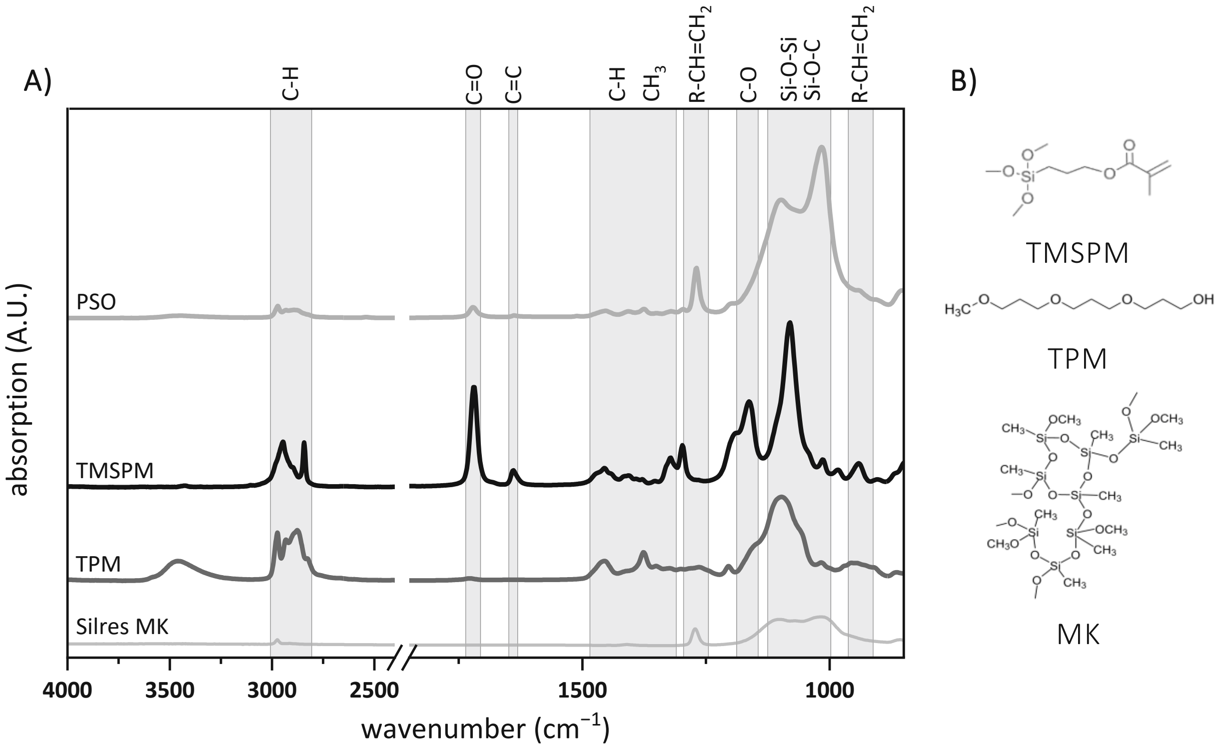

Figure 10: (A) ATR-FTIR spectra of the preceramic polymer resin (PSO) and its main components MK, TPM and TMSPM. (B) Molecular structures of the respective main components for the 5Ni10T resin, corresponding to the adjacent spectra.

The Si-O-Si and Si-O-C stretching vibrations are located between 1010 and 1090 cm^{-1} and 1000-1180 cm^{-1}, respectively. TPM shows the expected C-H stretching (2875-2975 cm^{-1}) and deformation (1370 cm^{-1}) vibrations in addition to strong C-O vibrations at 1100 cm^{-1}. In addition to C-H and C-O vibrations, TMSPM shows C=O stretching vibrations at 1716 cm^{-1} and Si-O-C vibrations at lower wavenumbers. The finished preceramic polymer (PSO) had strong signals from Si-O-Si and Si-O-C vibrations and also shows the C-O-C vibrations at around 1100 cm^{-1}.

Figure 11 shows FTIR spectra of the starting compounds used for the Ni-modified polymer system (PSO, NiN dissolved in THF, MAA and TMPTMA), as well as the resulting 5Ni10T-resin.

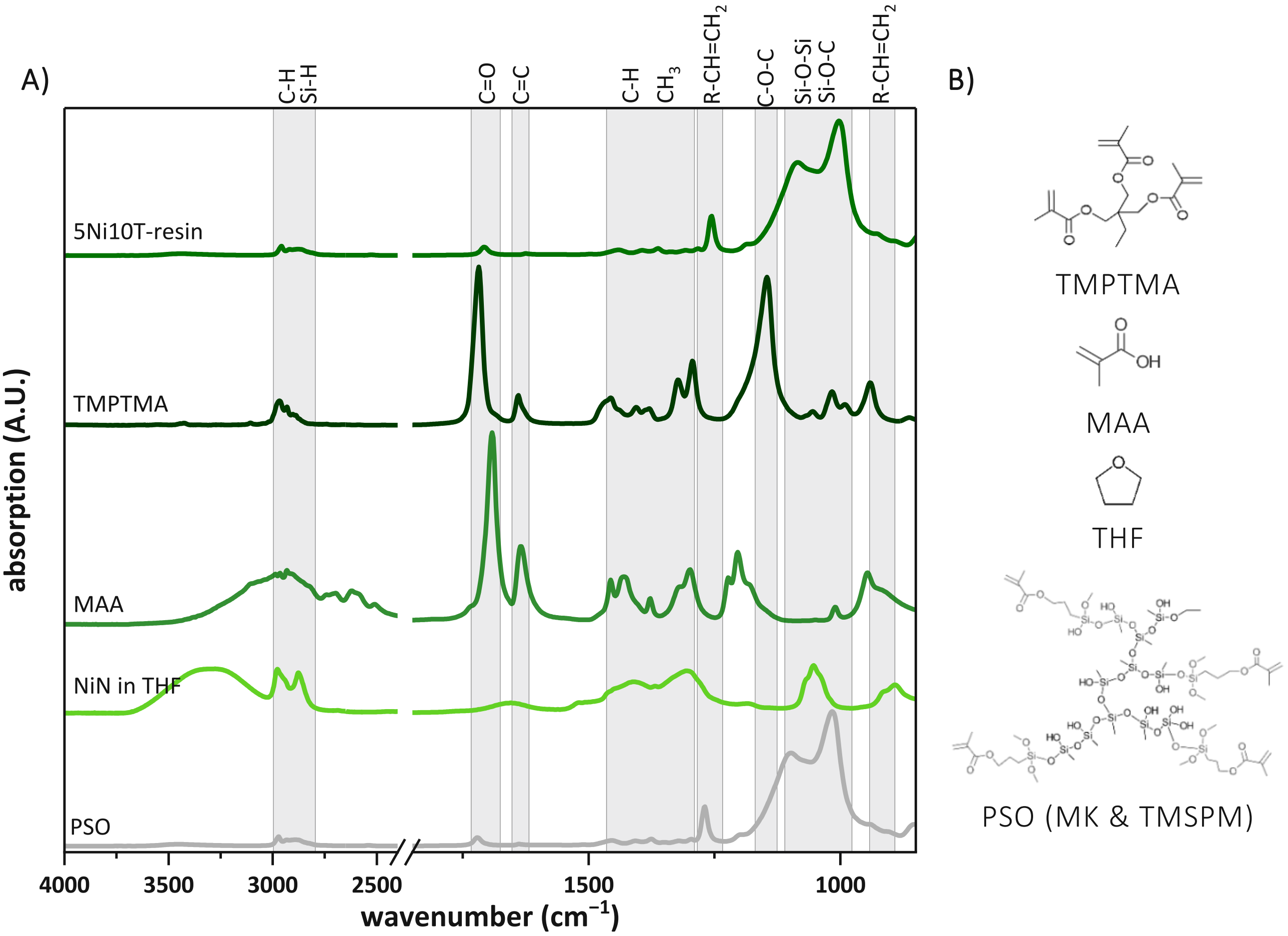

Figure 11: (A) ATR-FTIR spectra of the preceramic polymer resin (PSO) and its main components MK, TPM and TMSPM. (B) Molecular structures of the respective main components for the 5Ni10T resin, corresponding to the adjacent spectra.

At higher wavenumbers, the signals of asymmetric CH_3 stretching vibrations and Si-H vibrations (both around 2970 cm^{-1}) and C-H stretching vibrations (2925 cm^{-1}) of the organic residual groups are visible. TMPTMA as well as MAA show the expected strong signals at 1690-1720 cm^{-1}, corresponding to C=C stretching vibrations. Both molecules show the expected signals of C-H, C=C and C=O bonds with the addition of the C-O-C vibrations for TMPTMA at 1140 cm^{-1}.

There is no indication for a complexation of Ni with MAA. However, a significant amount of THF was necessary to dissolve the mixture after the addition of MAA, indicating that there was interaction between the dissolved NiN and the added MAA. A possible bonding between Si and Ni, which, if present, would show up at low wavenumbers and with a low intensity, could not be detected.

Figure 12 shows a comparison between ATR-FTIR spectra of the initial 5Ni10T resin and the cured 5Ni10T material.

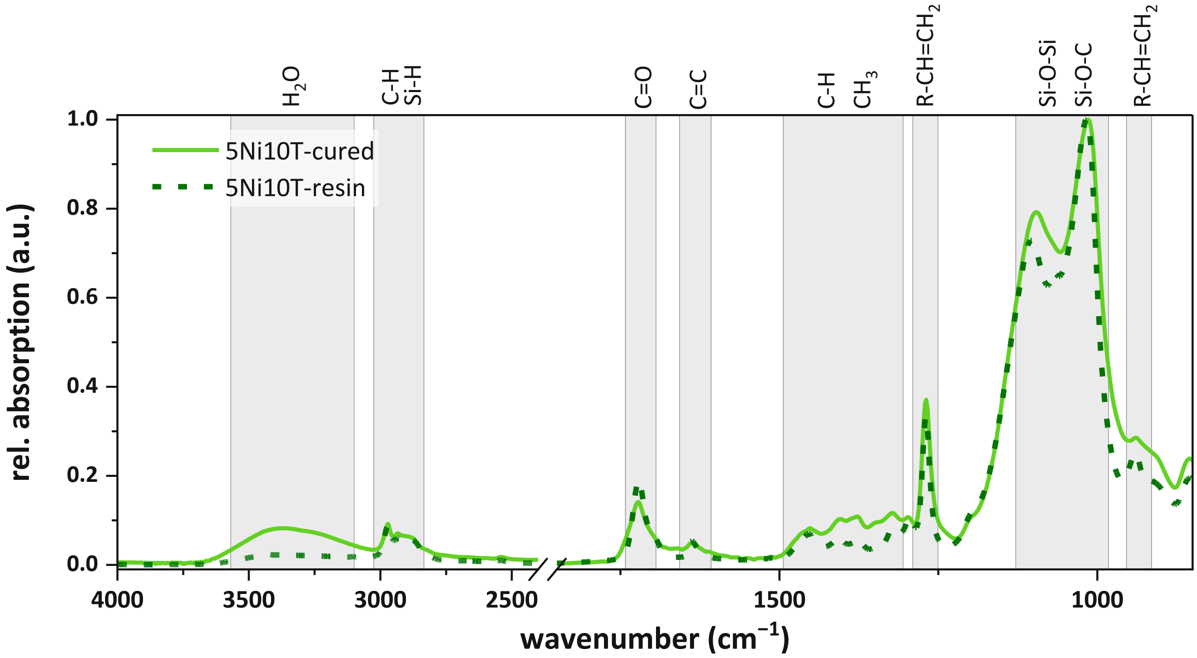

Figure 12: ATR-FTIR relative absorption spectra of sample 5Ni10T as resin (···) and after photopolymerisation through printing (—), normalized to the highest signal. Spectra were recorded between 4000-800 cm^{-1}.

Overall, the resin shows slightly lower signals than the cured sample. The peaks assigned to the C=C bond at 1640 cm^{-1} slightly decrease in the cured sample, indicating the polymerisation of the double bonds provided by TMSPM, TMPTMA and MAA. The peak at 940 cm^{-1}, originating from the vinyl groups, also widens after curing.

Figure 13 shows a comparison between ATR-FTIR spectra of the cured samples of the formulations 5Ni10T and 5Ni10T5U and their respective reference Ni-free materials Ref10T and Ref10T5U.

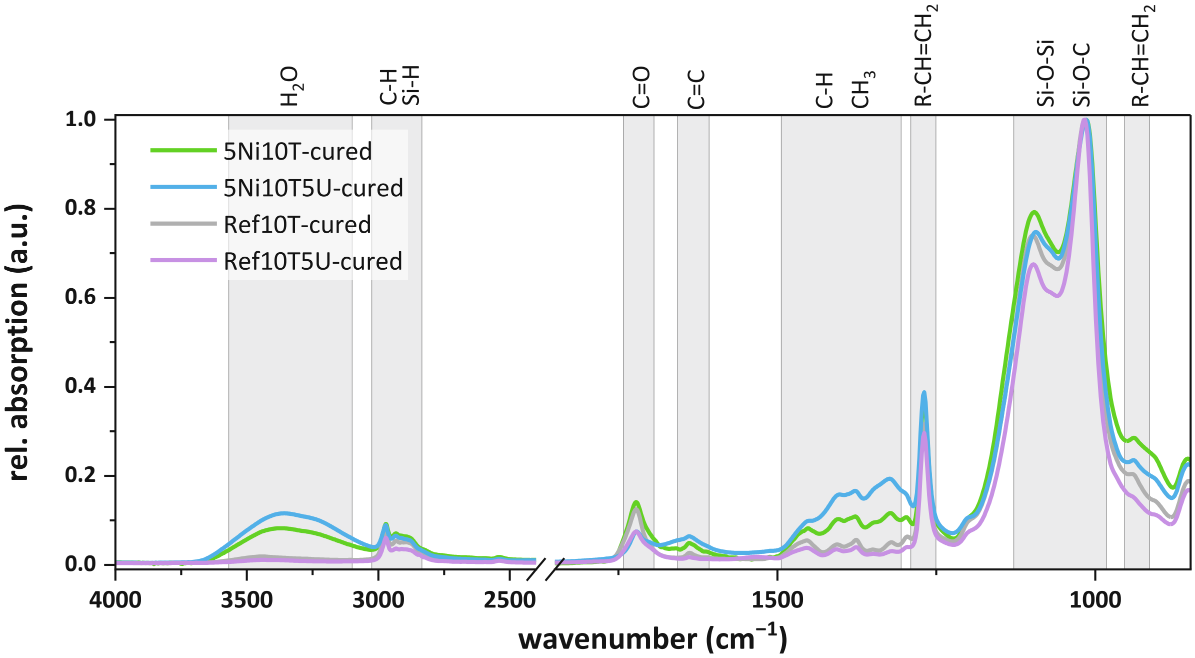

Figure 13: ATR-FTIR relative absorption spectra of cured samples 5Ni10T (green), 5Ni10T5U (blue), Ref10T (grey) and Ref10T5U (purple), normalized to the highest signal. Spectra recorded between 4000-800 cm^{-1}.

The Ni-modified resins show a higher signal assigned to water. This is a result from the Ni(II)nitrate hexahydrate, added as the Ni precursor. The absence of the precursor in the Ni-free reference resin leads to a significantly lower water signal. Furthermore, the reference materials show slightly reduced signals in the range between 1300-1500 cm^{-1}, where mainly vibrations of organic groups are present.

In addition, the occurring phase separation was investigated more closely, using the Keyence VHX-5000 microscope. It was found that a higher Ni concentration (and therefore more MAA), as well as a larger amount of TMPTMA, lead to a stronger phase separation and therefore more micelle formation. The secondary phase was stabilized as small, spherical micelles by the addition of 5 wt% Tween20, calculated to the amount of added TMPTMA (corresponding to 0,5 wt% of the final resin for most formulations). The use of a surfactant was necessary to obtain spherical micelles, as opposed to irregular bicontinuous networks. Furthermore, the added Tween20 delayed the separation of the two phases into individual layers.

Without the addition of Tween20 as a surfactant, the two phases quickly separated into individual layers. Since the darker phase does not polymerise but forms the inside of the micelles, such a strong layer formation is an obstacle for a successful printing process.

One exemplary image of the formed spherical micelles in the 5Ni10T resin can be seen in Figure 14.

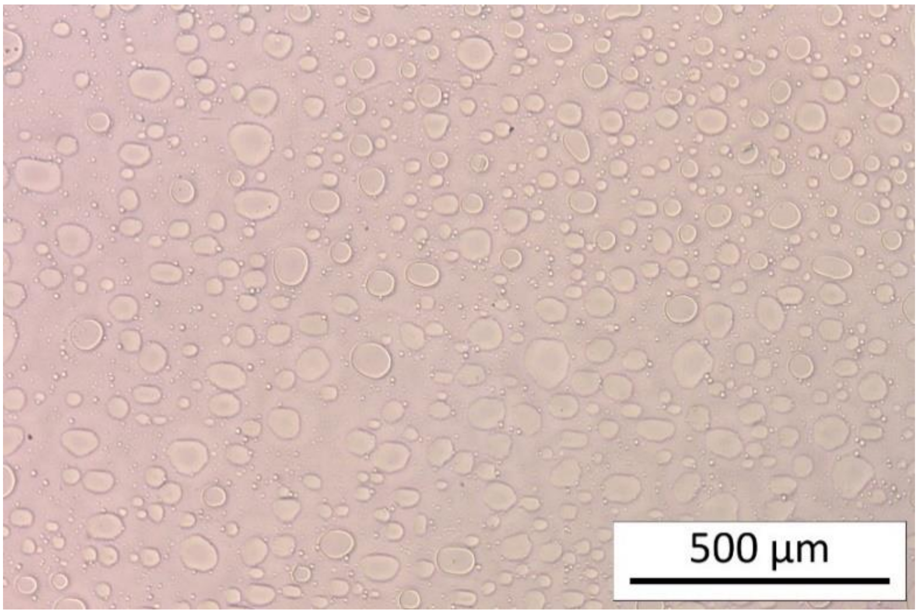

Figure 14: Transmitted-light microscope image of the 5Ni10T resin, with the exhibiting phase separation being stabilized by 5 wt% Tween20, with respect to the amount of added TMPTMA. Before microscopy, a drop of resin was sandwiched between a microscope slide and a cover platelet.

Moreover, phase separation into well-distributed spherical micelles was stabilised by adding hydroquinone (HQ), so that only one turbid phase was formed, and no layer formation occurred over time. (Figure 15 D) The HQ content was calculated to correspond to 10 mg per mol double bond in all constituents involved. Exemplary pictures of various resins with different amounts of Ni (and therefore different amounts of MMA and a slightly different ratio between PSO and TMPTMA) can be seen in Figure 15. The Ni-content was varied between 3-5%, calculated to the expected Ni content in the pyrolysed specimens.

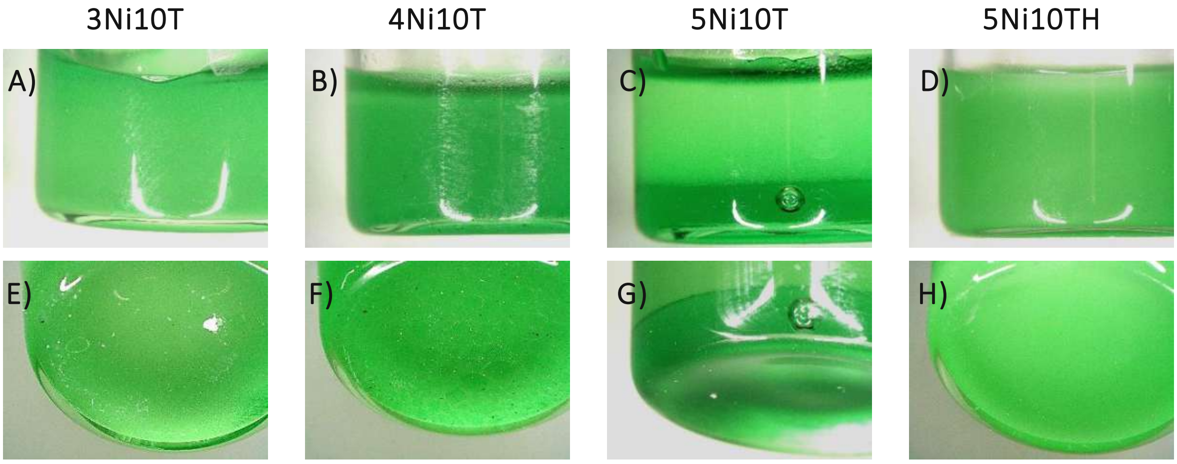

Figure 15: Microscope images of different perspectives of the gelled resins 3Ni10T (A and E), 4Ni10T (B and F), 5Ni10T (C and G) and 5Ni10TH (D and H) after rotary evaporation and without addition of photoinitiator.

The formation of a pronounced layered phase separation rises with an increasing concentration of Ni in the resin. This phenomenon could also be observed when increasing the amount of TMPTMA in the sample. The addition of 10 mg/mol$_{DB}$ HQ supressed the strong layer formation without hindering the spherical micelle formation within the remaining resin.

In addition to the occurring phase separation, a gelation of the Ni-modified resin could be observed. Since this resulted in a smaller timeframe (about 6 h) for the resin to be usable for printing, the gelation was briefly investigated. A beneficial influence due to the addition of HQ could also be observed since it retarded the undesirable gel formation of the resin. The additional HQ resulted in a resin that could be stored over night without layer formation or gelation. Still, printing was always done with freshly prepared resins to achieve the best possible printing results.

The gelation of the resin could not be observed for the reference materials without any nickel. This is due to the catalytic properties of the present Ni, promoting a cationic polymerisation without the addition of photoinitiator or UV-light exposure.

5.1.2 Photoreaction

The photorheological behaviour of selected resins without Ni and with 10 wt% reactive diluent (TMPTMA) and Ni-containing resins with different concentrations of TMPTMA were studied (10 wt%, 15 wt% and 20 wt%).

During resin production, it was observed that although phase separation occurred even without the addition of reactive diluent, it became more pronounced as the amount of TMPTMA increased. In addition, it was observed that the dark green phase that accumulates in the micelles does not polymerise under UV light. This is why 20 wt% were set to be the maximal concentration of TMPTMA, resulting in a printable resin where the phase separation was not yet too strong to negatively affect AM.

Figure 16 shows the results of a photorheology experiment of the 5Ni10T resin, with an additional highlight of the first 12 s after initial light exposure.

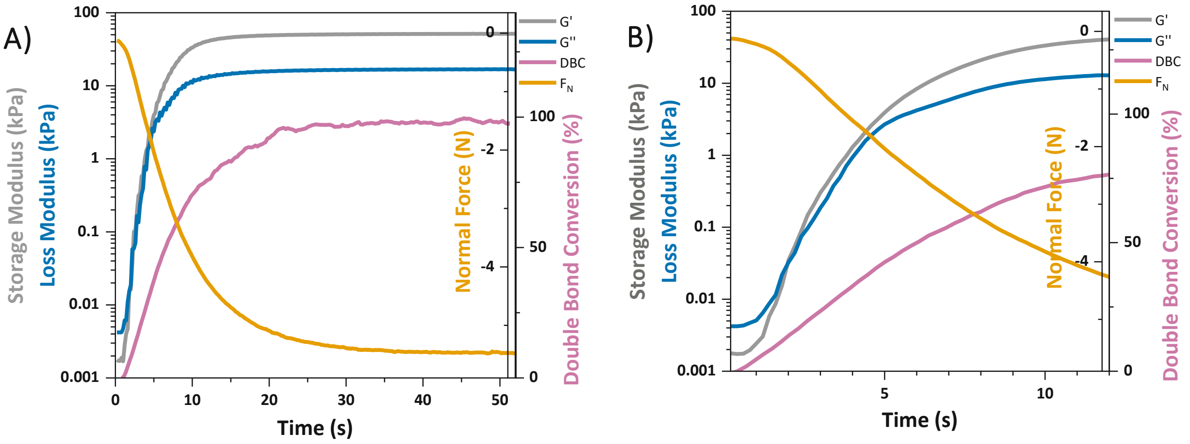

Figure 16: Exemplary RT-NIR-Photorheology study of 5Ni10T, showing the storage modulus G', loss modulus G'', normal force F_N and double bond conversion DBC versus the time after initiation of the radiation exposure. (A) complete measurement. (B) measurement results of the first seconds after initial light exposure of the same measurement.

For the sample shown above (5Ni10T), the gel point, defined as the time where intersection between storage and loss modulus (G', respectively G'') takes place, is reached after only a few seconds. Furthermore, a high final DBC can be seen.

Figure 17 shows the results of the results of DBC, G' and F_N for the samples Ref10T, 5Ni10T, 5Ni15T and 5Ni20T.

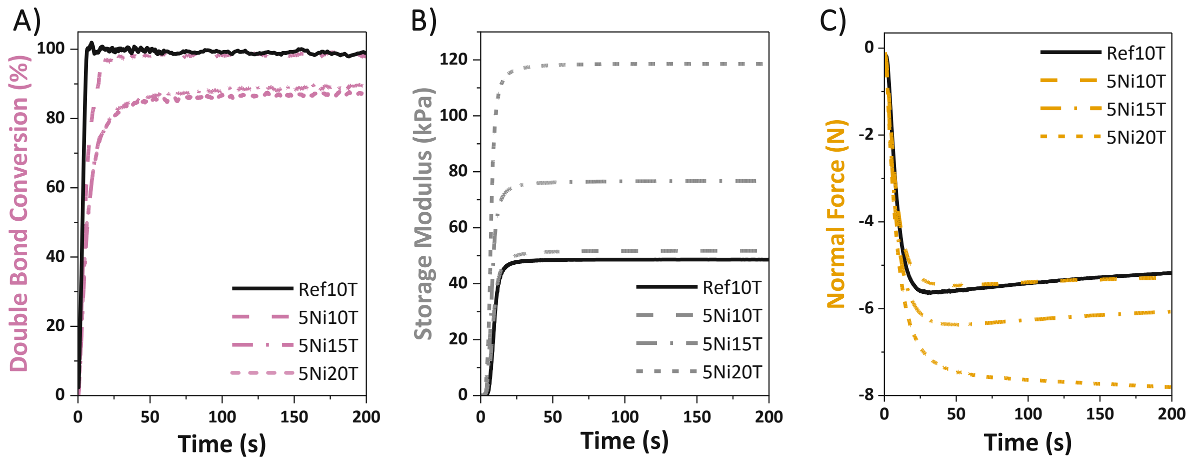

Figure 17: NIR-Photorheology study of the reference material with 10 wt% TMPTMA Ref10T (—) and Ni-modified systems with 10 wt% (-··-), 15 wt% (···) and 20 wt% (---) TMPTMA: (A) double bond conversion DBC; (B) storage modulus G'; (C) normal force F_N

Table 3 summarises the data obtained from NIR/photorheology investigations. The reference was compared with the Ni-modified system and the influence of the amount of reactive diluent (at 10, 15 and 20 wt%) was investigated.

Table 3: NIR-Photorheology results regarding the time to gel point (t_g), double bond conversion at gel point (DBC_g), final double bond conversion (DBC_{final}), maximal storage modulus (G'_{max}) and the shrinkage force (F_N) of the samples Ref10T, 5Ni10T, 5Ni15T and 5Ni20T.

Resin	t_g (s)	DBC_g (%)	DBC_{final} (%)	G'_{max} (kPa)	F_N (N)
Ref10T	3.1 ± 0.2	43 ± 9	100 ± 2	49 ± 28	-5.1 ± 0.9
5Ni10T	2.3 ± 0.1	18 ± 3	99 ± 1	52 ± 22	-5.2 ± 0.9
5Ni15T	2.3 ± 0.1	17 ± 3	89 ± 7	77 ± 2	-6.0 ± 0.4
5Ni20T	2.2 ± 0.3	14 ± 1	88 ± 3	118 ± 8	-7.9 ± 0.2

The gel point is reached faster in the systems modified with Ni than in the Ni-free reference system. The amount of reactive diluent (TMPTMA) has no significant influence on the gel point. The increase in multifunction TMPTMA also leads to faster curing and network formation, resulting in a lower double bond conversion at gel point (DBC_g). This means that the formed subnetwork is sufficient to reach the strength required for the gel point, which is beneficial for a faster printing process. In the reference material, a higher double bond conversion is needed for the material to reach the gel point. Therefore, the gel point is reached at a later time.

The value of the maximum storage modulus (G'_{max}) rises with increasing amount of TMPTMA. This is related to the increasing strength of the cured components and a higher extent of cross-linking.

In addition to that, the gel point corresponds well with the onset of measured normal force, which is an indication of the polymerisation-induced shrinkage and shrinkage stress evolution. In case of the Ni-modified systems with a higher TMPTMA content, the increase in storage modulus is achieved more quickly after the start of radiation exposure. This is most likely due to the formation of subnetworks that are swollen with unpolymerized material. After prolonged exposure, this uncured material potentially also becomes solid and pulls the outer lattice together, resulting in greater shrinkage (F_N), which is a direct consequence of DBC_g. With progressed polymerisation, the resin can no longer move unobstructed, and the already formed subnetworks in converted into a continuous network. Higher DBC and increased G' can result in enhanced shrinkage stress (higher absolute F_N value) with respect to the final stages of photopolymerisation.

Another relevant result from NIR/photorheology experiments is the final double bond conversion (DBC_{final}), which describes the extent of photopolymerisation. With increasing amount of TMPTMA the occurring phase separation was enhanced. However, the resulting inner phase of the micelles was not cured during photopolymerisation and therefore resulted in a lower DBC_{final}.

In addition to the photorheological properties of the resins, the cured layer thickness was also investigated (Figure 18 (A)). For this purpose, exposure tests were carried out in order to determine the curing depth as a function of time. The results for the of the curing depth are shown in Figure 18 (B).

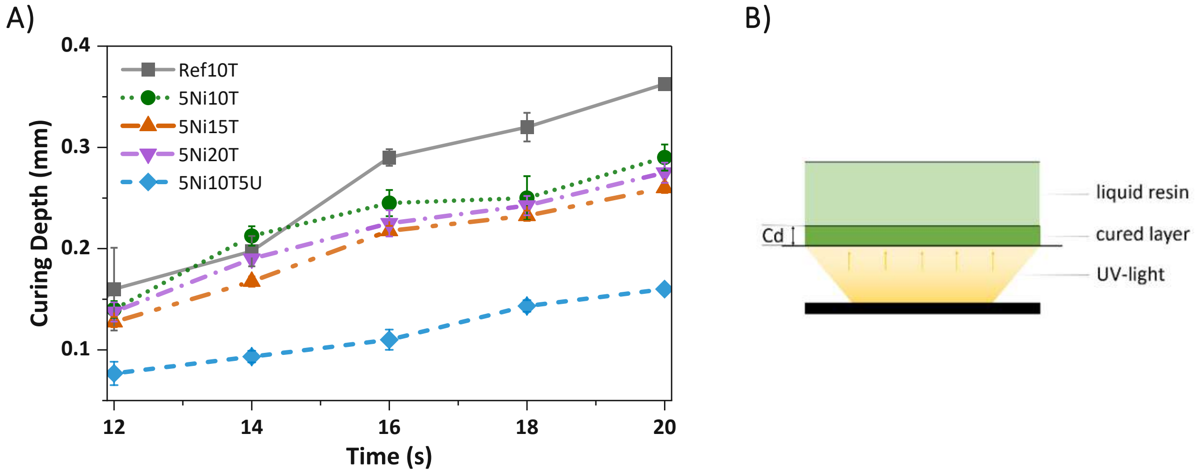

Figure 18: (A) The curing depth Cd as a function of different light exposure times of the reference material with 10 wt% TMPTMA Ref10T (—■—) and Ni-modified systems with 10 wt% (···•···), 15 wt% (-···▲···-) and 20 wt% (-··▼··-) TMPTMA as well as the resin with 10 wt% TMPTMA and 5 wt% UdMA (---◆---). (B) schematic diagram of the curing depth Cd.

The reference Ref10T shows a higher curing depth than the Ni-modified materials. In comparison, the Ni systems (without UdMA) have a smaller time to gel point with a lower DBC. The reference system reacts more slowly, but due to the stronger phase separation, the light in the Ni-containing systems is scattered and attenuated more strongly so that it does not penetrate the resin as deeply. This effect was not observed during photorheological measurements, as a layer thickness of 50 µm was pre-set. In addition, the green colour of the Ni-modified resins may also have affected the required exposure time.

It is particularly noticeable that the amount of added reactive diluent has a comparatively smaller influence on the curing depth, while the addition of UdMA (5Ni10T5U) significantly reduces the curing depth.

The results from the curing depth measurements were then used to adapt the printing parameters for the individual formulations. As a general rule, the selected exposure time should be selected in order to facilitate a layer thickness during exposure tests which is four times the desired layer thickness during latter printing experiments (in this work the desired layer thickness was set on 25 µm). The tests showed that somewhat higher exposure times were required when printing the filigree grid structures in order to achieve good adhesion between the layers and to simultaneously ensure that there was no over-polymerisation. This resulted in an exposure time of 12 s for the reference material grid structures and 18 s for the Ni-modified systems. This correlates to a curing depth of about 0.25 mm (10 times the desired layer thickness). When printing less complex structures such as cylinders and platelets, slightly lower exposure times also led to good printing results.

Among others, platelets, cylinders and grid structures were fabricated. Figure 19 shows exemplary 3D-images of the manufactured components.

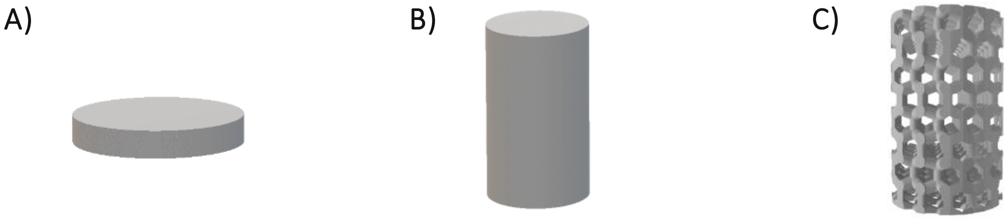

Figure 19: Exemplary 3D-images of different shapes for printing: (A) platelet with a diameter of 10 mm and a height of 2 mm, (B) cylinder with a diameter of 2 mm and a height of 5 mm, (C) grid structure with a diameter of 8 mm and a height of 14 mm.

In this work, all shown components have an adjacent cylinder indicating the direction and plane of observation and distinguish between surfaces and fracture surfaces. In addition, a small arrow indicates the direction of printing.

Figure 20 shows the morphology of printed grid structures in more detail (5Ni10T).

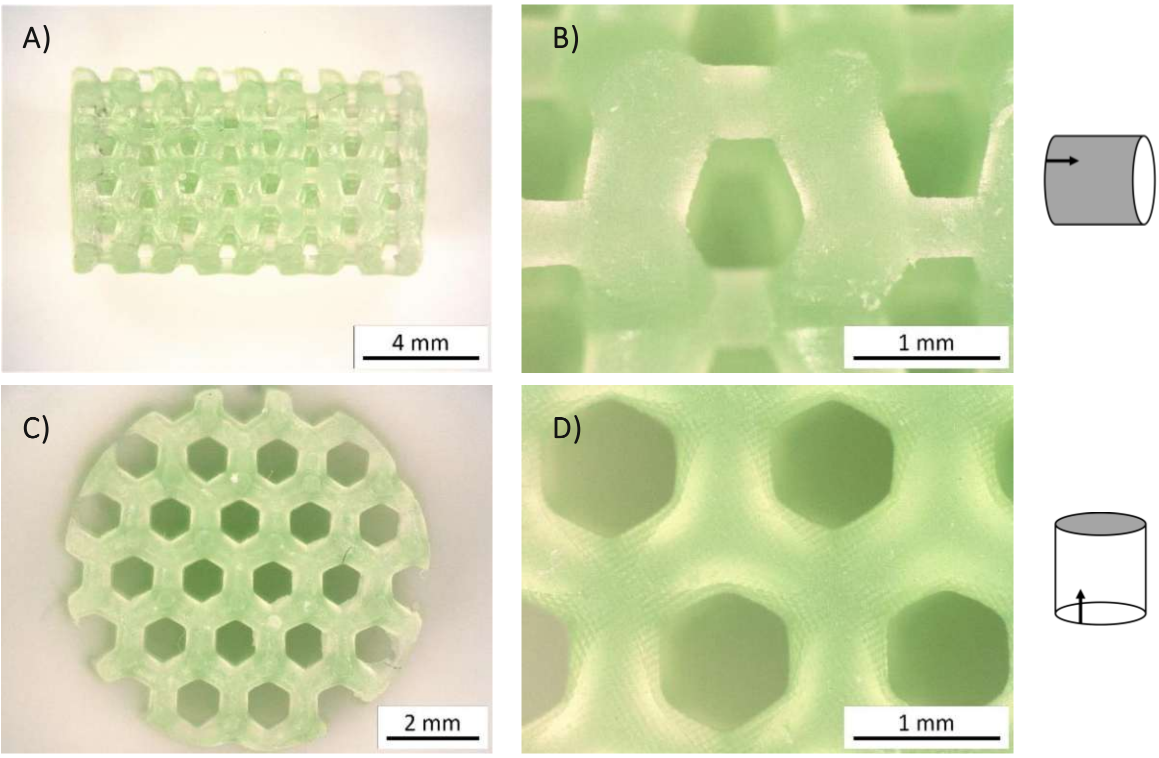

Figure 20: Microscope images of printed grid structures of the resin 5Ni10T: (A) grid structure shown perpendicular to the printing layers; (B and D) grid structure at the same magnification from different perspectives with (B) being the same vertical direction as (A) and (D) showing the smooth last printed horizontal layers.; (C) grid structure shown parallel to the printing layers with the contact points of the removed supports being visible. Adjacent cylinders indicating the direction and plane of observation; arrow indicating the printing direction.

The characteristic turbid green grid structures do not show any cracks after the printing process. Only some of the filigree features at the edge of the structure show defects, as can be seen in Figure 20 A and C. At higher magnifications (Figure 20 B and D), the individual printing layers and printing features are visible. Figure 20 C shows the layers of the lattice structure first printed, recognisable by the contact points of the supports, which had been removed during postprocessing.

Figure 21 shows 3D microscope images of the 3D printed grid structures of the reference material (Ref10T).

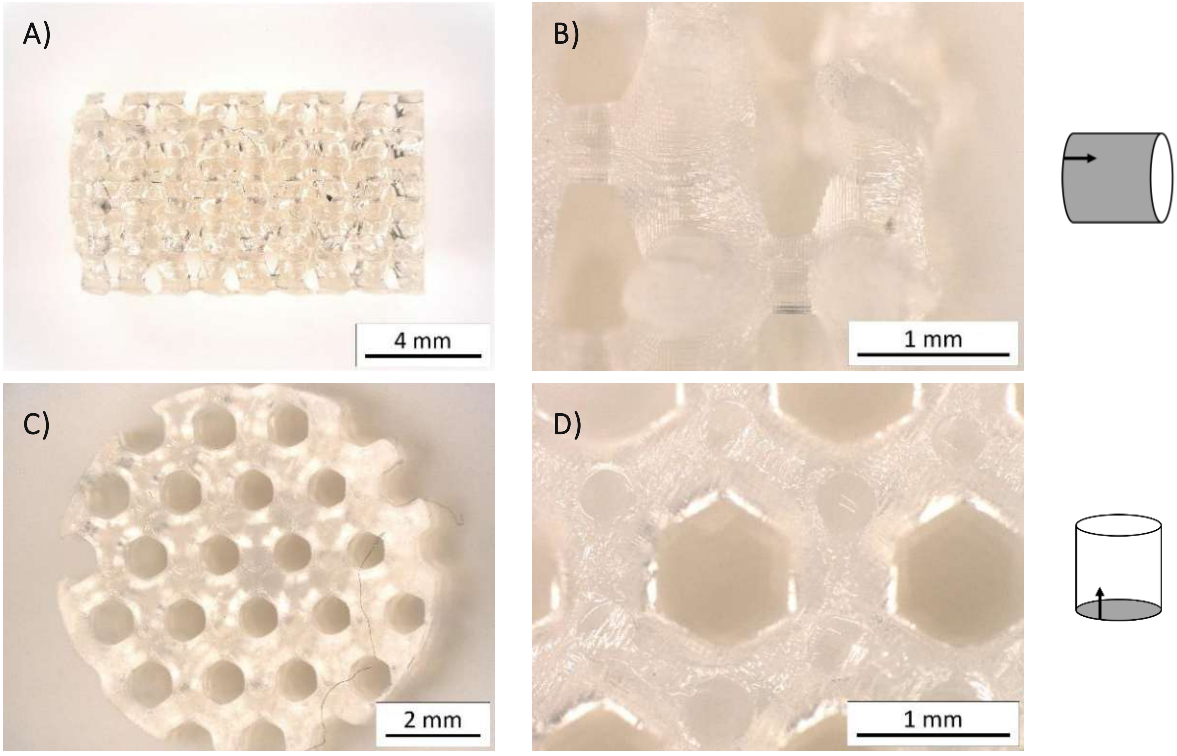

Figure 21: Microscope images of printed grid structures of the resin Ref10T: (A) grid structure shown perpendicular to the printing layers; (B and D) grid structure at the same magnification from different perspectives with (B) being the same vertical direction as (A) and (D) showing the grid structure parallel to the printing layers with the contact points of the removed supports being visible; (C) grid structure shown parallel to the printing layers with the smooth last printed horizontal layers. Adjacent cylinders indicating the direction and plane of observation; arrow indicating the printing direction.

The reference material is not as turbid as the 5Ni10T grid structures. Because of the missing Ni, the reference has a white appearance with a hint of yellow, resulting from the yellow G*16 and BAPO. The shorter exposure time (12 s), necessary to obtain the grid structures resulted in some of the smaller struts having cracks or even detaching from the grid, as can be seen in Figure 21 A and B. Figure 21 D shows the grid structure parallel to the printing layers with the contact points of the removed supports. The individual printing layers are visible in Figure 21 B and D.

Strut sizes down to about 400 µm could be realised with the printer used without any drawbacks. When the diameter of the struts is too small, they are not strong enough to support the structure during the printing process, resulting in fragile and incomplete components. The light exposure time had to be adjusted according to the curing depth, in order to avoid over-polymerisation leading to closing of the grid structure closing of the grid structure.

When comparing printed components from formulations with and without the addition of UdMA, respectively, the printed platelets exhibit a slight variation in colour. Figure 22 shows printed grid structures using either the standard reference material Ref10T or the material including 5 wt% UdMA.

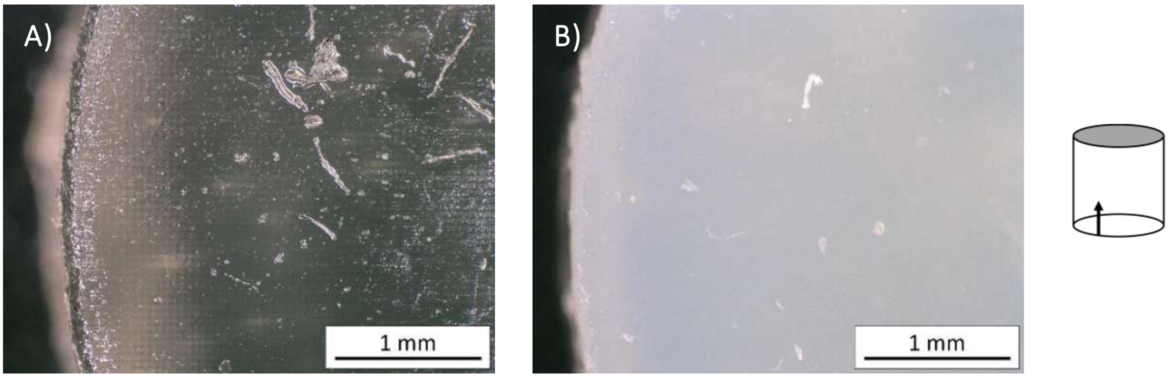

Figure 22: Microscope images of printed platelets shown parallel to the printing layers. (A) Ref10T; (B) Ref10T5U. The addition of 5 wt% of UdMA to the resin results in a green body with higher opacity, indicating an occurring phase separation. Adjacent cylinder indicating the direction and plane of observation; arrow indicating the printing direction.

The addition of UdMA leads to an opaquer cured component, compared to the pieces without UdMA. This may indicate an additional occurring phase separation. This is preferable, since the UdMA is meant to completely volatilize during the pyrolysis, resulting in a porous component. The same opacity could be observed in Ni-containing samples.

5.2 Polymer-to-ceramic conversion

In this section, the thermal conversion of the preceramic polymer into the ceramic, or more precisely ceramer, is described in more detail. In a first step, ATR-FTIR measurements as well as TGA and DTA measurements were carried out. In addition, the linear shrinkage and the ceramic yield of the pyrolyzed components were investigated.

Complementary to ATR-FTIR investigations of the unpyrolysed samples (5.1.1 – Resin characteristics), ATR-FTIR measurements were performed on milled samples after pyrolysis in Ar atmosphere at temperatures of 600, 700 and 800 °C with a dwell time of 2 h. Measurements were conducted with the samples 5Ni10T, 5Ni10T5U, Ref10T and Ref10T5U. The wavenumber range between 1850 and 2400 cm^{-1} was again masked out in all subsequent spectra.

The FTIR spectra as a function of the sample state were compared, as can be seen exemplarily for 5Ni10T in Figure 23. There were no significant differences between the four formulations to be observed.

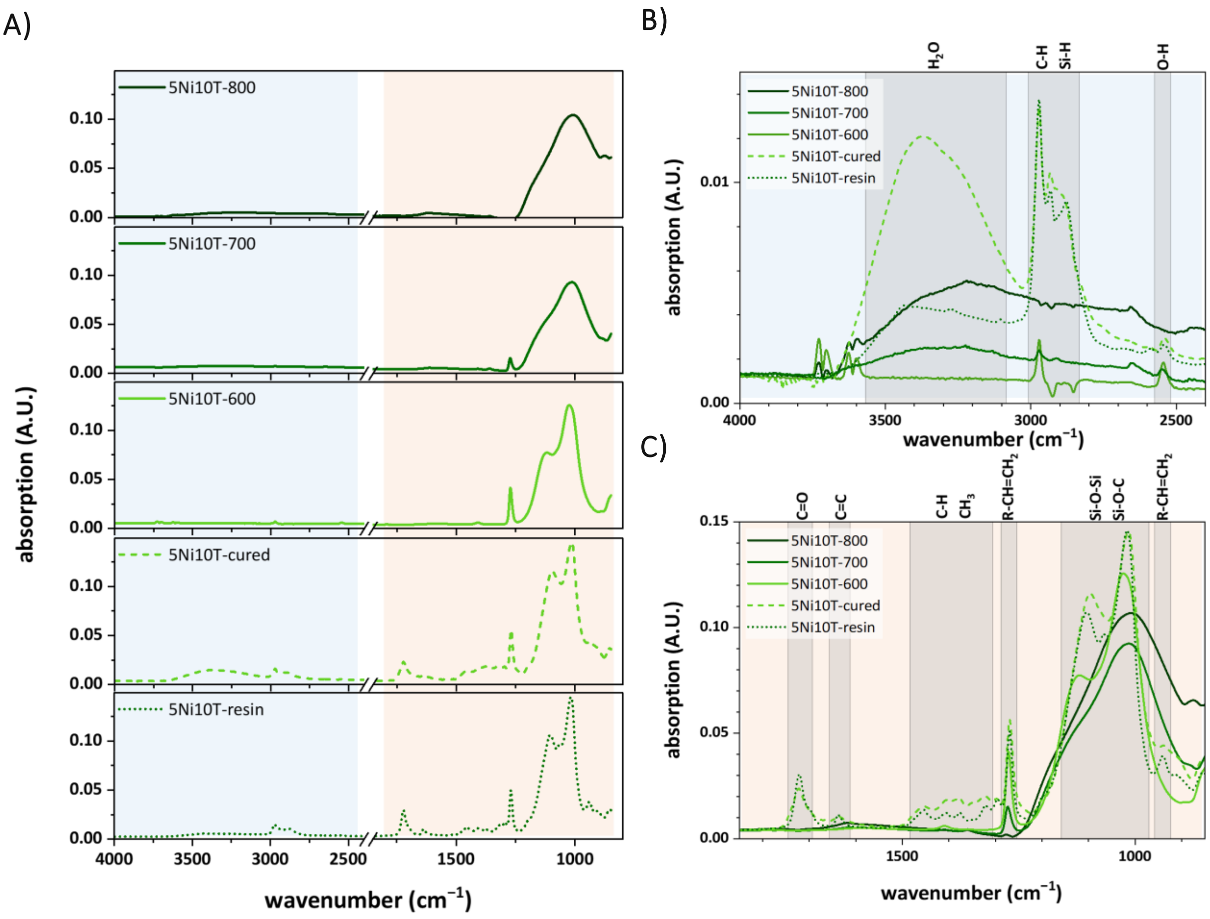

Figure 23: ATR-FTIR spectra of the 5Ni10T formulation. (A) Individual spectra of the resin, the photocured printed component and after pyrolysis in Ar up to temperatures of 600 °C, 700 °C and 800 °C from 4000-850 cm^{-1}. (B) Overlay of all five spectra in the region of 4000-2400 cm^{-1}. (C) Overlay of all five spectra in the region of 1850-850 cm^{-1}.

A distinct difference in the signals between the samples before and after pyrolysis can be observed. The signals of asymmetric CH$_3$ stretching vibrations, Si-H vibrations (both around 2970 cm^{-1}) and C-H stretching vibrations (2925 cm^{-1}) originating from the organic residual groups can be determined in the spectra of the resin and the cured component. These modes fade with an increase in pyrolysis temperature. Other organic residues, which can be recognised as C-H (1390-1450 cm^{-1}), also disappear after pyrolysis. In addition, the broad mode between 3120-3370 cm^{-1} indicative of water is present in the non-pyrolyzed materials, which is due to residual water in solvents and Ni(II)nitrate hexahydrate (NiN), as the hexahydrate leads to a stronger mode in the Ni-modified samples. The pyrolysed samples also show signals of water, which was presumably adsorbed to the different samples to varying degrees during storage. The characteristic water signal is not present in the sample pyrolyzed at 600 °C but rises again with increasing pyrolysis temperatures. Residual C-H and Si-H bonds, still present after pyrolysis at 600 °C, result in a hydrophobic material.

As mentioned previously, the peaks assigned to the C=C bond at 1640 cm^{-1} decrease during curing sample, indicating the polymerisation of TMSPM. The peak at 940 cm^{-1}, originating from the vinyl groups, also widens after curing and vanishes after pyrolysis.

The C=O stretching vibrations at 1720 cm^{-1}, typical of MAA or esters such as TMSPM and TMPTMA, become broader after photocuring due to the change of mobility of the C=O bonds with gradual terminal double bond polymerisation. [25]

The peak at 1270 cm^{-1}, indicating R-CH=CH$_2$ and Si-CH$_3$, decrease with rising pyrolysis temperatures. The modes between 990-1120 cm^{-1} could be assigned to a number of Si-O-Si and Si-O-C stretching vibrations 1120-1170 cm^{-1} (cages structures) and 1030-1060 cm^{-1} (Si–O–Si network). As the pyrolysis temperature increases, these signals become a broad single peak with a shoulder at about 1000 cm^{-1}. With increasing pyrolysis temperature, almost all absorption peaks tend to shift slightly and broaden, which is due to the structural reorganisation leading to an increase in the energy for the vibration of each bond. [21]

The signals between 3600-3800 cm^{-1} are side vibrations of CO$_2$ from the measuring environment, which is why they are not discussed further.

In comparison, Figure 24 shows the ATR-FTIR spectra of the pyrolysed samples of the formulation 5Ni10T5U.

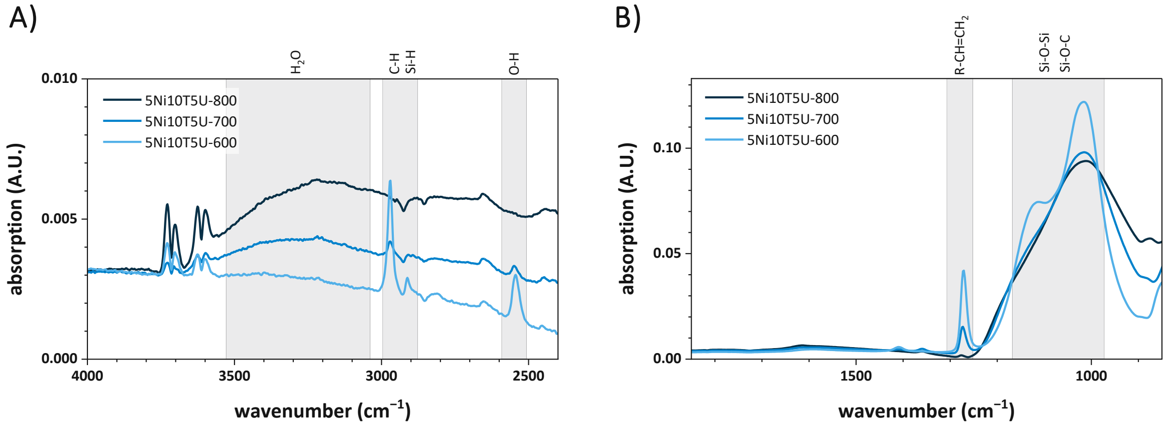

Figure 24: ATR-FTIR spectra of the 5Ni10T5U formulation. (A) Overlay of all three spectra of the printed components after pyrolysis in Ar up to temperatures of 600 °C, 700 °C and 800 °C in the region of 4000-2400 cm^{-1}. (B) Overlay of all three spectra in the region of 1850-850 cm^{-1}.

As explained for sample 5Ni10T, the intensities of the signals associated with organic components decrease with increasing pyrolysis temperature. Higher pyrolysis temperatures also result in a higher signal for the vibrations associated with adsorbed water. In addition, Figure 25 and Figure 26 show the ATR-FTIR spectra of the respective reference materials Ref10T and Ref10T5U.

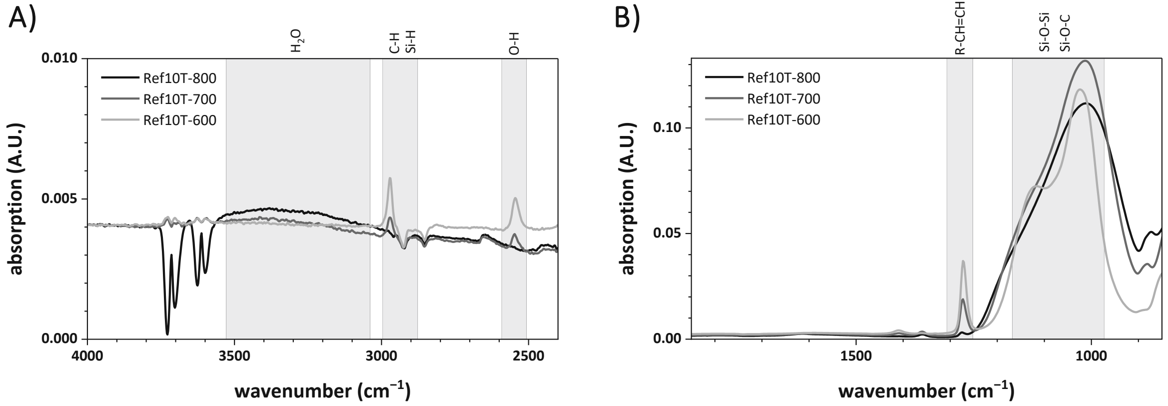

Figure 25: ATR-FTIR spectra of the formulation Ref10T. (A) Overlay of all three spectra of the printed components after pyrolysis in Ar up to temperatures of 600 °C, 700 °C and 800 °C in the region of 4000-2400 cm-1. (B) Overlay of all three spectra in the region of 1850-850 cm^{-1}.

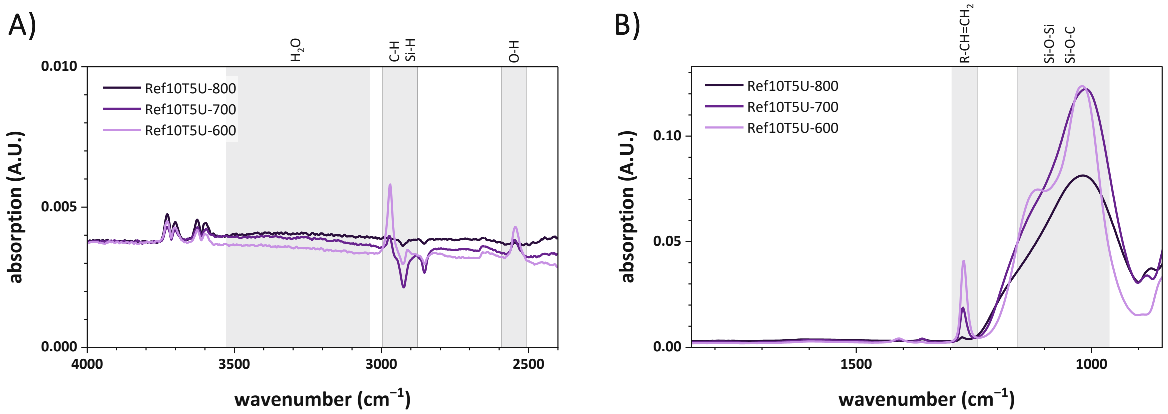

Figure 26: ATR-FTIR spectra of the formulation Ref10T5U. (A) Overlay of all three spectra of the printed components after pyrolysis in Ar up to temperatures of 600 °C, 700 °C and 800 °C in the region of 4000-2400 cm^{-1}. (B) Overlay of all three spectra in the region of 1850-850 cm^{-1}.

When comparing the reference materials with the respective Ni-modified samples, it is noticeable that the signal indicating adsorbed water does not increase as much at higher pyrolysis temperatures. However, the observed hydrophobic behaviour of the samples pyrolysed at 600°C and the decrease in this behaviour with increasing pyrolysis temperature remains. This could be an indicator that the hydrophobic character of the sample is not only related to the pyrolysis temperature but also to the presence of Ni in the sample.

The high thermal stability of polysiloxanes is one of the most important properties of this polymer class and is directly related to the ionic character and the high binding energy of the Si-O bond. Thermal conversion is mainly carried out by splitting and restructuring the organic groups and the various bonds (Si-CH$_3$, Si-H, etc.), resulting in a mixture of volatile compounds and free (hydro) carbon, leading to a loss of weight. [8]

The decomposition behaviour of the cured polysiloxanes and the ceramers as well as the transformation of the preceramic polymer into a PDC was investigated by means of thermogravimetric analysis (TGA) and differential thermal analysis (DTA) in Ar atmosphere at temperatures up to 1500 °C.

Figure 27 compares the results of the TGA and DTA measurements of the cured 5Ni10T and Ref10T samples.

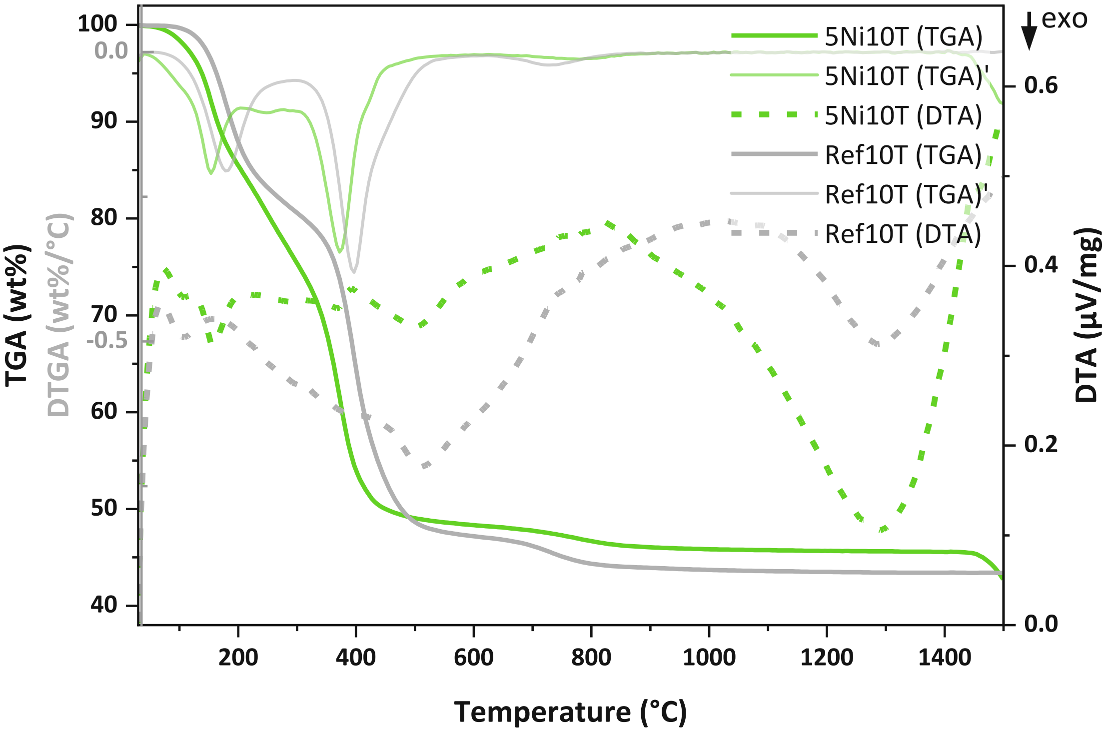

Figure 27: Simultaneous thermal analysis (TGA/DTA) of cured samples 5Ni10T (green) and the according reference material Ref10T (grey) in Ar atmosphere (heating rate 5 K/min). TGA (—), first derivative of TGA (---) and DTA (-··-).

Regarding the TGA curve, the evaporation of the residual water and the remaining solvents can be seen at temperatures below 400 °C. In addition, low-molecular organic compounds, such as alcohols and oligomers, volatilise at relatively low temperatures. Subsequently, the remaining double bonds in the components, which could not already be cured by post-light-exposure, are thermally cured. As soon as the volatile components have evaporated, the conversion and decomposition of the material begins. After the initial weight loss, the decomposition continues with increasing temperature. At higher temperatures (~450-800 °C), decomposition of the organic groups takes place. By breaking Si-H, Si-C and C-H bonds, hydrocarbons such as CH_4, H_2, and other volatile compounds are released. At temperatures above 800 °C, mainly H_2 is released. At about 800 °C, the weight loss levels off, indicating that the polymer-to-ceramic conversion has largely been completed. The first derivative of TGA, which illustrates the temperature dependence of the change, also shows no strong variations above 800°C. The crystallisation of the material can start at temperatures above 1000 °C. Up to this point, the matrix is largely amorphous. Therefore, the thermal stability and the conversion are strongly influenced by the pyrolysis conditions, composition of the resin, and presence of Ni.

When comparing the Ni-modified 5Ni10T sample with the corresponding reference sample Ref10T, it can be seen from the TGA curve that the mass loss is higher for the reference sample (lower ceramic yield), also due to the fact that the 5 wt% Ni remain in the sample after pyrolysis and are responsible for the additional weight. By adding Ni, the decomposition during the pyrolytic conversion is slightly shifted to lower temperatures indicating that Ni catalyses the decomposition and conversion to a certain extent, leaving behind a higher number of inorganic parts remaining in the material. The mass loss at about 1450 °C occurring in the Ni-modified sample could not be assigned. This loss of mass was not detected in any of the individual reactant measurements, suggesting that Ni may also affect the PDC decomposition process.

An exothermic signal at about 160 °C, only occurring in the samples modified with Ni, is an indication of a reaction only taking place in the presence of Ni. Melting of undissolved Ni nitrate, which would result in an endothermic signal at about 180°C, could not be observed. Another explanation for the exothermic signal is thermal cross-linking. The results of the photorheological measurements (5.1.2 – Photoreaction) show that the sample 5Ni10T has a slightly lower double bond conversion than the reference Ref10T, which has a DBC of 100% and therefore no further thermal cross-linking occurs. The exothermic signal at about 500 °C, evident in both samples, indicates that most of the evaporation processes have been completed. Above 500 °C, only small mass losses occur, and polymorphic transformation processes in the material start. At about 1200 °C, crystallisation processes start to take place in the material, which can be seen from the exothermic signal of the DTA curve. The endothermic signal at high temperatures could indicate carbothermic reduction occurring in both the reference and Ni-modified samples.

Based on the available data, it is not possible to determine a distinct baseline of the DTA signal. Therefore, it is also not possible to determine a possible baseline shift that would indicate a glass transition temperature. In order to gain further insights into the temperature-dependent mechanical properties of the cured components, dynamic mechanical thermal analysis (DMTA) measurements would have to be carried out.

The mass loss up to around 300 °C results from the evaporation of water, alcohols and other volatile species. The endothermic and exothermic decomposition between

300 °C and 500 °C corresponds to the severe mass loss in this temperature range. The solvents THF and TPM as well as TMSPM and TMPTMA have a boiling point below 500 °C. NiN, as a hexahydrate, has a mass loss of about 73% at 500 °C and does not decompose any further.

Between 600 °C and 800 °C, the last significant mass loss occurs. It is known from the experimental work that the samples pyrolyzed at 600 °C are very hydrophobic, whereas the samples pyrolyzed at 800 °C do not show such behaviour. This indicates that the remaining CH_4 groups and other hydrophobic groups in the material are decomposed at these temperatures. This behaviour could be observed in all prepared formulations.

The distinctive exothermic signal at 1290 °C indicates the crystallisation without any mass loss in both the sample 5Ni10T and the reference Ref10T.

The mass loss during pyrolysis and the associated linear shrinkage were also determined for structured specimens. Figure 28 shows the ceramic yield after pyrolysis, corresponding to the remaining mass after the polymer-to-ceramic transformation. The linear shrinkage was determined with respect to the dimensional change of the specimen diameter, since the diameter changes less due to the mechanical stress during post-processing. The linear shrinkage was therefore determined in the plane perpendicular to the direction of pressure. These values differ less than 2% from those obtained by measuring the height of the components.

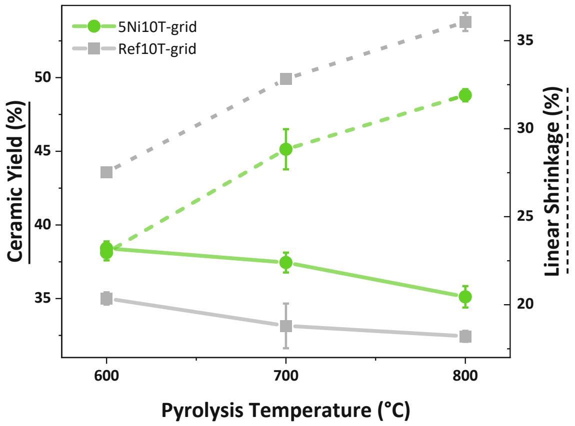

Figure 28: Ceramic yield (—) and linear shrinkage (···) of the printed grid structures from 5Ni10T (•) and Ref10T (■) after pyrolysis at various temperatures.

The grid structures printed using the reference material Ref10T show a lower ceramic yield and a higher linear shrinkage after pyrolysis, meaning that the reference grid structures are smaller and lighter after pyrolysis. The reason for the increased ceramic yield of Ni-modified grid structures can be explained by Ni remaining in the structure.

Figure 29 shows the comparison of the ceramic yield and linear shrinkage of the 5Ni10T-cylinders, compared with the reference material Ref10T and the Ni-modified resin with the addition of 5 wt% UdMA 5Ni10T5U.

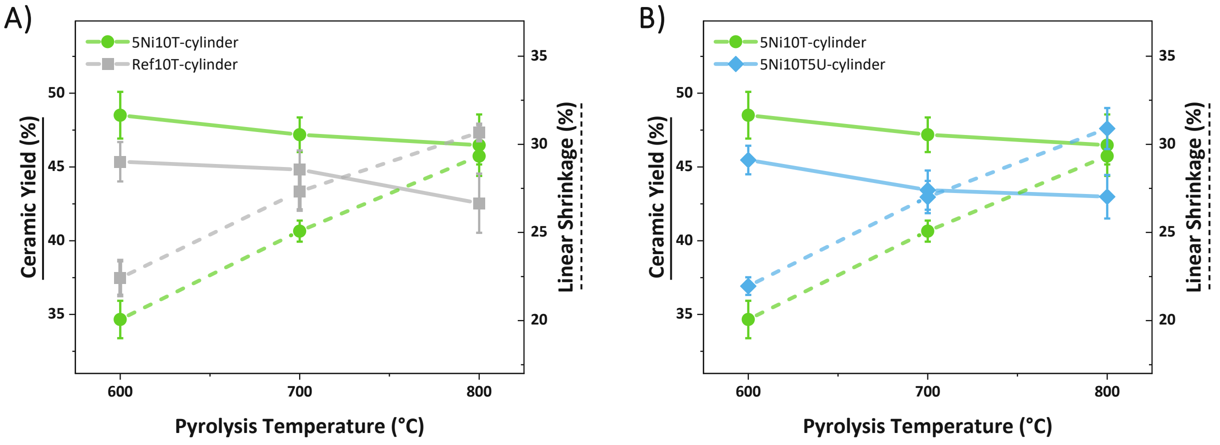

Figure 29: Ceramic yield (—) and linear shrinkage (···) of the printed cylinders after pyrolysis at various temperatures. (A) 5Ni10T (•) and Ref10T (■); (B) 5Ni10T (•) and 5Ni10T5U (◆).

The cylinders made of Ni-free reference material show a lower ceramic yield, which is due to the absence of Ni in the Ref10T sample. When comparing the ceramic yield and linear shrinkage of the 5Ni10T formulation and the Ref10T reference material, a difference between the grids and the cylinders can be observed. The 5Ni10T-cylinders show a higher ceramic yield and a slightly lower linear shrinkage than the corresponding grid structures. Since all other parameters were kept constant, this is due to the different geometry. At 2 mm, the wall thickness of the cylinders is about four times higher than the diameter of struts within the printed grid components. Similar to the grid structures, cylinders built from the reference material system also show a lower ceramic yield and a higher linear shrinkage.

When comparing cylinders made of 5Ni10T and 5Ni10T5U, differences in ceramic yield and linear shrinkage are visible. Despite the presence of 5 wt% Ni, the addition of 5 wt% UdMA results in a lower ceramic yield and a higher linear shrinkage. UdMA is supposed to volatilise during pyrolysis, which explains the lower ceramic yield after pyrolysis. The addition of UdMA therefore, again, leads to slightly smaller and lighter components than their 5Ni10T counterparts.

5.3 Ceramic characteristics

Some of the ceramic properties, such as morphology or crystallinity, are now discussed on the basis of the results obtained with a microscope and SEM imaging. In addition, the distribution and concentration of in-situ generated Ni particles are evaluated by means of SEM and TEM imaging.

The focus in the following section was set on 5Ni10T specimens. Where feasible, said specimens were compared with other samples.

5.3.1 Morphology of pyrolysed specimens

In the following, heating rates during the pyrolysis are indicated with an *R* for the program including additional dwell times at 200 °C (2 h, heating rate 0,5 K/min) and 500 °C (1 h, heating rate 1 K/min) with a final dwell time at the highest temperature (2 h, heating rate 1 K/min). The abbreviation *1K* denotes the samples for which no additional dwell times were added and the furnace was heated to the final temperature at 1 K/min (2 h dwell time).

Influence of pyrolysis temperature

First, the influence of different pyrolysis temperatures, regarding the morphology of different samples is discussed, taking system 5Ni10T as an example. Figure 30 shows exemplary microscope images of 5Ni10T-R grid components pyrolyzed at different temperatures.

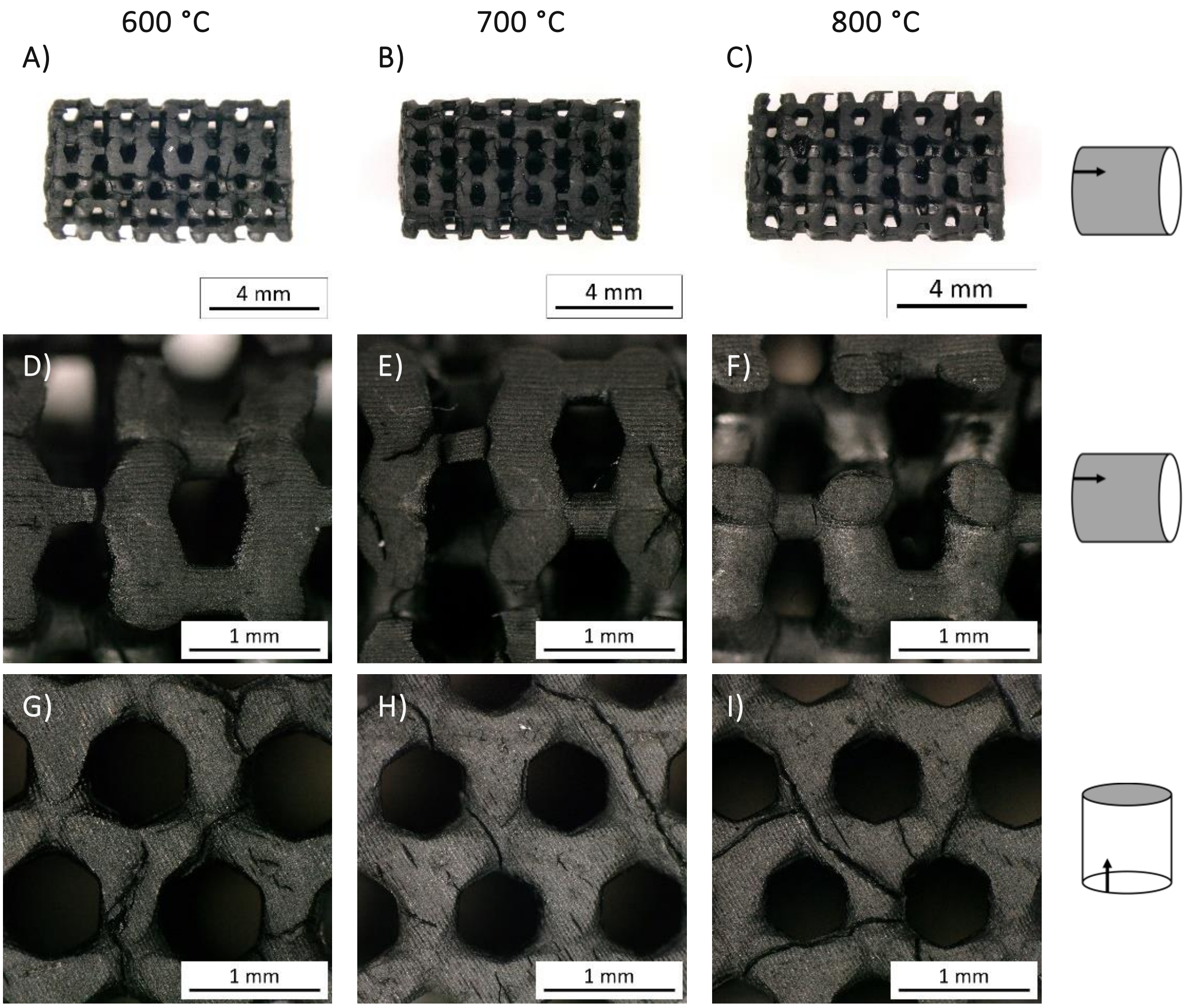

Figure 30: Microscope images of 5Ni10T-R grid structures after pyrolysis in Ar atmosphere at different temperatures (600, 700 and 800 °C). (A-F) grid structures shown perpendicular to the printing layers; (G-I) grid structures shown parallel to the printing layers. Adjacent cylinders indicating the direction and plane of observation; arrow indicating the printing direction.

Given the morphology of the printed and pyrolyzed lattice structures, cracks occurred during pyrolysis, even at low heating rates. The surface has a matte appearance with the individual printing features being visible at higher magnifications. Regarding the crack formation, only small differences between the different pyrolysis temperatures are visible. With increasing pyrolysis temperature, the crack formation is only slightly increased, correlating with the higher linear shrinkage at higher pyrolysis temperatures.

For higher magnifications, the pyrolyzed components were examined by scanning electron microscopy (SEM). Exemplary images of the surfaces of the 5Ni10T samples for all three pyrolysis temperatures are shown in Figure 31.

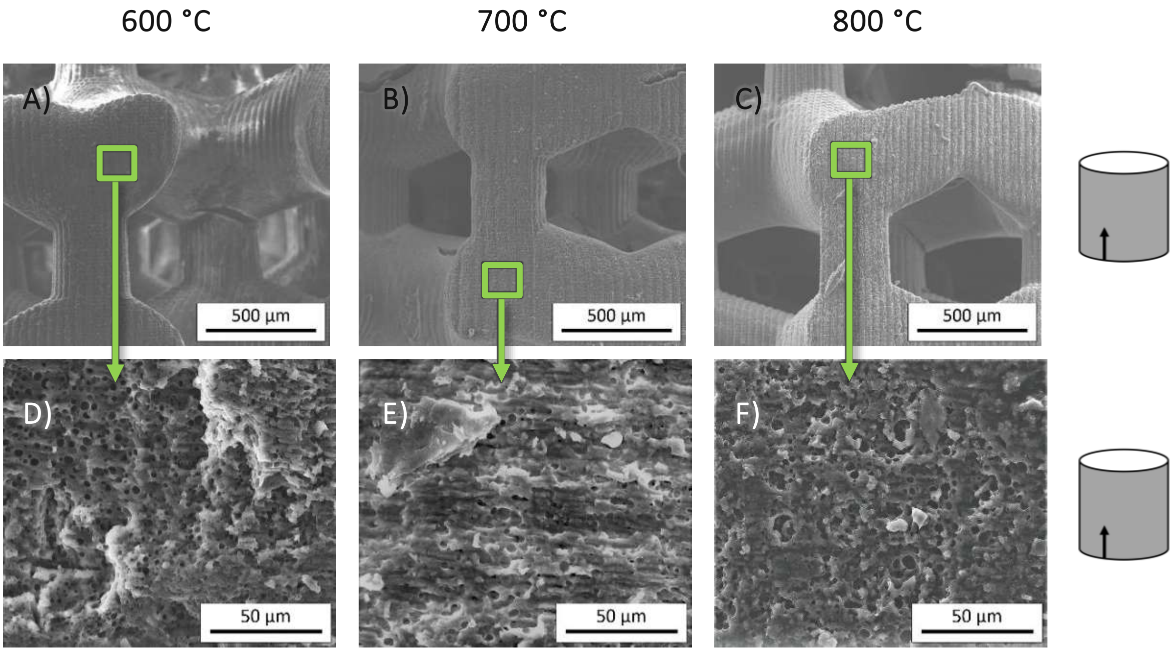

Figure 31: Secondary electron SEM micrographs of 5Ni10T sample surfaces pyrolyzed in Ar atmosphere up to temperatures of 600 °C, 700 °C and 800 °C. (A-C) showing the structure with the individual features due to the resolution of the screen being visible. (D-F) showing the rough surface of the grid structure. Adjacent cylinders indicating the direction and plane of observation; arrow indicating the printing direction.

No clear effect of pyrolysis temperature on surface texture can be seen in the SEM images. The rough surface with some clearly visible pores is comparable at all three pyrolysis temperatures.

The lines visible in the direction of printing (as indicated by the adjacent arrow) are features caused by the screen during the printing process. The pixel resolution of the printer used is not sufficient to avoid these features.

Influence of temperature profile

To observe the influence of the temperature profile, some samples were also heated directly to the final temperature at a rate of 1 K/min. Thus, cylinders of the formulation 5Ni10T were compared at the same pyrolysis temperatures but with different heating rates. First, examples of 5Ni10T cylinders pyrolysed under the same conditions as the lattice structures mentioned in the previous chapter are shown in Figure 32.

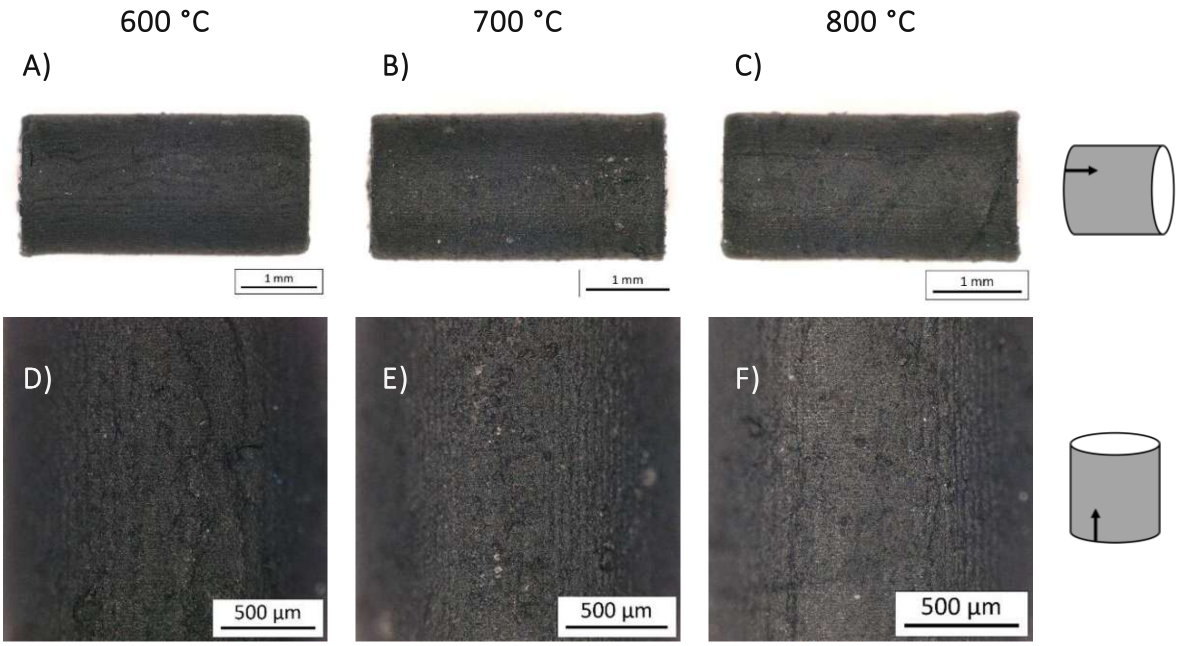

Figure 32: Microscope images of 5Ni10T-R sample surfaces pyrolyzed in Ar atmosphere up to temperatures of 600 °C, 700 °C and 800 °C. (A-C) showing the whole cylinders shown perpendicular to the printing layers. (D-F) showing the cracked surface of the grid structure. Adjacent cylinders indicating the direction and plane of observation; arrow indicating the printing direction.

In contrast to the grid structures shown in Figure 30, the cylinders shown have no cracks. Regarding the surface morphology, there is no difference in relation to the varying pyrolysis temperatures. Complementary to the above, Figure 33 shows the 5Ni10T cylinders that were heated at a rate of 1 K/min during pyrolysis.

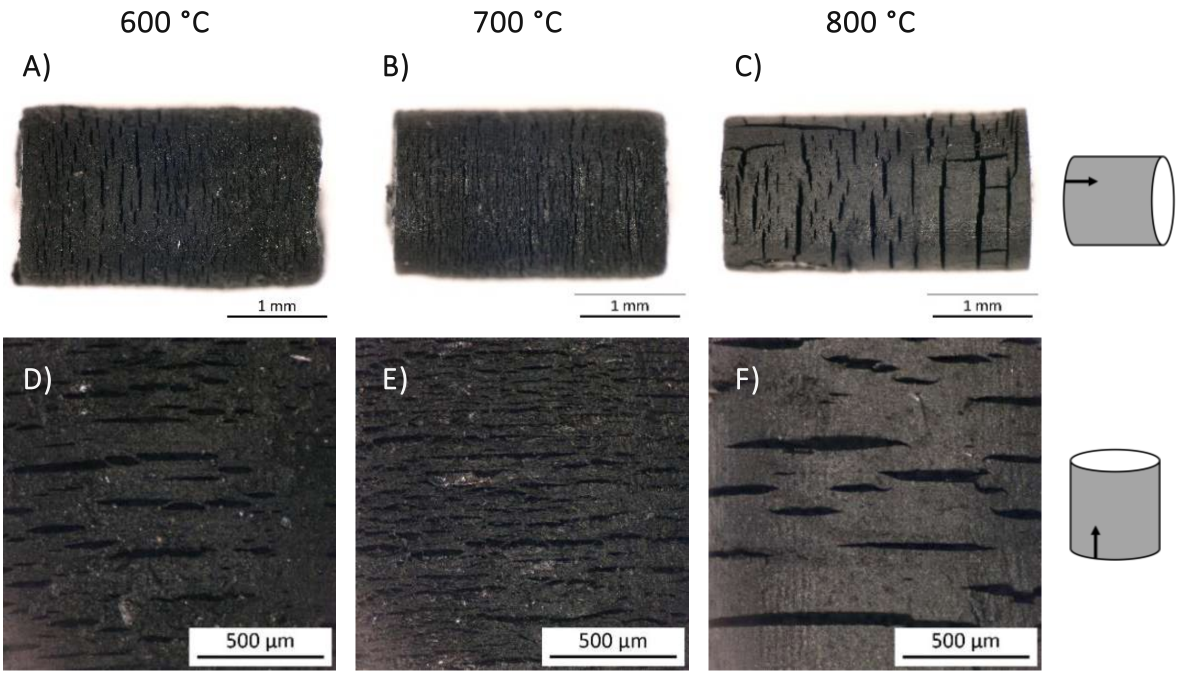

Figure 33: Microscope images of 5Ni10T-1K sample surfaces pyrolyzed in Ar atmosphere up to temperatures of 600 °C, 700 °C and 800 °C. (A-C) showing the whole cylinders shown perpendicular to the printing layers. (D-F) showing the cracked surface of the grid structure. Adjacent cylinders indicating the direction and plane of observation; arrow indicating the printing direction.

Direct heating to the target temperature with 1 K/min results in a large number of small cracks in the specimens at 600 °C and 700 °C and severe cracking at 800 °C. This correlation was not observed in the pyrolysis of the grid structures, suggesting that cracking is strongly dependent on component thickness.

Prevention of dense layer formation

Since not only the surfaces are relevant but also the bulk material was to be examined, micrographs were prepared (Figure 34) by embedding the components in a clear epoxy resin and subsequential grinding and polishing. For both the micrographs and the fracture surfaces, it should be noted that all specimens do not have straight edges and therefore the angle has a very large influence on the optical appearance.

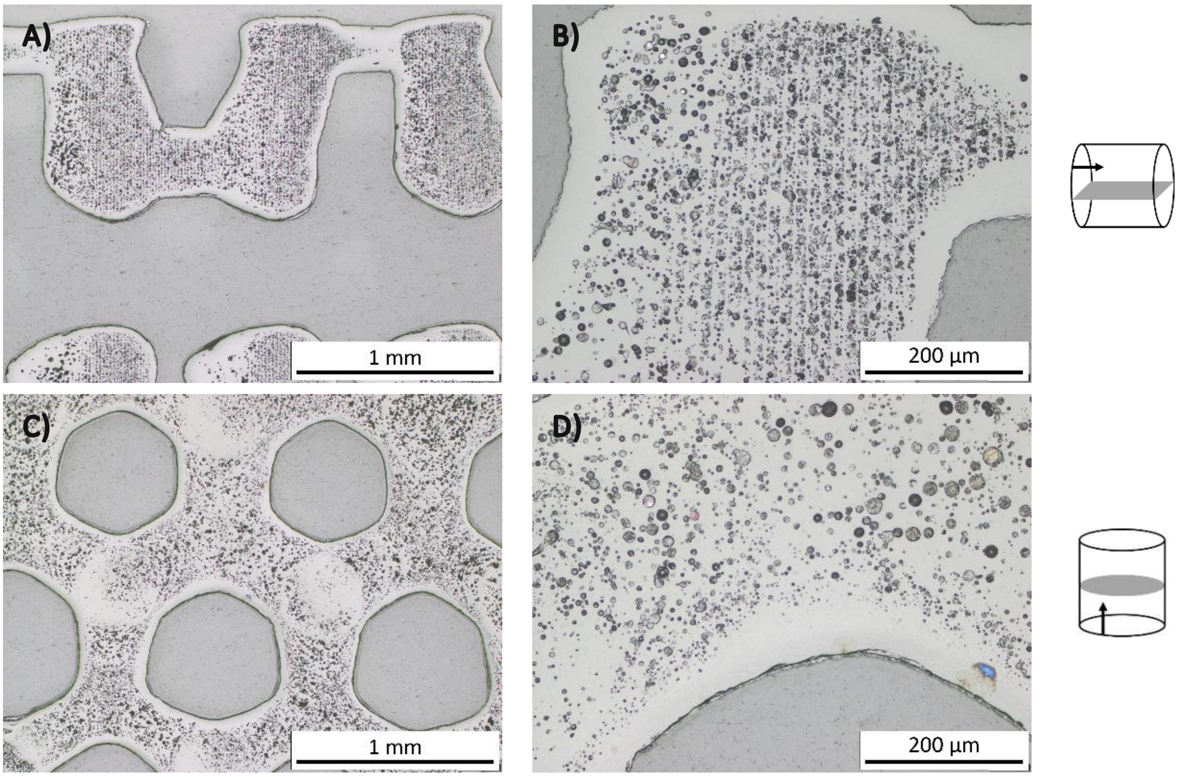

Figure 34: Light-microscope images of micrographs from 3D printed 5Ni10T grids, embedded in epoxy resin. (A/B) grid structure perpendicular to the printing layers; (C/D) grid structure parallel to the printing layers. Adjacent cylinders indicating the direction and plane of observation; arrow indicating the printing direction.

The already mentioned micelles have turned into pores during the pyrolysis and are still clearly visible and well distributed. At the surface of the pyrolyzed grid structures, a dense surface layer is visible, containing an increased concentration of Ni (as later shown by EDX investigations, see section 5.3.2 – Distribution of Ni in ceramic matrix and phase composition). Since the formation of a dense surface layer negatively affects the specific surface area of the components and therefore the catalytic activity, it was desirable to inhibit the formation of said layer.

The first approach to suppressing the dense surface layer formation was a change in atmosphere within the furnace during pyrolysis. Besides the regular Ar atmosphere, dried Ar was used, using a molecular sieve and Cu chips as oxygen getter. In addition, a reductive atmosphere with 5% H_2 in Ar was evaluated, regarding its influence on the surface layer. Due to the samples available at the time of the experiment, the variation of the furnace atmosphere during pyrolysis was carried out using samples of the composition 5Ni20T. In order to compare the effect of the three distinct atmospheres and to be able to exclude other influences, the fracture surface of 5Ni20T-600-1K from the exact same print job is shown in Figure 35.

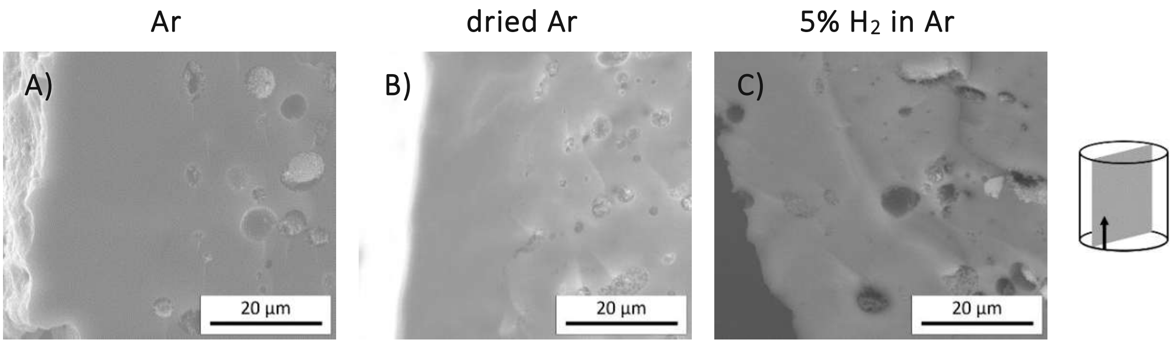

Figure 35: Secondary electron SEM images of 5Ni20T-600-1K sample fracture surfaces, pyrolyzed in different atmospheres up to temperatures of 600 °C. (A) Ar; (B) purified Ar (molecular sieve and Cu as oxygen getter), (C) 5% H_2 in Ar. Adjacent cylinder indicating the direction and plane of observation; arrow indicating the printing direction.

The dense surface is visible in all three different variants, still covering the existing inner pores. The samples shown in Figure 35 C have isolated pores that are slightly closer to the sample surface, but the dense layer is still present. In case 5Ni10T-600-1K samples, a difference in morphology is evident after pyrolysis in Ar or in 5% H2/Ar, as can be seen in Figure 36.

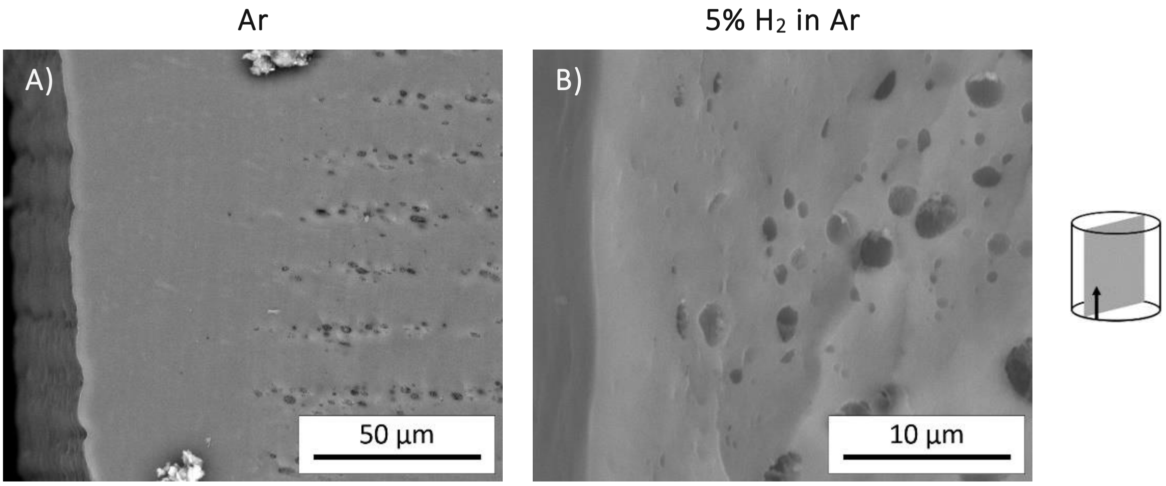

Figure 36: Secondary electron SEM images of 5Ni10T-600-1K sample fracture surfaces, pyrolyzed in different atmospheres up to temperatures of 600 °C. (A) Ar atmosphere and (B) 5% H_2 in Ar, the latter image showing a higher magnification. Adjacent cylinder indicating the direction and plane of observation; arrow indicating the printing direction.

In spite of stemming from the same print job, the difference in the two samples is clearly visible. Even at a significantly higher magnification of the sample pyrolysed with 5% H_2 in Ar, the dense layer is difficult to see. The Thickness of the dense surface layer was significantly reduced under the influence of a slightly reducing pyrolysis atmosphere. However, the dense layer is still present and thus makes the existing internal porosity inaccessible. In addition, the direction of the fracture has a significant influence, making it difficult to determine the exact layer thickness.

As an alternative approach to eliminate the dense layer, UdMA was used as an additive. The added UdMA is meant to volatilize during pyrolysis and connect the existing internal porosity and thus significantly increase the specific surface area. Fracture surfaces of the sample 5Ni10T5U-600-1K-Ar, pyrolyzed in Ar atmosphere at 600 °C with a heating rate of 1 K/min, are depicted in Figure 37.

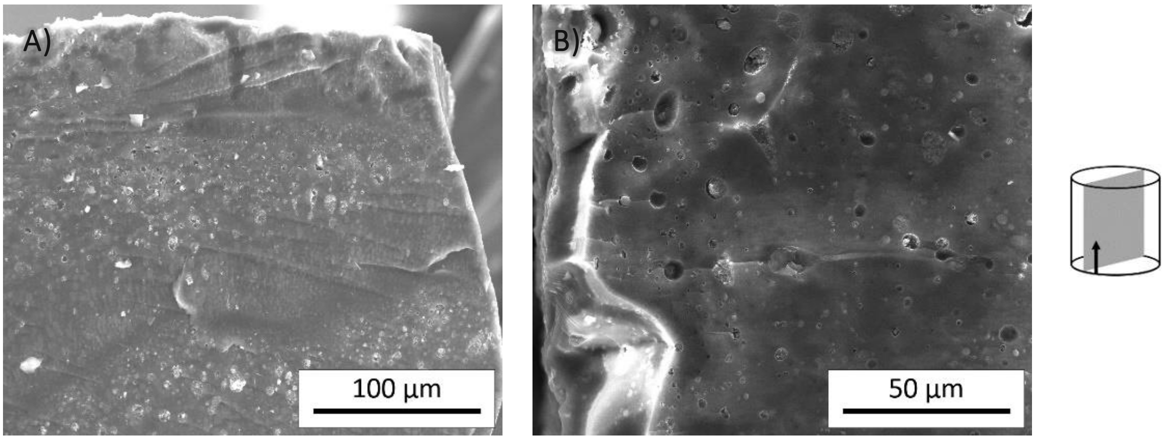

Figure 37: Secondary electron SEM images of 5Ni10T5U-600-1K-Ar fracture surfaces. (A) revealing different layers of dense layers and areas with pores, due to the phase separation; (B) higher magnification of the fracture at the surface area, showing the uneven surface with the pores not being compacted in the outer areas. Adjacent cylinder indicating the direction and plane of observation; arrow indicating the printing direction.

The addition of 5 wt% UdMA to the existing resin largely prevents the formation of a dense outer layer, as can be seen in Figure 37 B. The extent to which this affects the specific surface area will be described in more detail in 5.3.3 – Specific surface area. In Figure 37 A, the pore-rich layers and the denser interfaces between the individual 3D printed layers are visible.

Comparison to reference material

Supplementary to the 5Ni10T material shown in Figure 30, the reference grid components were also pyrolyzed at different temperatures, as shown in Figure 38.

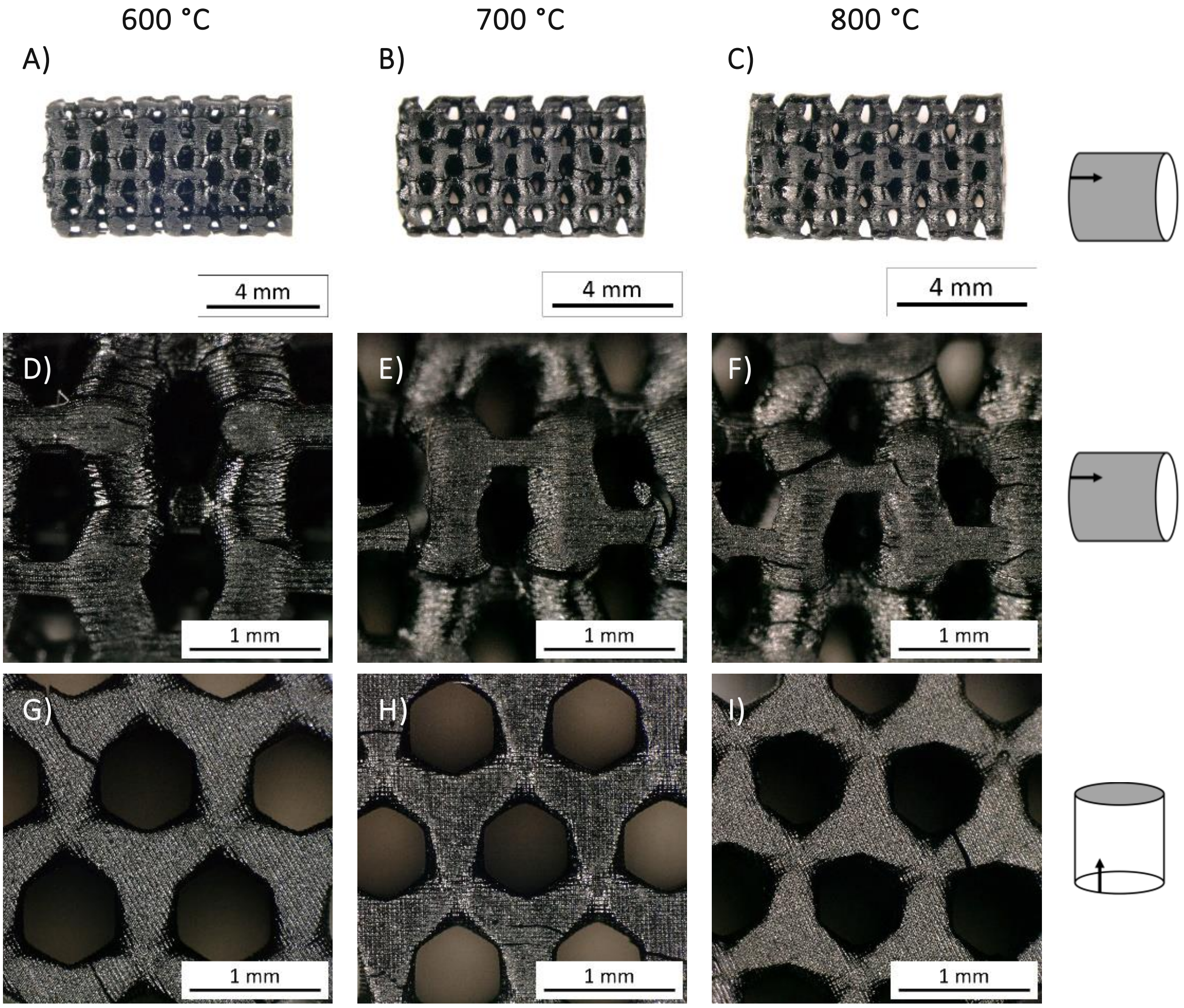

Figure 38: Microscope images of Ref10T-R grid structures after pyrolysis in Ar atmosphere at different temperatures (600, 700 and 800 °C). (A-F) grid structures shown perpendicular to the printing layers; (G-I) grid structures shown parallel to the printing layers. Adjacent cylinders indicating the direction and plane of observation; arrow indicating the printing direction.

The shiny surfaces of the Ref10T grid structures also show the individual printing features. Similar to the 5Ni10T components, the structures also show various cracks, most of them at nodal points and oriented in parallel to the printing direction (perpendicular to the individual printing layers).

A further comparison was made between the manufactured 5Ni10T cylinders and the corresponding reference Ref10T, as well as the 5Ni10T5U sample. When comparing the different formulations after pyrolysis at 600 °C (with the additional dwell times), strong differences occur, as can be seen in Figure 39.

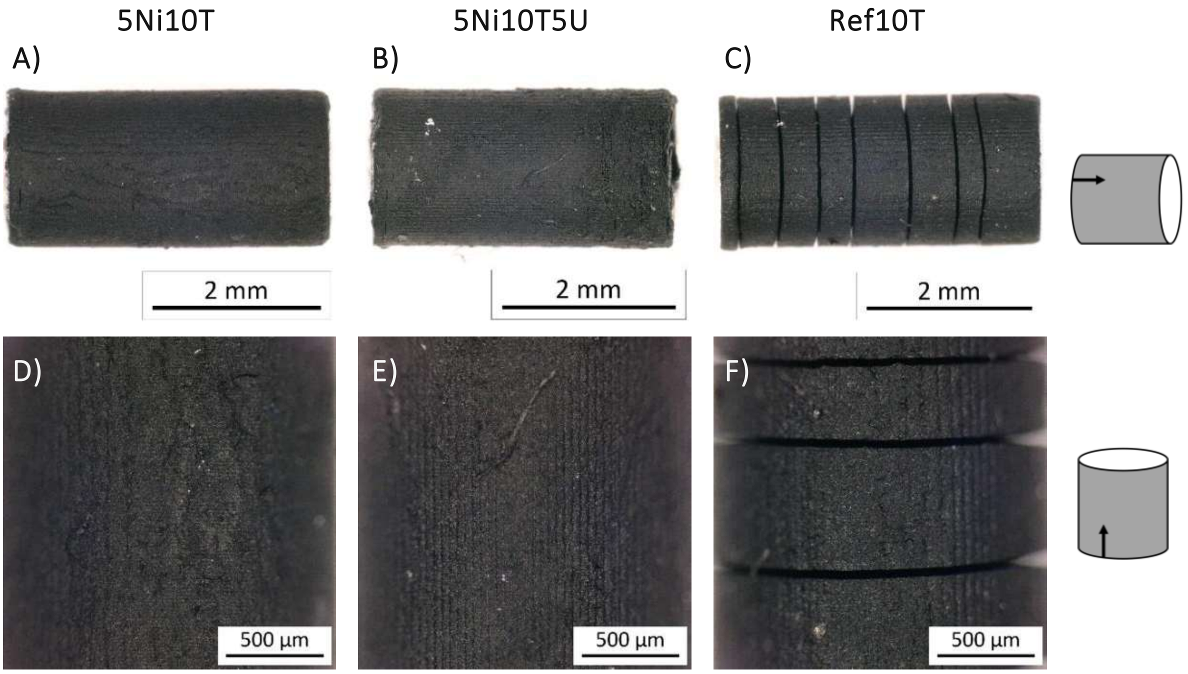

Figure 39: Microscope images of cylinders of different formulations (Ref10T, 5Ni10T and 5Ni10T5U) after pyrolysis at 600 °C. (A-F) cylinders shown perpendicular to the printing layers. Adjacent cylinders indicating the direction and plane of observation; arrow indicating the printing direction.

The reference sample Ref10T-600-R shows very pronounced crack formation along the plane perpendicular to the printing direction, presumably between the individual printing layers. The other two Ni-modified samples 5Ni10T-600-R and 5Ni10T5U-600-R show no surface cracks. The addition of UDMA therefore does not change the cracking tendency of the samples.

Further examination of the Ni-free reference material Ref10T (Figure 40) reveals a smooth surface and a completely dense and homogeneous bulk material. Due to this homogeneity, the reference material will not be discussed more closely in the following section.

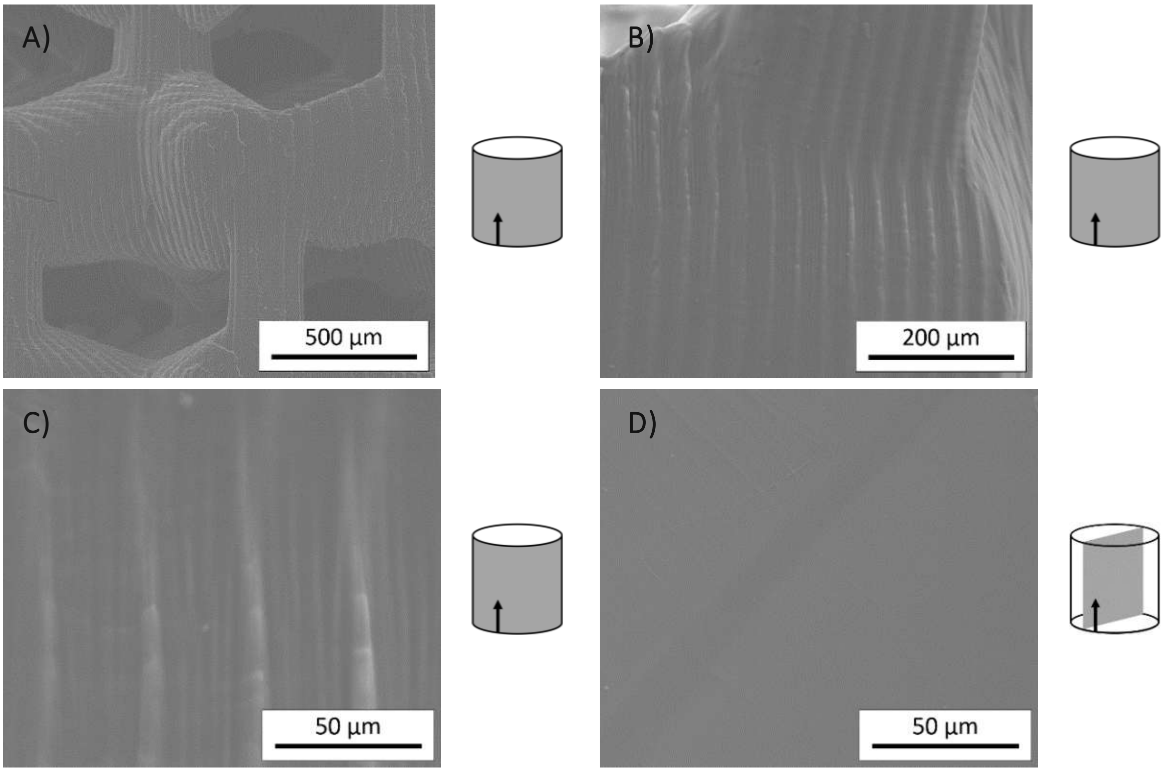

Figure 40: Secondary electron SEM micrographs of Ref10T samples pyrolyzed in Ar atmosphere. (A, B, C) surface shown perpendicular to the printing direction at different magnifications; (D) fracture surface. Adjacent cylinders indicating the direction and plane of observation; arrow indicating the printing direction.

Specimens externally manufactured by LCM

One print job was done at Lithoz GmbH with the formulation 5Ni10T5UH, since this has proven to be the most stable formulation regarding the phase separation and the available timeframe before gelation hinders the printing. The 3D printers available at Lithoz GmbH are suitable for higher intensities during the UV-exposure, leading to a shorter exposure time. In addition, the integrated scraper blades used after each printed layer further influence the printing process and the resulting components. The printed cylinders were then pyrolyzed under Ar atmosphere at temperatures up to 600 °C and 800 °C, including all dwell times (at 200 °C and 500 °C) to minimize crack formation. Figure 41 shows SEM images of the pyrolyzed cylinders surface areas.

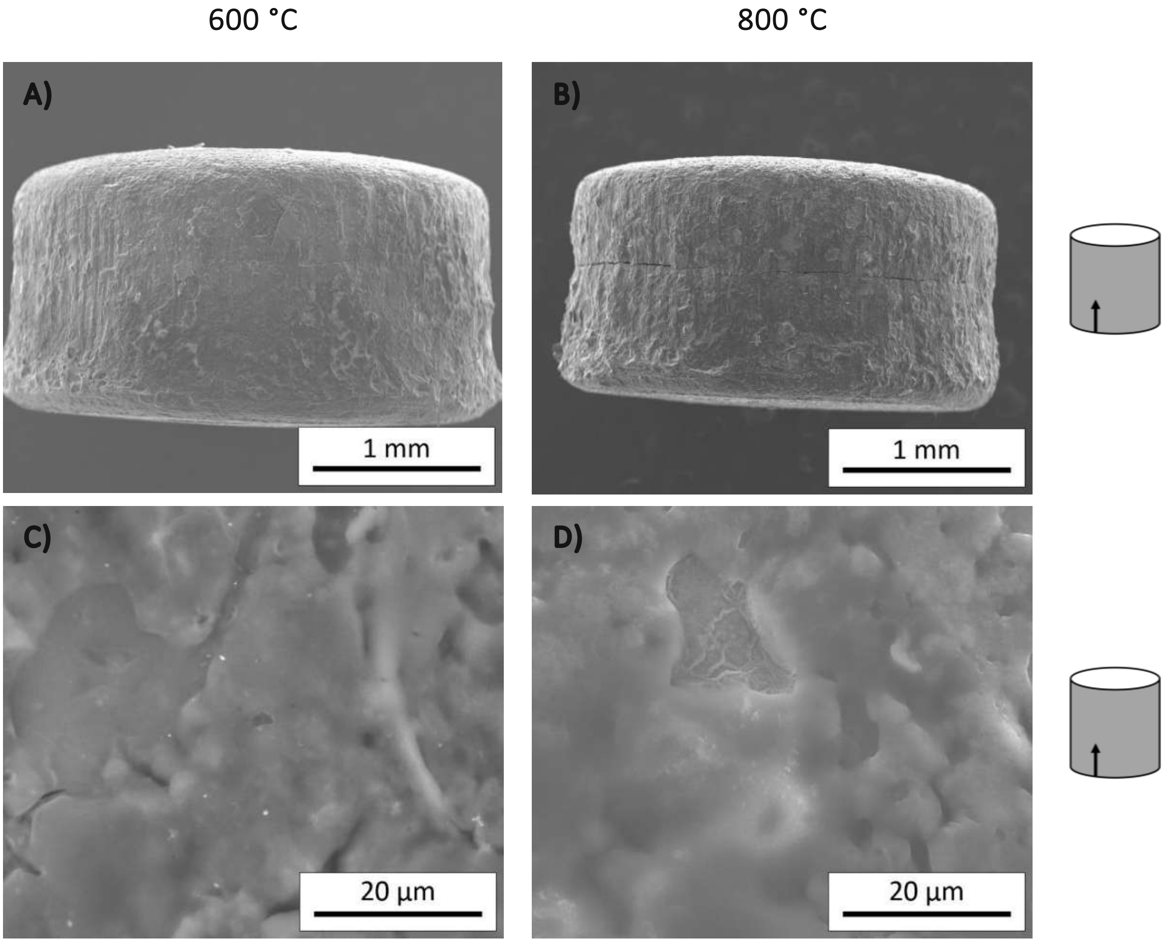

Figure 41: Secondary electron SEM images of surface areas of 5Ni10T5UH cylinders printed at Lithoz GmbH. (A/C) pyrolyzed at 600 °C; (B/D) pyrolyzed at 800 °C; (A/B) showing the whole cylinders and (C/D) the surface area perpendicular to the printing layers. Adjacent cylinders indicating the direction and plane of observation; arrow indicating the printing direction.

In accordance with the previously discussed cylinders, the component pyrolyzed at 800 °C has a higher linear shrinkage. Except for a single crack (shown in Figure 41 B) located in the center of the sample with an orientation parallel to the printing layers, no crack formation could be observed, similar to the previous experiments (Figure 39 C and F).

The surface of the cylinders printed at Lithoz GmbH do not show the same morphology as the previous cylinders printed at the desktop printer. The samples have a smoother surface and do not show the expected surface with a porous appearance. Since post processing, including cleaning and post-curing, was also done at Lithoz GmbH, this may have influenced the surface properties. Figure 42 shows backscatter electron SEM images of the fracture surfaces of the samples printed at Lithoz GmbH.

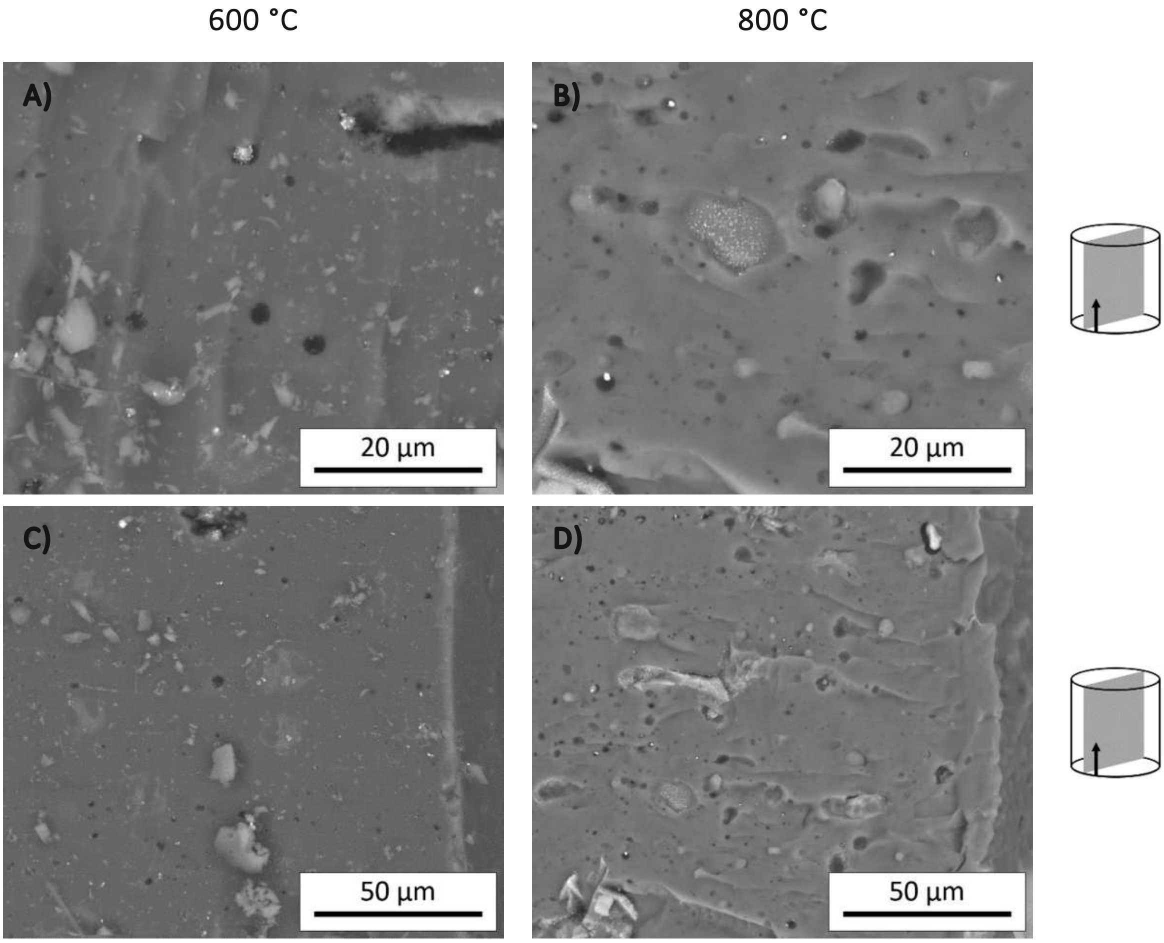

Figure 42: BSE-SEM images of 5Ni10T5UH cylinder fracture surfaces printed at Lithoz GmbH. (A/C) pyrolyzed at 600 °C; (B/D) pyrolyzed at 800 °C; (A/B) fracture surface shown perpendicular to the printing layers; (C/D) fracture surface at the sample surface shown perpendicular to the printing layers. Adjacent cylinders indicating the direction and plane of observation; arrow indicating the printing direction.

The fracture surfaces of the pyrolyzed cylinders do not show the same pore distribution as previous samples. Figure 42 A shows only minimal pore formation within the sample pyrolyzed at 600 °C. In the sample pyrolysed at 800 °C (Figure 42 B), more pores are visible and a higher Ni-concentration within the pores could be observed. Figure 42 C and D, do not reveal a surface layer different from the bulk material. The samples do not show the distinct printing layers observed in other samples printed at the desktop printer. This is most likely a result of the higher intensity used and the resulting shorter exposure time. In addition, the scraper blade may had also disrupted the formation of the distinct layers, as the micelles had no time to reorganize into individual layers. The formation of the layers mentioned will be discussed in more detail in the following section (5.3.2 – Distribution of Ni in ceramic matrix and phase composition).

5.3.2 Distribution of Ni in ceramic matrix and phase composition

It is not only the porosity that is crucial for good catalytic activity, but also the distribution of the Ni within the material.

Ni particle size and distribution

Due to the high molecular weight of Ni compared to the SiOC matrix, the Ni particles can be identified using BSE-SEM. Figure 43 and Figure 44 shows exemplary fracture surfaces of the sample 5Ni10T-800-R-Ar.

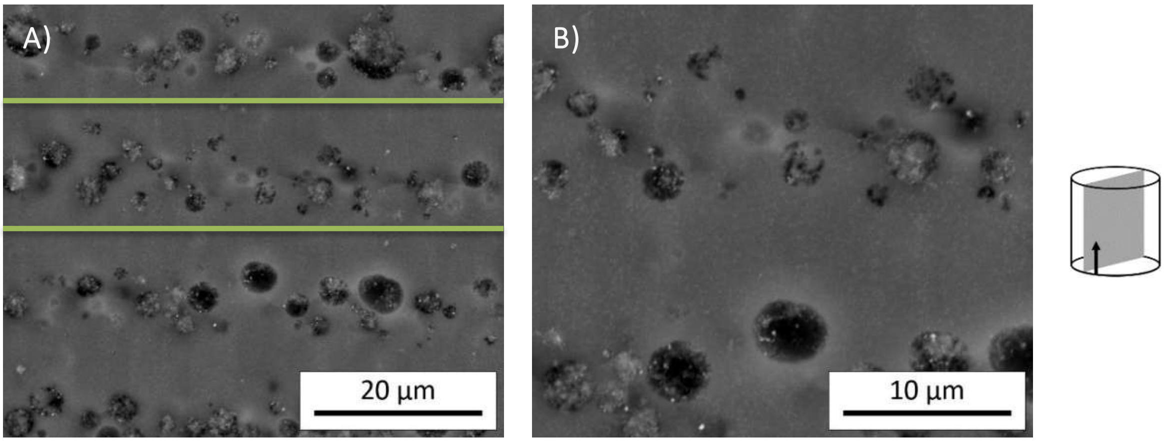

Figure 43: Backscatter electron SEM images of 5Ni10T-800-R-Ar fracture surfaces at various magnifications. (A) fracture surface with the green lines indicating the approximate individual printing layers, with pores originating from the former micelles, within the printing layers; (B) pores with Ni depositions and the surrounding bulk material. Adjacent cylinders indicating the direction and plane of observation; arrow indicating the printing direction.

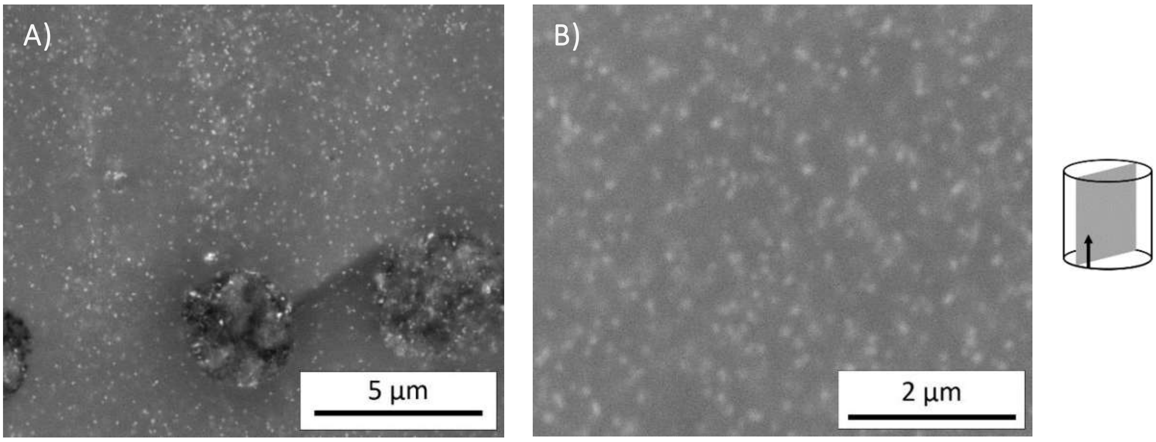

Figure 44: Backscatter electron SEM images of 5Ni10T-800-R-Ar fracture surfaces at various magnifications. (A) Pores, with Ni particles in the bulk material being visible as bright dots; (B) well distributed Ni particles in the bulk material. Adjacent cylinders indicating the direction and plane of observation; arrow indicating the printing direction.

The bright dots, indicating the presence of Ni, are well distributed in the bulk material. An accumulation of Ni in the pore walls is visible. The Ni particles were present and well distributed in all samples, regardless of the pyrolysis temperature used.

Since the individual particles are significantly smaller than 1 µm, the resolution of the BSE-SEM is not sufficient to resolve the particles. To determine the particle size, transmission electron microscopy (TEM) was used. Figure 45 shows an SEM image of the 5Ni10T-800-R-Ar sample after sample preparation (detailed information can be found in chapter 4.3.2 – Morphology).

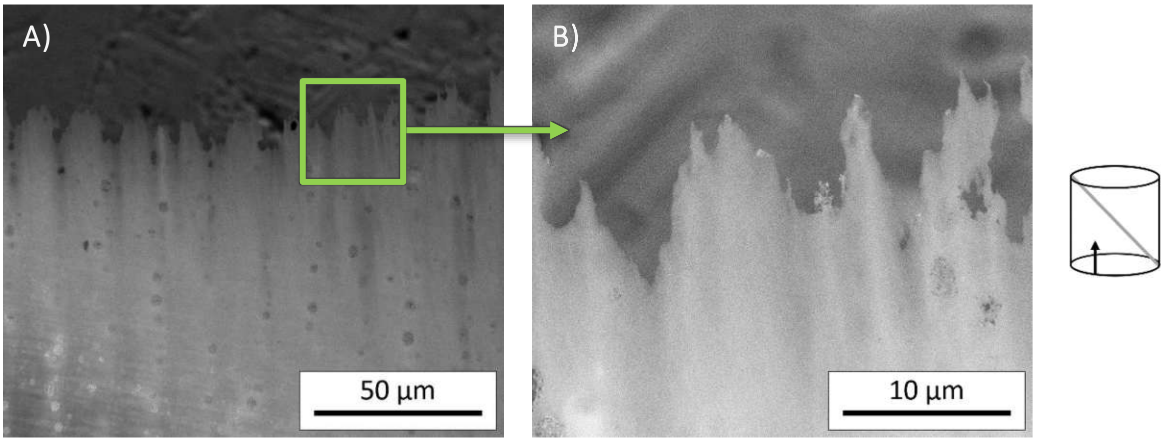

Figure 45: Secondary electron SEM images of 5Ni10T-800-R-Ar samples after sample preparation for TEM measurements. (A) edge area of the prepared sample with pores; (B) approximate area of TEM measurements. Adjacent cylinders indicating the direction and plane of observation; arrow indicating the printing direction.

The edge of the prepared sample is thin enough for electron transmittance, while still showing the Ni-rich pores embedded in the matrix. The prepared flat grind of the sample was placed on a copper ring and imaged by TEM, using the bright and dark field mode. Figure 46 shows two bright-field images of the scanning transmission electron microscope (STEM).

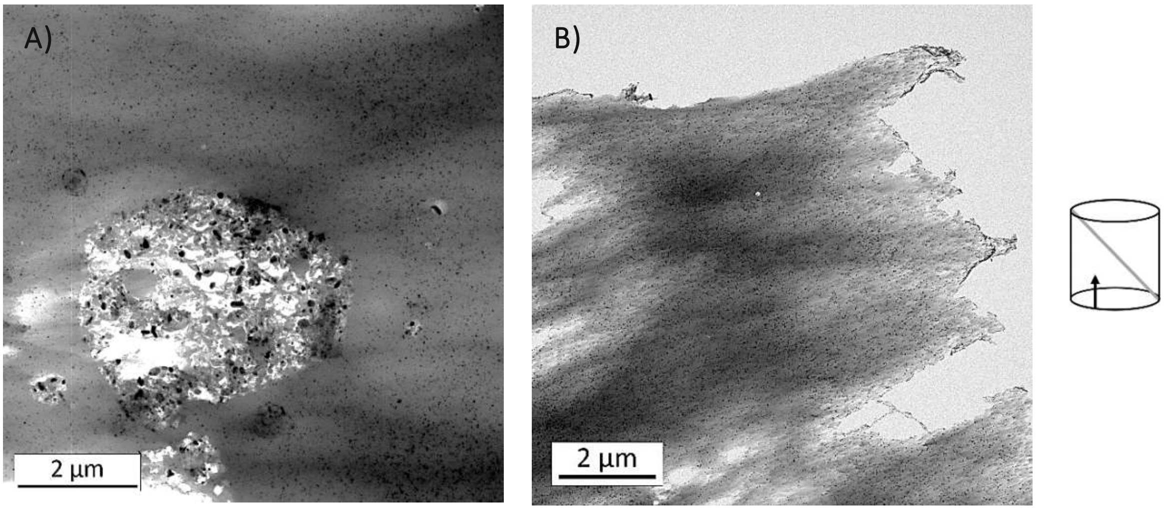

Figure 46: Bright-field TEM images of sample 5Ni10T-800-R-Ar; (A) pore with Ni enrichments and surrounding bulk material; (B) edge of the flat grind prepared. Adjacent cylinders indicating the direction and plane of observation; arrow indicating the printing direction.

In Figure 46 A one of the pores is visible, embedded in the Ni-modified SiOC matrix material. The dark Ni particles in the pores are larger than those in the bulk material.

This may originate from an incomplete solvation of the Ni (II) nitrate during resin preparation. Figure 47 shows bright-field TEM images of the Ni-modified bulk material.

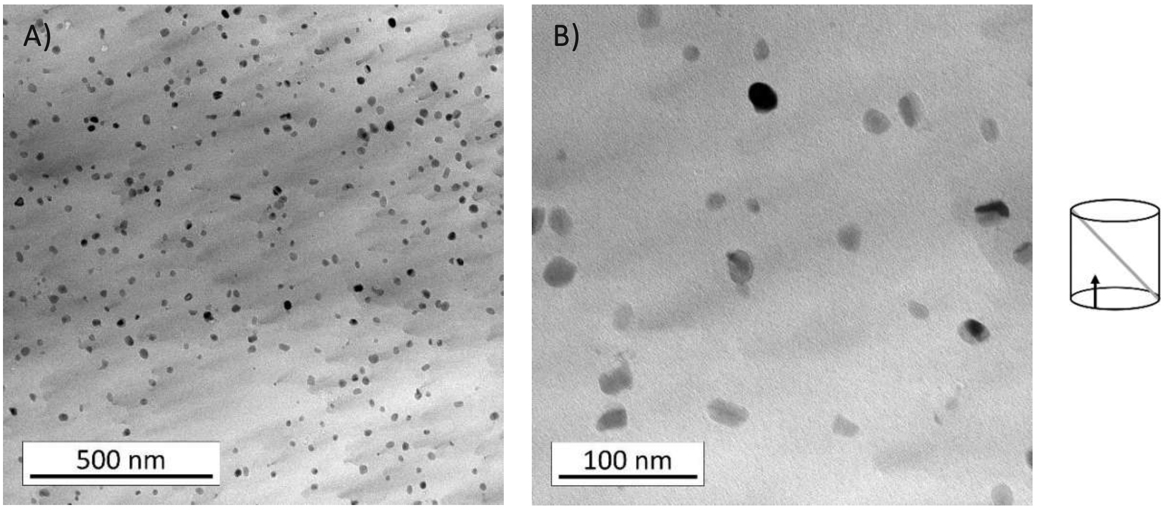

Figure 47: Bright-field TEM images of sample 5Ni10T-800-R-Ar. (A) Ni-modified bulk material; (B) bulk material at a higher magnification. Adjacent cylinders indicating the direction and plane of observation; arrow indicating the printing direction.

Ni particles in the bulk material are well distributed and do not agglomerate. The size of the particles depicted above varies a little, while still being well below 100 nm.

In addition to imaging, TEM enables the visualisation of lattice plains in crystalline materials at higher resolutions. Figure 48 shows high resolution TEM images of the Ni-modified bulk material surrounding the pores.

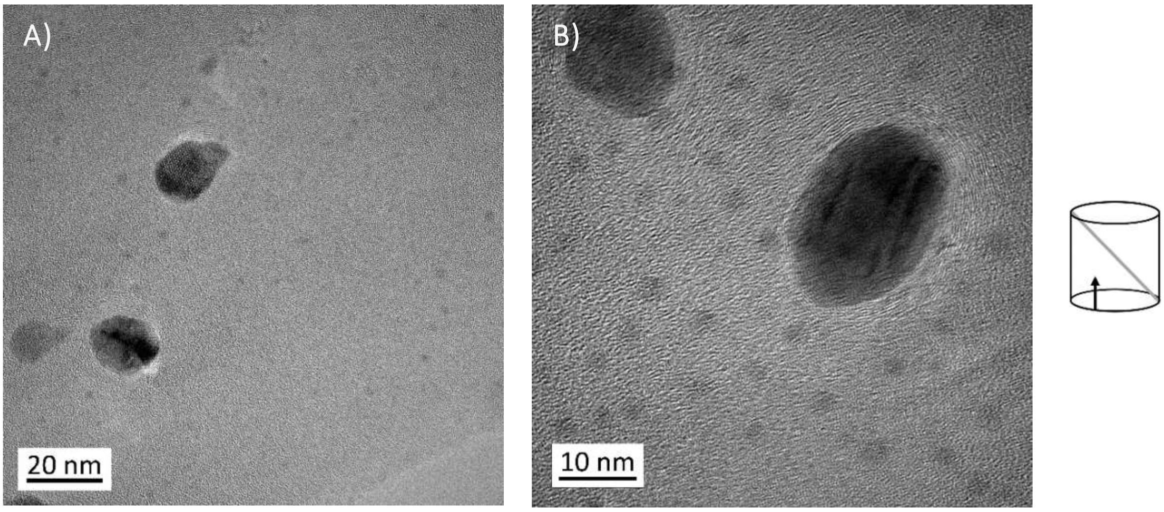

Figure 48: HR-TEM images of sample 5Ni10T-800-R-Ar. (A) bulk material with three bigger particles and small particles distributed in the remaining material; (B) bulk material with bigger and smaller Ni particles. The dark bigger particles show parts of the lattice planes due to the crystallinity of the particles. Surrounding the particles, curved lattice planes can be observed. Adjacent cylinders indicating the direction and plane of observation; arrow indicating the printing direction.

With the particles being about 10-20 nm in diameter, the lattice planes are difficult to determine precisely. In addition to the planes in the particles, there are diffraction effects visible surrounding the individual particles. This indicates the formation of another phase.

At higher magnifications, a second, smaller particle size fraction (dark contrast) homogeneously embedded within the SiOC matrix becomes visible. To determine the particle sizes, dark-field STEM images were recorded, providing a better contrast between the particles and the SiOC matirx. Figure 49 provides a better view at the two different particle sizes.

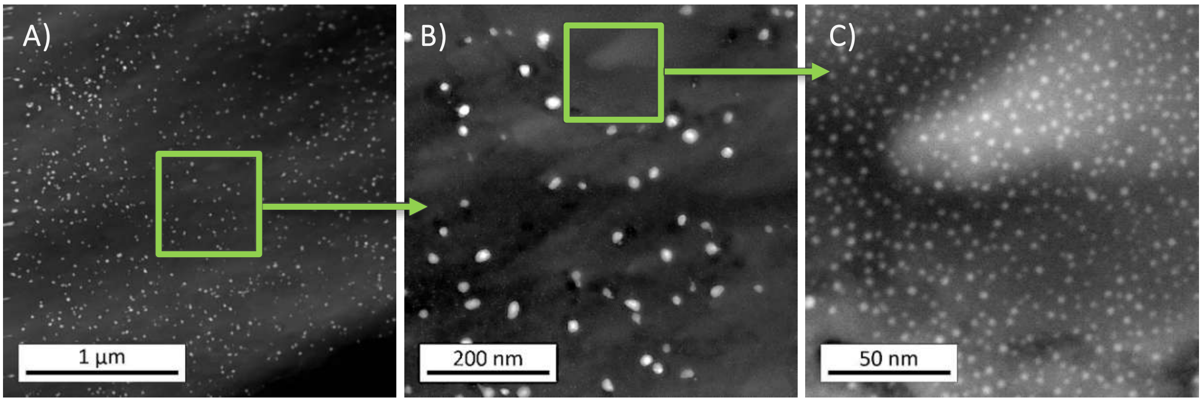

Figure 49: Dark-field STEM images of sample 5Ni10T-800-R-Ar. (A) SiOC bulk material with Ni particles (bright contrast) distributed within; (B) magnification of a selected area, as indicated by a green box. The smaller particles can be observed; (C) magnification of an area (green box) just containing the smaller particles embedded within the bulk material.

The material surrounding the bigger particles within the bulk material can be seen in Figure 49 A. At higher magnification (Figure 49 B), the small, bright particles can be distinguished. At even higher magnifications (Figure 49 C), the matrix material with small particles embedded within is shown.

Selected images where then chosen to determine particle sized using a particle analysis routine provided by the ImageJ software. The images were first converted into binary images and the region of interest was chosen. Figure 50 shows the three chosen TEM images for the determination of the particle sizes.

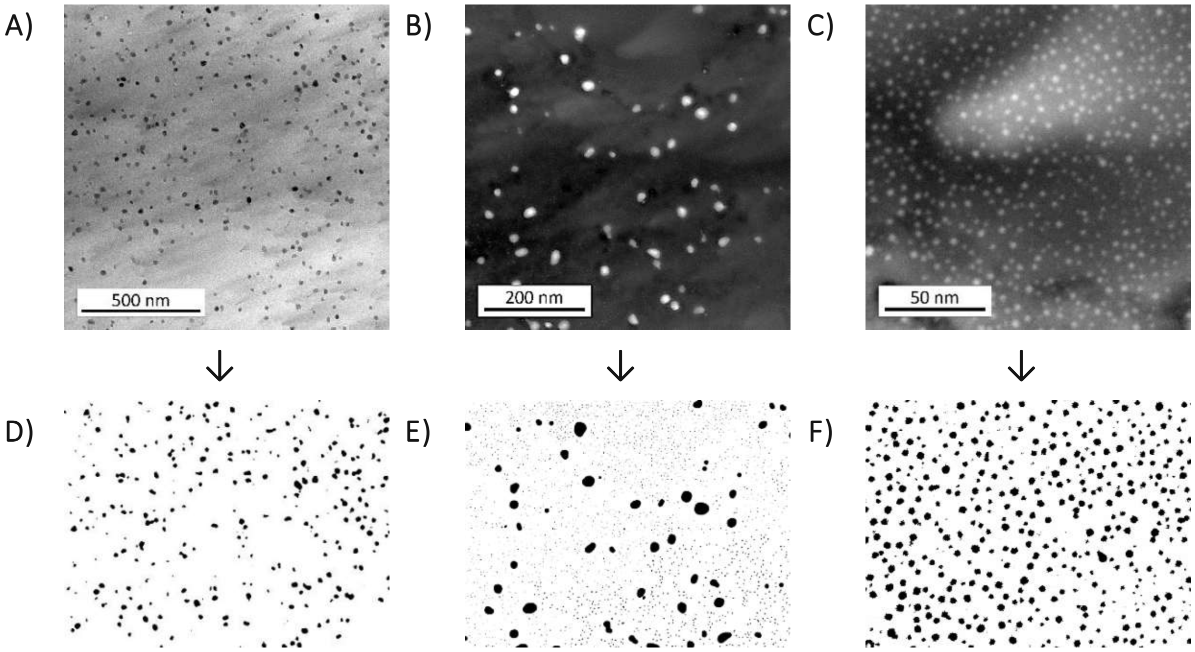

Figure 50: Images chosen for the determination of the particle sizes with the corresponding binary region of interest (D-F) below the image in question for sample 5Ni10T-800-R-Ar. (A) bright-field TEM image of the Ni-particles (dark contrast) within the bulk material; (B) dark-field STEM image SiOC bulk material with Ni-particles (bright contrast) distributed within the bulk material; (C) dark-field STEM image at a higher magnification of a selected area of (B).

(A) and (B) were used for determination of particle sizes of the bigger particles and (C) was used for determination of the size distribution of the smaller particle fraction. (B) was used to determine the approximate ratio between the two groups of particles. The evaluation of the area distribution of the particle sizes is shown in Figure 51.

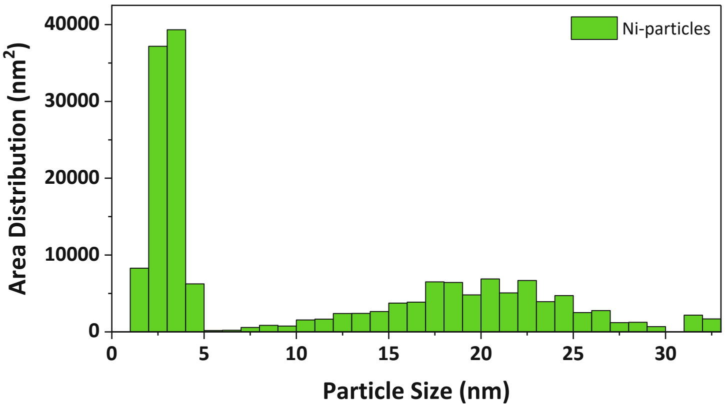

Figure 51: Area distribution of Ni-particles in the SiOC bulk material with sizes between 1 and 36 nm in average particle diameter. Calculations were done with the region of interest of the images depicted in Figure 50 D-F.

The bimodal average particle size distribution indicates that most of the particles have a diameter smaller than 5 nm, whereas the bigger particles show diameters between 10 nm and 30 nm. According to these calculations, the bigger, crystalline particles have an average particle size of 16.1 nm ± 5.7 nm. The smaller particle fraction shows an average particle size of 2.7 nm ± 0.7 nm. Nanocrystalline particles have thus been successfully distributed homogeneously in the SiOC matrix.

Material composition

The phase surrounding the bigger particles could result from graphite-like carbon being present within the samples. Another possibility is the formation of an intermetallic phase containing Ni and Si, forming around the Ni particles. The phase was investigated using TEM diffraction patterns. One exemplary diffraction pattern is shown in Figure 52.

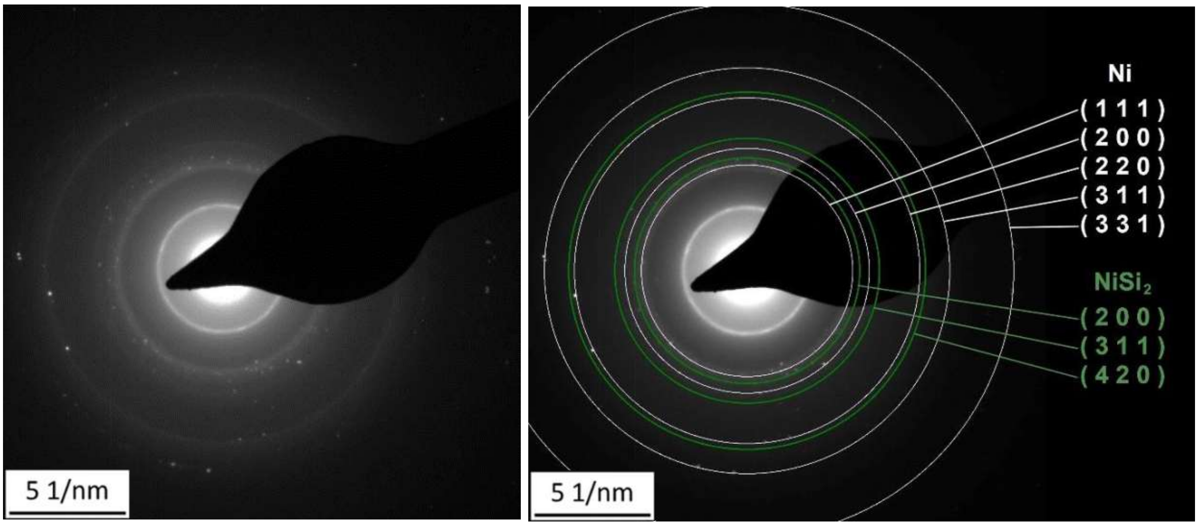

Figure 52: TEM diffraction pattern from sample 5Ni10T-800-R-Ar. (A) original image with dots indicating the location of the rings generated because of the differently orientated crystalline particles within the amorphous matrix; (B) diffraction pattern with some prominent lattice planes indicated with circles for Ni (white) and $NiSi_2$ (green).

The TEM diffraction patterns confirm the presence of a $NiSi_2$ phase. To validate these results, powder X-ray diffraction (XRD) was used. The resulting diffraction pattern of the milled 5Ni10T-800-R-Ar sample, corresponding to the sample investigated by TEM, is shown in Figure 53.

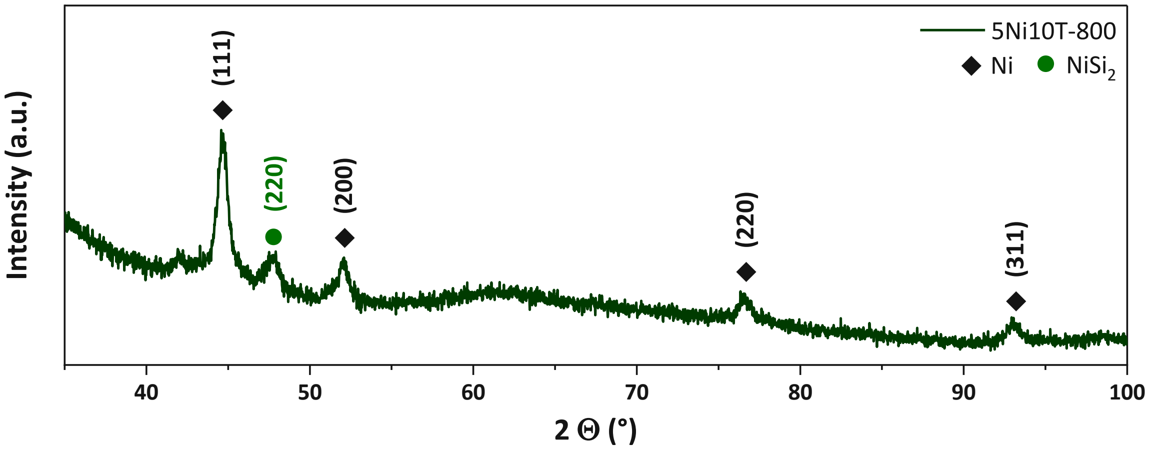

Figure 53: Powder X-ray diffraction pattern of sample 5Ni10T-800 after pyrolytic conversion at 800 °C. Indication of pronounced reflexes with the indication on the HKL indices for Ni (◆) and $NiSi_2$ (•).

Besides the Ni phase, the formed $NiSi_2$ phase can be observed. The small and widened reflexes result from the variety of small and dispersed particles.

The small signal next to the Ni (111) reflex (around 42°) could not be identified with certainty. The reflex may originate from graphite-like carbon or some already formed crystalline SiO_2. The presence of measurable amounts of NiO phase could be ruled out.

To observe any temperature dependent phase formation between 600 °C and 800 °C, samples made of 5Ni10T were characterised by means of XRD. Complementary, samples of 5Ni10T5U pyrolysed at all three temperatures (600, 700 and 800 °C) were analysed for a possible influence of UdMA on phase formation.

The resulting diffraction patterns including the corresponding phase determination are depicted in Figure 54. To simplify the comparison between the individual diffraction patters, the relative intensity of the diffractograms was normalized to the Ni (111) reflex.

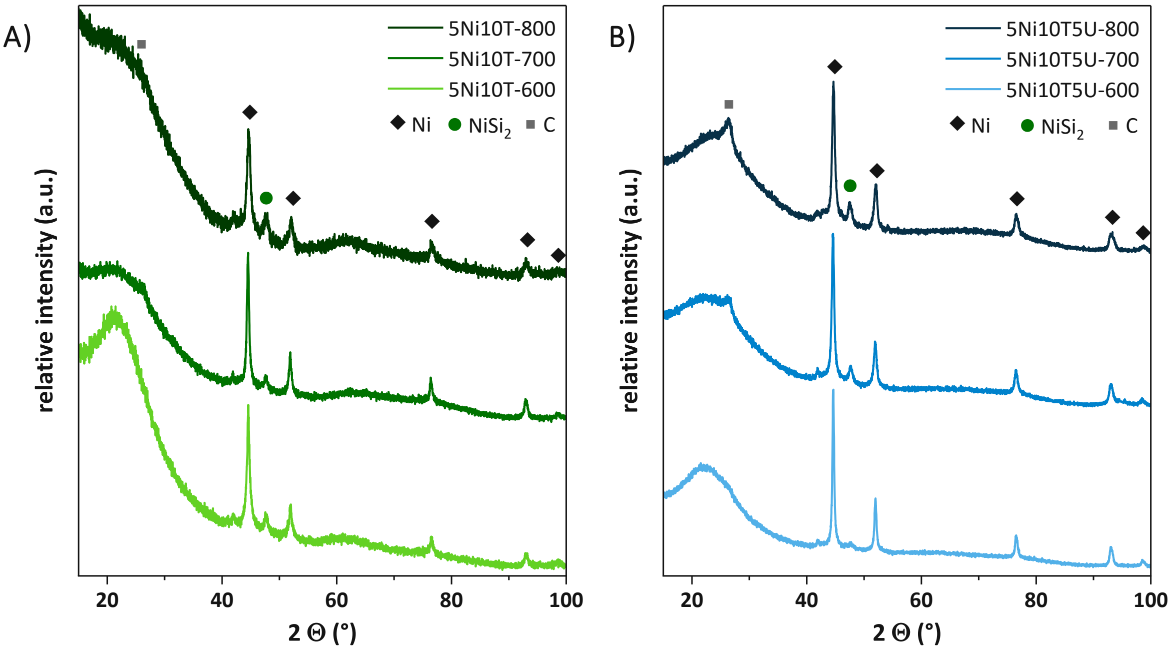

Figure 54: Powder XRD diffraction patterns of the samples 5Ni10T and 5Ni10T5U after pyrolytic conversion at 600, 700 and 800 °C (under Ar atmosphere, with additional dwell times). Indication of pronounced reflexes with the indication on the HKL indices for Ni (◆), $NiSi_2$ (•) and C (■). (A) 5Ni10T; (B) 5Ni10T5U

At lower diffraction angles, the amorphous material is visible as a broad shoulder. The most pronounced reflexes could be clearly assigned to Ni, demonstrating the successful introduction of crystalline Ni into the polymer-derived material. In accordance with the results of TEM measurements, a reflex could be assigned to the $NiSi_2$ phase. In addition, reflexes were found indicating the presence of graphite. The reflexes are more pronounced in the samples with the addition of UdMA, and the signal intensifies with the rise in pyrolysis temperature.

Using Rietveld refinement, the crystallite size of the Ni particles was determined through diffraction patterns. No significant temperature dependence of the Ni particle size could be observed, with the crystallite sizes varying between 14-20 nm in both the 5Ni10T and the 5Ni10T5U samples for all pyrolysis temperatures. This corresponds well with the size determination through TEM images of the bigger Ni particles in the SiOC matrix material (16,1 nm ± 5,7 nm).

In addition to the presence of crystalline Ni particles, the Ni content of the sample is also important for the catalytic activity. Since the material produced contains light elements such as C and O on the on one hand and heavier elements such as Si and Ni on the other, a quantitative determination is difficult. Therefore, different methods were combined to achieve the best possible results. The results obtained were then compared with each other.

The quantification of the Ni present within the material, other than calculation through the amount of the used materials to prepare the resin, is not executable with only one method: quantification of the lighter elements C and O was done by combustion analysis. The results were then used to determine the ration between Si, C and O in the reference material. For the sample 5Ni10T-800, the determination of the ratio between Si and Ni was done with three different methods: X-ray fluorescence spectroscopy (XRF), energy dispersive X-ray spectroscopy using a field emission gun as an electron source (FEG-EDX) and inductively coupled plasma – mass spectrometry (ICP-MS). The resulting material compositions are shown in Table 4.

Table 4: Elemental compositions and stoichiometric calculations, in relation to Si, of sample 5Ni10T-800 by combustion analysis (LECO), XRF, FEG-EDX and ICP-MS.

Element (wt%)	LECO	XRF	FEG-EDX	ICP-MS
C	19.3 ± 0.1			
O	30.2 ± 1.6			
Si		37.6 [a)]	41.5 [a)]	47.2 [b)]
Ni		12.7 [c)]	4.6 [c)]	3.1 [c)]
		$SiO_{1.20}C_{1.41}$ + 0.16 Ni [d)]	$SiO_{1.09}C_{1.28}$ + 0.05 Ni [d)]	$SiO_{1.16}C_{1.36}$ + 0.04 Ni [d)]

[a)] Si content is calculated as remainder to 100%. [b)] Ratio between Si and Ni was determined via ICP-MS and calculated as remainder to 100%. [c)] Determined by means of the method indicated. [d)] Empirical stoichiometric calculations with reference to Si. C and O content were determined via LECO (elemental analysis by combustion), the ratio between Si and Ni was determined by means of the method indicated.

Nitrogen was neglected for the stoichiometric calculations depicted in Table 4, as it is only a minor constituent at 0.22 ±0.04 wt%. Both the results for the matrix composition and the amount of Ni within the sample vary between the different methods. The results obtained by the combination of LECO and FEG-EDX result in a Ni content closest to the intended 5 wt% of Ni in the final pyrolyzed compound.

The reference material was also investigated my means of elemental analysis by combustion, resulting in a composition of $SiO_{0.80}C_{0.71}$ for Ref10T-600 and $SiO_{0.64}C_{0.96}$ for Ref10T-800.

To get a better insight into the chemical constitution of the surface and bulk material, surface sensitive X-ray photoelectron spectroscopy (XPS) measurements were carried out. The following measurements were realized with a 5Ni10T5U-800 sample. Three different sample locations were evaluated. One was the sample surface area (SA) and the other two were fracture surfaces, one of which was fractured in air (FS-air) and one in a glovebox under an inert Ar atmosphere (FS-gb). The measurements were carried out using the untreated samples (as received) and after sputtering with Ar-ions (sputtered). All received XPS spectra can be found in the Appendix, Figure A 1 to Figure A 3. Table 5 shows the results of the XPS measurements with respect to the quantification.

Table 5: Stoichiometric calculations, in relation to Si, and atomic percentage of Ni of sample 5Ni10T5U-800 by XPS measurements. Measurements were done at the surface (SA) and fracture surfaces fractured on air (FS-air) and under argon atmosphere in a glove box (FS-gb).

Sample	sputtered	composition	Ni
SA	No	$SiO_{3.67}C_{2.07}$	
FS-air	No	$SiO_{2.30}C_{2.11}$	Traces of Ni in Ni2p signal
FS-gb	No	$SiO_{3.43}C_{2.31}$	Traces of Ni in Ni2p signal
SA	Yes	$SiO_{1.56}C_{1.27}$	<0.1 at%
FS-air	Yes	$SiO_{1.48}C_{1.78}$ + 0.02 Ni	0.39 at%
FS-gb	Yes	$SiO_{1.88}C_{1.67}$ + 0.01 Ni	0.31 at%

All samples show the expected elements Si, O and C. Ni could not be detected in all of the measured spots. With the additional Ar sputtering, the amount of measured C decreases, leading to an increase of the relative amounts of Si and O. Ni could be detected only in overview spectra of fracture surfaces after Ar sputtering (0.31-0.39 at%). The detection limit in survey measurements usually lies around 0.1-0.5 at%.

Deconvolution of O1s and Si2p spectra show the major components around 533 eV and 103.5-103.9 eV, respectively, pointing to the presence of SiO_2. Regarding the Ni within the samples, the highest signals for Ni 2p peaks could be found at around 853.6 eV BE, indicating the bonding environment of NiO. The presence of NiO could not be confirmed by powder XRD measurements.

With various measurement methods, it was thus possible to determine matrix compositions with $SiO_{1.09}C_{1.28}$ (FEG-EDX) representing the highest Si content. All other methods resulted in a lower calculated Si content for Ni-modified samples. Varying results were also obtained when quantifying the Ni content. Therefore, no measurement method could be found which could provide useful results for both the quantification of the matrix elements and the determination of the Ni content. The obtained results only present an approximate impression of the sample composition.

5.3.3 Specific surface area

Besides the presence of catalytically active Ni at the surface of the material, a high available specific surface area (SSA) is necessary to improve the catalytic activity. N_2 adsorption and desorption isotherms were recorded at -196 °C to determine the SSA using the BET method. Porosity is generated through the gases released during the polymer-to-ceramic transformation due to the decomposition of volatile organic groups as well as the residual solvents and added TMPTMA and UdMA. The linear shrinkage due to the pyrolysis works against pore formation by compacting the ceramer, leading to collapsed pores.

Table 6 shows the results of the SSA determination of selected PDC samples from this work. The measurements were conducted by *Szoldatits* [41] and detailed information can be found in the according work.

Table 6: Specific surface area according to BET theory of reference materials (Ref10T-600 and Ref10T-800), a Ni-modified sample (5Ni10T-800) and Ni-modified samples with the addition of UdMA (5Ni10T5U-600 and 5Ni10T5U-800). Printed and pyrolyzed components as well as resulting powders were analysed.

Sample	S_{BET} (m^2/g)	
	Component	Powder
Ref10T-600	132	367
Ref10T-800	/	90
5Ni10T-800	<1	129
5Ni10T5U-600	85	410
5Ni10T5U-800	2	20

All samples show a higher specific surface area after milling the pyrolyzed components. This indicates that the existing porosity is not fully accessible for the gases used during the thermal catalysis. The reference material Ref10T-600 shows the highest SSA of the components, at 132 m^2/g, with the powdered sample having an even higher SSA of 367 m^2/g. The reference material as well as the Ni-modified sample with the addition of UdMA show a higher SSA at lower pyrolysis temperatures. The highest SSA was achieved with the milled 5Ni10T5U-600 sample, at 410 m^2/g. When comparing the results for the milled Ref10T-800 and 5Ni10T-800 samples, a slight increase in SSA is noticeable. This could be caused by an enhanced decomposition of the siloxanes around the Ni nanoparticles and the presence of pore-forming micelles, leading to a higher surface once the sample is milled. A higher porosity enables more accessible nanopores, which can be observed using BET. The comparative low SSA of the 5Ni10T5U-800 may be a result from the graphite-like carbon that could be observed through XRD measurements (Figure 54). The formed carbon can block the existing porosity, leading to a lower SSA.

The obtained pore size distribution does not show any indication for the presence of hierarchical porosity up to 100 nm pore diameter, with an average pore width between 2-6 nm.

5.4 Catalytic Activity

Evaluation of the catalytic activity of the prepared Ni-modified ceramers with respect to the CO_2 methanation was conducted by *Szoldatits* [41] in the setup described in chapter 4.3.3 (Catalytic activity). Figure 55 below shows the results for the CO_2 conversion (X_{CO2}) and the selectivity towards methane (S_{CH4}) during the thermal catalysis (400 °C) with a gas feed consisting of CO_2:H_2:He in a ratio of 1:4:5.

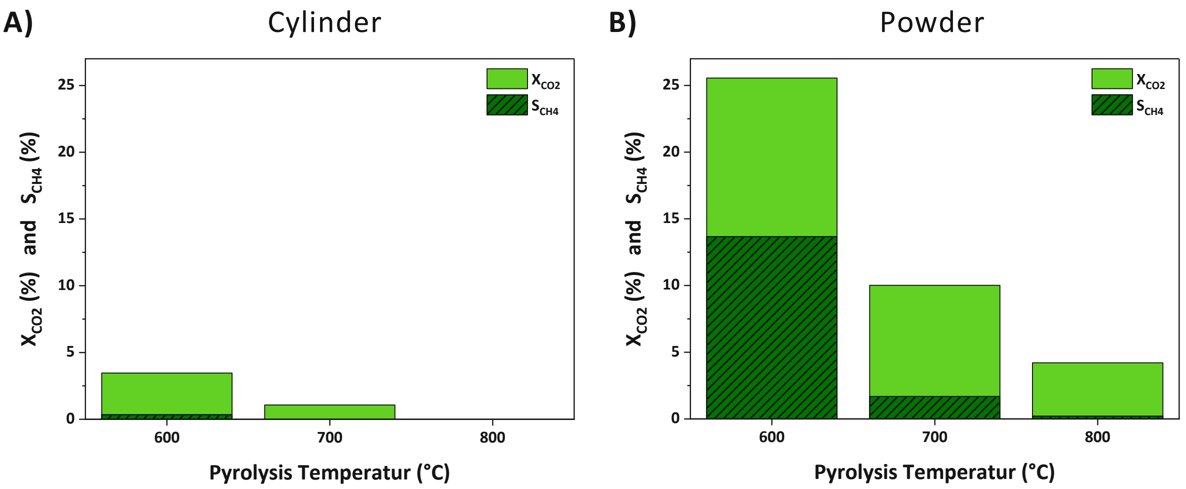

Figure 55: CO_2 conversion and corresponding selectivity to methane at 400 °C of printed 5Ni10T5U samples after pyrolysis at 600, 700 and 800 °C. (A) cylinders as depicted in Figure 39 B, with diameters between 1.6-1.8 mm and heights between 3.2-3.7 mm, depending on pyrolysis temperature; (B) resulting powders using a mixer mill (particle sizes below 180 µm)

Milled 5Ni10T5U samples show a much higher activity compared to the components due to the higher SSA, resulting in more available Ni sites. Furthermore, samples pyrolyzed at 600 °C show a higher catalytic activity than those pyrolyzed at higher temperatures. On the one hand, this is a result from the higher SSA, as discussed in 5.3.3 – Specific surface area.

On the other hand, different surface characteristics could be observed, influencing the catalytic activity. During the sample preparation, a hydrophobic character of the samples pyrolyzed at 600 °C could be observed. With increasing pyrolysis temperature, the samples became hydrophilic. This can be verified by the conducted ATR-FTIR measurements, showing no H_2O-bands resulting of adsorbed water on the samples pyrolyzed at 600 °C (Figure 23 B). Since water is a by-product during CO_2 methanation, hydrophobic properties of the sample are beneficial for catalytic activity because it prevents water from blocking the adsorption sites. This phenomenon was previously discussed by *Schumacher et. al.* [18].

In addition to the higher CO_2 conversion at lower pyrolysis temperatures, a higher selectivity towards methane at lower pyrolysis temperatures could be observed. The maximum catalytic activity was observed for sample 5Ni10T5U-600 at 400 °C, with a CO_2 conversion of 25,55% and a selectivity towards methane of 53,47%. All results from catalytic activity experiments, including data from samples 5Ni10T and the milled reference materials Ref10T-600 and Ref10T-800, are listed in Table 7.

Table 7: CO_2 conversion and corresponding selectivity to methane of different samples at temperatures between 200 °C and 400 °C.

	200 °C		250 °C		300 °C		350 °C		400 °C	
sample	X_{CO2} (%)	S_{CH4} (%)	X_{CO2} (%)	S_{CH4} (%)	X_{CO2} (%)	S_{CH4} (%)	X_{CO2} (%)	S_{CH4} (%)	X_{CO2} (%)	S_{CH4} (%)
5Ni10T-800_C	0.00	0.00	0.00	0.00	0.00	0.00	0.00	0.00	0.17	0.00
5Ni10T-800_P	0.00	0.00	0.00	0.00	0.00	0.00	0.37	100.00	1.22	100.00
5Ni10T5U-600_C	0.00	0.00	0.00	0.00	0.06	0.00	1.07	0.00	3.46	9.84
5Ni10T5U-600_P	0.00	0.00	0.00	0.00	1.83	4.57	10.76	41.44	25.55	53.47
5Ni10T5U-700_C	0.00	0.00	0.00	0.00	0.00	0.00	0.05	0.00	1.07	0.00
5Ni10T5U-700_P	0.00	0.00	0.00	0.00	0.54	0.00	3.29	14.54	10.02	16.85
5Ni10T5U-800_C	0.00	0.00	0.00	0.00	0.00	0.00	0.00	0.00	0.00	0.00
5Ni10T5U-800_P	0.00	0.00	0.00	0.00	0.00	0.00	1.10	0.00	4.21	4.82
Ref10T-600_P	0.00	0.00	0.00	0.00	0.00	0.00	0.24	0.00	1.38	0.00
Ref10T-800_P	0.00	0.00	0.00	0.00	0.00	0.00	0.65	0.00	3.17	0.00

X_{CO2}: total CO_2 conversion into other molecules, calculated with equation(A 1); S_{CH4}: selectivity towards methane, calculated with equation (A 2). The measurements of the different temperatures for the thermal catalysis were conducted as depicted in Figure 9.

The catalytic activity increases with rising temperatures for all samples. Comparing the samples 5Ni10T-800 and 5Ni10T5U-800, the sample with the addition of UdMA shows a higher catalytic activity due to the higher SSA, and some activity at lower catalysis temperatures. The activity of the milled 5Ni10T-800 samples is lower, although this material exhibits a higher selectivity towards methane, resulting in a higher overall methane generation despite the lower catalytic activity.

The milled reference materials were tested to validate that the catalytic activity of the material indeed stems from the added Ni. Even though both reference materials (Ref10T-600 and Ref10T-800) showed minor catalytic activity in terms of CO_2 conversion, no methane could be detected.

6 Conclusions and Outlook

In summary, a novel Ni-modified preceramic polymer system suitable for additive manufacturing by vat-based photopolymerization was developed. The resin was modified using methacrylic acid and Ni(II)nitrate as a metal precursor. The resulting phase separation could be stabilized into spherical micelles using Tween20 and further stabilized by the addition of hydroquinone. The photopolymerisation-based additive manufacturing of various solid compounds and grid structures with strut sizes down to 400 µm could be achieved.

Pronounced phase separation and rapid gelation makes wide application difficult, as the material must always be produced fresh. A positive influence of hydroquinone has been observed, but still the Ni-modified resin produced cannot be stored overnight.

The addition of TMPTMA as a reactive diluent resulted in lower resin viscosity and higher stability of the printed green bodies. Increasing the amount of TMPTMA resulted in higher storage modulus, greater shrinkage, and lower double bond conversion, which was still above 85% at 20 wt% TMPTMA. The Ni-modified resins reached the gel point faster (2.3 s) than the reference material (3.1 s). For printing of the grid structures, the exposure times had to be adjusted as the Ni-modified resin required a longer exposure time (18 s) compared to the reference material (12 s). Due to the pronounced phase separation, the light is scattered and attenuated earlier in the Ni-modified samples, so it does not reach the depth of the resin as easily. Printing of solid structures was possible with shorter exposure times for the individual printing layers.

The pyrolysis in Ar atmosphere was carried out at temperatures up to 600, 700 and 800 °C. Increasing the pyrolysis temperature resulted in higher linear shrinkage and a higher weight loss, levelling off at about 800 °C, indicating that the majority of the polymer-to-ceramic conversion has occurred. A dependence between the different geometries and the resulting linear shrinkage and ceramic yield could be observed. In comparison, the reference material without Ni addition shows a lower ceramic yield and a higher linear shrinkage after pyrolysis. The addition of Ni shifted the pyrolytic conversion to lower temperatures, indicating that Ni catalyses the decomposition and conversion to a certain extent.

Crack formation could be observed after pyrolysis, even at slow heating rates and with the addition of intermediate dwell times. The formation of cracks is dependent on the geometry and the presence of Ni. The reference material showed a pronounced crack formation perpendicular to the printing direction. Cracking is detrimental to the stability of the components and should therefore be avoided. By choosing the right geometries and pyrolysis conditions, cracking can be minimized.

All Ni-modified samples exhibit a rough surface in contrast to the reference material, which had a smooth surface and a homogeneous matrix material. Due to the micelles in the Ni-modified resin, which resulted in pores after pyrolysis, these specimens did not exhibit a smooth fracture surface. The Ni-rich former micelles are well distributed within the individual printing layers. The surrounding bulk material showed nanocrystalline Ni particles with average diameters between 10-30 nm. The determination of the crystallite size by XRD resulted in a crystallite size for the Ni phase between 14-20 nm. In addition to these larger particles, TEM imaging revealed a second, smaller particle fraction up to 5 nm in average diameter. Consequently, the bulk material showed a bimodal average Ni particle size distribution. Furthermore, another Ni-containing phase, $NiSi_2$, was detected, which was presumably formed between the Ni particles and the surrounding SiOC matrix. Regarding the surface area and BSE-SEM imaging revealed a rather dense surface layer, with a comparably lower Ni concentration. XPS measurements recorded at the surface area confirm the low Ni concentration in the outer layers. This interferes with the catalytic application.

Quantification of the Ni present in the sample using a combination of combustion analysis and EDX provided the results closest to the calculated values, with $SiO_{1.09}C_{1.28}$ + 0.05 Ni for sample 5Ni10T-800. Due to the SiOC matrix consisting mainly of light elements, quantification is difficult and needs further optimisation.

The SSA of the Ni-modified components was very low and could be significantly increased by milling the pyrolyzed material. This indicates that the existing position within the printed structures is not accessible for catalysis. A further increase of the SSA could be achieved by lowering the pyrolysis temperature and adding UdMA, with a maximal BET specific surface area of 410 m^2/g and an average pore width of 2-6 nm. There was no indication found for the presence of hierarchical porosity.

Ultimately, the investigation of the catalytic activity revealed that the material is indeed suitable for catalysing CO_2 methanation. As was shown for the changes in SSA, a higher activity could be detected for samples pyrolyzed at lower temperatures and with the addition of UdMA. Besides the higher SSA, which results in more accessible Ni sites, the hydrophobicity of the sample surface may affect the catalytic activity. Samples pyrolyzed at 600 °C revealed to be hydrophobic, which is beneficial for the catalysis by preventing emerging water (a by-product of catalysis) from blocking the adsorption sites. A maximum in catalytic activity was found for a sample containing 5 wt% UdMA pyrolysed at 600 °C, which exhibited the highest SSA and resulted in a CO_2 conversion of 25,55% and a selectivity towards methane of 53,47%. The sample in question contained 5 wt% UdMA, was pyrolysed at 600 °C, and also had the highest SSA.

Recalling the results of this work, further possibilities for continued research arise. The chosen manufacturing process allows for the modification to be carried out with other metals such as Co, Cu or Fe. This in turn could allow for new ranges of applications.

The influence of pyrolysis conditions such as temperature, atmosphere and heating rate, require further investigation. Complementary investigations should be conducted, especially regarding temperature resistance and stability during catalysis. Subsequently, the material can be studied in terms of catalysis of other reactions.

Another challenge is to figure out how to increase the pyrolysis temperature without compromising the SSA and catalytic activity, which currently both show better results at lower temperatures. Increasing the SSA through a variation of the pyrolysis conditions, sacrificial fillers, or through targeted phase segregation is a topic for further investigation.

Consequently, this work is an important step towards the fabrication of catalysts through modified PDCs using vat-based photopolymerization as a method for additive manufacturing. Ni-modified SiOC with nanocrystalline Ni particles was successfully developed with the material showing catalytic activity towards CO_2 methanation. To further improve the catalytic activity, a high SSA is necessary, which may be achieved through the generation of hierarchical porosity in the future. Moreover, more accessible Ni sites on the surface are necessary to increase the catalytic properties of the material.

References

1. Macedo, H.P., *Ni-Containing Hybrid Ceramics Derived from Polysiloxanes for Production of CH4 via Hydrogenation of CO2*. 2018, Doctoral Thesis, Federal University od Rio Grande do Norte
2. Jin, G.; Gu, F.; Liu, Q.; Wang, X.; Jia, L.; Xu, G.; Zhong, Z. and Su, F., *Highly stable Ni/SiC catalyst modified by Al2O3 for CO methanation reaction.* RSC Advances, 2016. **6**(12): p. 9631-9639.
3. Ashok, J.; Pati, S.; Hongmanorom, P.; Tianxi, Z.; Junmei, C. and Kawi, S., *A review of recent catalyst advances in CO2 methanation processes.* Catalysis Today, 2020. **356**: p. 471-489.
4. Essmeister, J.; Altun, A.A.; Staudacher, M.; Lube, T.; Schwentenwein, M. and Konegger, T., *Stereolithography-based additive manufacturing of polymer-derived SiOC/SiC ceramic composites.* Journal of the European Ceramic Society, 2022. **42**(13): p. 5343-5354.
5. Colombo, P.; Mera, G.; Riedel, R. and Sorarù, G.D., *Polymer-Derived Ceramics: 40 Years of Research and Innovation in Advanced Ceramics.* Journal of the American Ceramic Society, 2010: p. no-no.
6. Porosoff, M.D.; Yan, B. and Chen, J.G., *Catalytic reduction of CO2 by H2 for synthesis of CO, methanol and hydrocarbons: challenges and opportunities.* Energy & Environmental Science, 2016. **9**(1): p. 62-73.
7. Wu, H.C.; Chang, Y.C.; Wu, J.H.; Lin, J.H.; Lin, I.K. and Chen, C.S., *Methanation of CO2 and reverse water gas shift reactions on Ni/SiO2 catalysts: the influence of particle size on selectivity and reaction pathway.* Catalysis Science & Technology, 2015. **5**(8): p. 4154-4163.
8. Macedo, H.P.; Medeiros, R.L.B.A.; Ilsemann, J.; Melo, D.M.A.; Rezwan, K. and Wilhelm, M., *Nickel-containing hybrid ceramics derived from polysiloxanes with hierarchical porosity for CO2 methanation.* Microporous and Mesoporous Materials, 2019. **278**: p. 156-166.
9. Tsiotsias, A.I.; Charisiou, N.D.; Yentekakis, I.V. and Goula, M.A., *Bimetallic Ni-Based Catalysts for CO2 Methanation: A Review.* Nanomaterials (Basel), 2020. **11**(1).
10. Wei, W. and Jinlong, G., *Methanation of carbon dioxide: an overview.* Frontiers of Chemical Science and Engineering, 2010. **5**(1): p. 2-10.
11. Burger, T.; Donaubauer, P. and Hinrichsen, O., *On the kinetics of the co-methanation of CO and CO2 on a co-precipitated Ni-Al catalyst.* Applied Catalysis B: Environmental, 2021. **282**.

12. Zaheer, M.; Schmalz, T.; Motz, G. and Kempe, R., *Polymer derived non-oxide ceramics modified with late transition metals.* Chemical Society Reviews, 2012. **41**(15): p. 5102-16.

13. Le, T.A.; Kang, J.K. and Park, E.D., *CO and CO2 Methanation Over Ni/SiC and Ni/SiO2 Catalysts.* Topics in Catalysis, 2018. **61**(15-17): p. 1537-1544.

14. Zelinski, B.J.J. and Uhlmann, D.R., *Gel Technology in Ceramics.* Journal of Physics and Chemistry of Solids, 1984. **45**: p. 1069-1090.

15. Rasaki, S.A.; Xiong, D.; Xiong, S.; Su, F.; Idrees, M. and Chen, Z., *Photopolymerization-based additive manufacturing of ceramics: A systematic review.* Journal of Advanced Ceramics, 2021. **10**(3): p. 442-471.

16. Pantano, C.G.; Singhm, A.K. and Zhang, H., *Silicon Oxycarbide Glasses.* Journal of Sol-Gel Science and Technology, 1999.

17. Wilhelm, M.; Adam, M.; Bäumer, M. and Grathwohl, G., *Synthesis and Properties of Porous Hybrid Materials containing Metallic Nanoparticles.* Advanced Engineering Materials, 2008. **10**(3): p. 241-245.

18. Schumacher, D.; Wilhelm, M. and Rezwan, K., *Porous SiOC monoliths with catalytic activity by in situ formation of Ni nanoparticles in solution-based freeze casting.* Journal of the American Ceramic Society, 2020. **103**(5): p. 2991-3001.

19. Segatelli, M.G.; Pires, A.T.N. and Yoshida, I.V.P., *Synthesis and structural characterization of carbon-rich SiCxOy derived from a Ni-containing hybrid polymer.* Journal of the European Ceramic Society, 2008. **28**(11): p. 2247-2257.

20. Ma, C.; He, C.; Wang, W.; Yao, X.; Yan, L.; Hou, F.; Liu, J. and Guo, A., *Metal-doped polymer-derived SiOC composites with inorganic metal salt as the metal source by digital light processing 3D printing.* Virtual and Physical Prototyping, 2020. **15**(3): p. 294-306.

21. Fu, Y.; Xu, G.; Chen, Z.; liu, C.; Wang, D. and Lao, C., *Multiple metals doped polymer-derived SiOC ceramics for 3D printing.* Ceramics International, 2018. **44**(10): p. 11030-11038.

22. Adam, M.; Wilhelm, M. and Grathwohl, G., *Polysiloxane derived hybrid ceramics with nanodispersed Pt.* Microporous and Mesoporous Materials, 2012. **151**: p. 195-200.

23. Zakeri, S.; Vippola, M. and Levänen, E., *A comprehensive review of the photopolymerization of ceramic resins used in stereolithography.* Additive Manufacturing, 2020. **35**.

24. Eckel, Z.C.; Zhou, C.; Martin, J.H.; Jacobsen, A.J.; Carter, W.B. and Schaedler, T.A., *Additive manufacturing of polymer-derived ceramics.* Science, 2016. **351**(6268): p. 58-62.

25. Zanchetta, E.; Cattaldo, M.; Franchin, G.; Schwentenwein, M.; Homa, J.; Brusatin, G. and Colombo, P., *Stereolithography of SiOC Ceramic Microcomponents.* Adv Mater, 2016. **28**(2): p. 370-6.

26. Ding, G.; He, R.; Zhang, K.; Xie, C.; Wang, M.; Yang, Y. and Fang, D., *Stereolithography-based additive manufacturing of gray-colored SiC ceramic green body.* Journal of the American Ceramic Society, 2019. **102**(12): p. 7198-7209.

27. Halloran, J.W., *Ceramic Stereolithography: Additive Manufacturing for Ceramics by Photopolymerization.* Annual Review of Materials Research, 2016. **46**(1): p. 19-40.

28. de Hazan, Y. and Penner, D., *SiC and SiOC ceramic articles produced by stereolithography of acrylate modified polycarbosilane systems.* Journal of the European Ceramic Society, 2017. **37**(16): p. 5205-5212.

29. Schmidt, J. and Colombo, P., *Digital light processing of ceramic components from polysiloxanes.* Journal of the European Ceramic Society, 2018. **38**(1): p. 57-66.

30. Wang, X.; Schmidt, F.; Hanaor, D.; Kamm, P.H.; Li, S. and Gurlo, A., *Additive manufacturing of ceramics from preceramic polymers: A versatile stereolithographic approach assisted by thiol-ene click chemistry.* Additive Manufacturing, 2019. **27**: p. 80-90.

31. Zocca, A.; Colombo, P.; Gomes, C.M.; Günster, J. and Green, D.J., *Additive Manufacturing of Ceramics: Issues, Potentialities, and Opportunities.* Journal of the American Ceramic Society, 2015. **98**(7): p. 1983-2001.

32. Li, Z.; Chen, Z.; Liu, J.; Fu, Y.; Liu, C.; Wang, P.; Jiang, M. and Lao, C., *Additive manufacturing of lightweight and high-strength polymer-derived SiOC ceramics.* Virtual and Physical Prototyping, 2020. **15**(2): p. 163-177.

33. Gorsche, C.; Harikrishna, R.; Baudis, S.; Knaack, P.; Husar, B.; Laeuger, J.; Hoffmann, H. and Liska, R., *Real Time-NIR/MIR-Photorheology: A Versatile Tool for the in Situ Characterization of Photopolymerization Reactions.* Analytical Chemistry 2017. **89**(9): p. 4958-4968.

34. Shirley, D.A., *High-Resolution X-Ray Photoemission Spectrum of the Valence Bands of Gold.* Physical Review B, 1972. **5**(12): p. 4709-4714.

35. Tougaard, S., *Universality Classes of Inelastic Electron Scattering Cross-sections.* Surface and Interface Analysis 1997. **25**.

36. Scofield, J.H., *Hartree-Slater subshell photoionization cross-sections at 1254 and 1487 eV.* Journal of Electron Spectroscopy and Related Phenomena, 1976. **8**.

37. Yeh, J. and Lindau, I., *Atomic subshell photoionization cross sections and asymmetry parameters: 1 ⩽ Z ⩽ 103.* Atomic Data and Nuclear Data Tables, 1985. **32**(1): p. 1-155.

38. Beamson, G. and Briggs, D., *High ResolutionXPS of Organic Polymers: The Scienta ESCA300 Database*. 1992.

39. Wagner, C.D.; Naumkin, A.V.; Kraut-Vass, A.; Allison, J.W.; Powell, C.J. and Rumble, J.R., *NIST Standard Reference Database 20*. 2003.

40. Herzig, C.; Frank, J.; Opitz, A.K.; Fleig, J. and Limbeck, A., *Quantitative imaging of structured complex metal oxide thin films using online-LASIL-ICP-MS.* Talanta, 2020. **217**: p. 121012.
41. Szoldatits, E.M., *Catalytic Properties of Functionalized Polymer-Derived Ceramics Produced by Additive Manufacturing*. 2022, Diploma Thesis, Technische Universität Wien.
42. Socrates, G., *Infrared and Raman Characteristic Group Frequencies: Tables and Charts*. 2004: John Wiley & Sons.

Appendix

Table A 1: ICP-MS: detection system parameters

Parameter	Setting
RF Power (W)	1550
Nebulizer gas flow (l/min)	1.05
Cool gas flow (l/min)	14
Auxiliary gas flow (l/min)	0,65
Dwell time (s)	0,01

Table A 2: ICP-MS: measurement laser parameters

Parameter	Setting
Laser fluence (J/cm^2)	0.76
Spot size (µm)	100
Scan speed (mm/s)	0.2
Repetition rate (Hz)	10
Liquid carrier solution flow (ml/min)	0.4

Table A 3: Catalytic activity: measurement setup parameters for the Micro GC

Parameter	Module A	Module B
Column type	Mole sieve	PLOT-Q
Inject time (ms)	0	25
Backflush time (s)	15	-
Temperature injector (°C)	90	90
Temperature detector (°C)	70	70
Column pressure (psi)	30	15
Temperature Column (°C)	60	60
Hold time (s)	450	450
Sample pump (s)	20	20

The CO_2 conversion X_{CO2} and the selectivity to methane S_{CH4} were calculated according to Equations (A 1) and (A 2).

$$X_{CO_2}(\%) = \frac{[CO_2]_{in} - [CO_2]_{out}}{[CO_2]_{in}} \cdot 100 \qquad \text{(A 1)}$$

$$S_{CH_4}(\%) = \frac{[CH_4]_{out}}{[CO_2]_{in} - [CO_2]_{out}} \cdot 100 \qquad \text{(A 2)}$$

X_{CO2} ……..…… CO_2 conversion (%)
S_{CH4} …….…… selectivity towards CH_4 (%)
$[CO_2]_{in/out}$ …molar fractions of CO_2 in the gas going in/out (vol%)
$[CH_4]_{out}$ ….. molar fractions of CH_4 in the gas coming out (vol%)

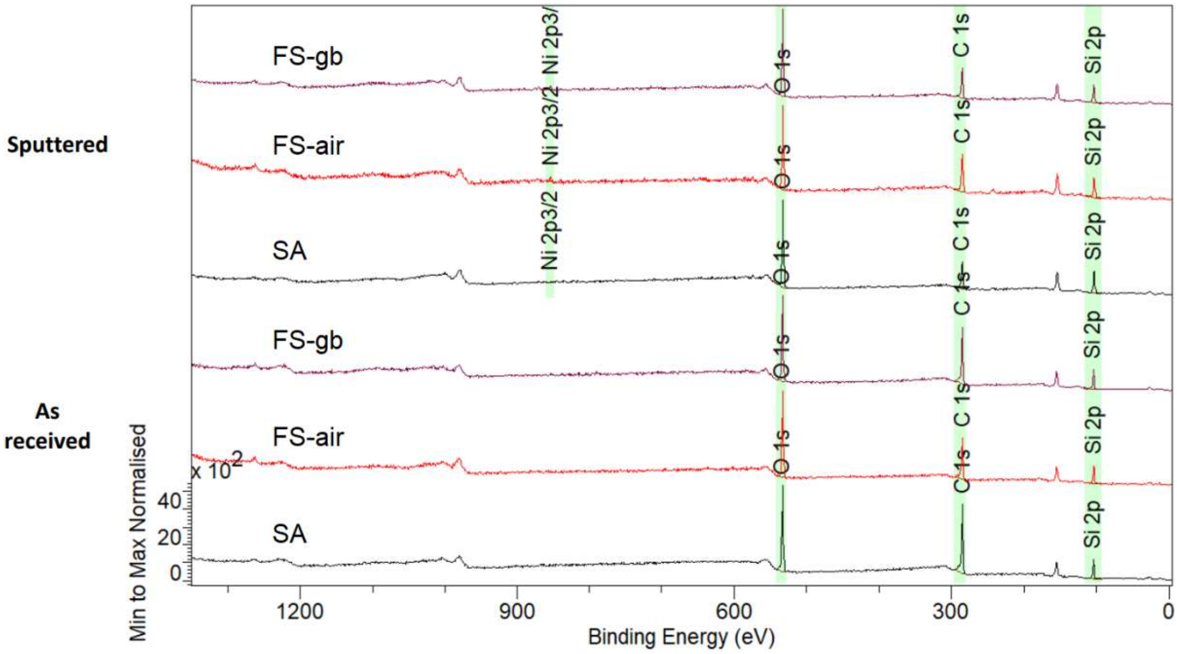

Figure A 1: XPS survey spectra of all samples in as-received state and after 360s of Ar-ion sputtering. The regions used for quantification are shown in green. All spectra were normalised with respect to their most intense signals. Three different sample areas were investigated: (SA) sample surface area; (FS-air) sample fractured in air; (FS-gb) sample fractured in a glovebox under an inert argon atmosphere. The measurements were carried out on the untreated samples (as received) and after sputtering with Ar-ions (sputtered).

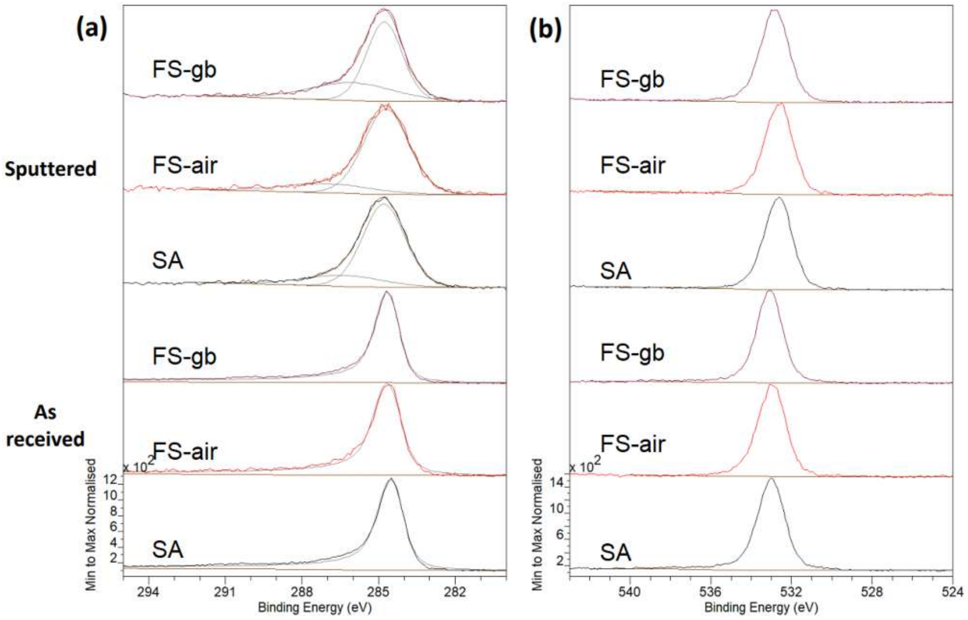

Figure A 2: XPS detail spectra of all samples (a) C1s and (b) O1s in as-received state and after 360s of Ar-ion sputtering. All spectra were normalised with respect to their most intense signals. Three different sample areas were investigated: (SA) sample surface area; (FS-air) sample fractured in air; (FS-gb) sample fractured in a glovebox under an inert argon atmosphere. The measurements were carried out on the untreated samples (as received) and after sputtering with Ar-ions (sputtered).

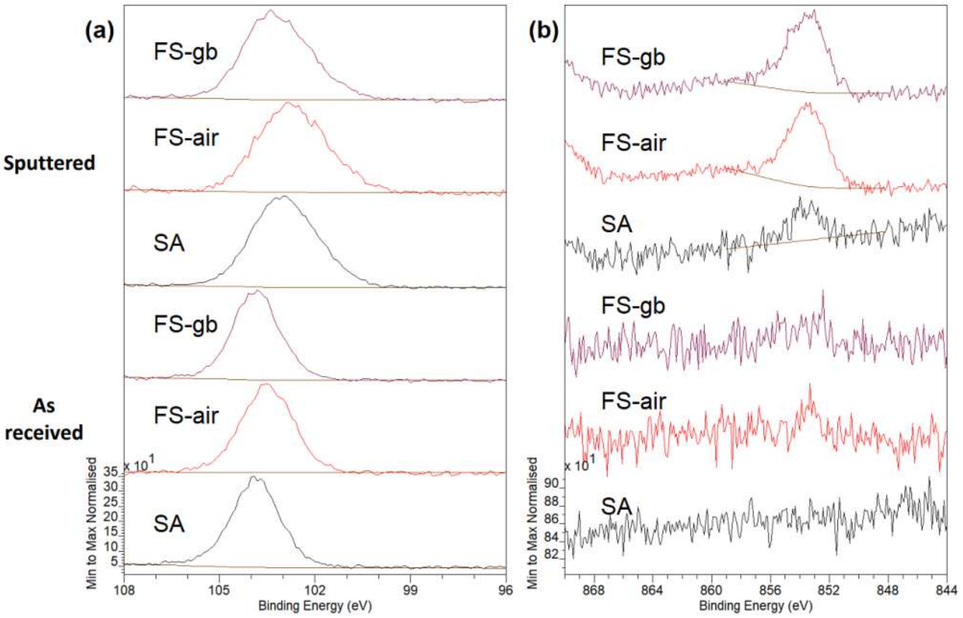

Figure A 3: XPS detail spectra of all samples (a) Si2p and (b) Ni2p in as-received state and after 360s of Ar-ion sputtering. All spectra were normalised with respect to their most intense signals. Three different sample areas were investigated: (SA) sample surface area; (FS-air) sample fractured in air; (FS-gb) sample fractured in a glovebox under an inert argon atmosphere. The measurements were carried out on the untreated samples (as received) and after sputtering with Ar-ions (sputtered).